

**PRECISE MEASUREMENT OF THE NUCLEAR DEPENDENCE OF
THE EMC EFFECT AT LARGE X**

A Dissertation
Presented to
the Faculty of the Department of Physics
University of Houston

In Partial Fulfillment
of the Requirements for the Degree
Doctor of Philosophy

By
Aji Daniel
December 2007

**PRECISE MEASUREMENT OF THE NUCLEAR DEPENDENCE OF
THE EMC EFFECT AT LARGE X**

Aji Daniel

APPROVED:

Dr. Ed V. Hungerford, Chairman

Dr. David Gaskell

Dr. Donald Kouri

Dr. Bill W. Mayes

Dr. Lawrence Pinsky

Dean, College of Natural Sciences and Mathematics

ACKNOWLEDGEMENTS

I would like to start by thanking God, the most gracious, for all the things that I have in my life. I am grateful to all my family members without whose support this dissertation would never have been written. My parents, Samuel Daniel and Ammini Daniel, whose support and strong belief in my abilities were the things that helped me to reach this milestone. I am fortunate to have a caring and supportive brother like Anil.

I am most thankful to my advisor, Professor Ed Hungerford, for his guidance, advice, and help in the development of my career, not only as a student, but also as a researcher. I would specially like to thank him for encouraging and providing support for travel to several conferences.

I was fortunate to have two extremely talented spokespersons for my dissertation experiment: Dave Gaskell and John Arrington. I have been lucky to have an excellent research adviser like Dave. I am grateful for his answering of countless questions over the years. Dave's ability to explain the most complicated things in terms of basic concepts was one of the things that I always tried to learn from him. Thanks to John for carefully reviewing this manuscript and for his tireless efforts to make the experiment a success. I appreciate him for his deep insight in the minute details of the experiment, and for the quick responses to my emails.

I would like to thank my fellow dissertation students: Jason and Nadia. Without their support it would have been much more difficult for me to accomplish this analysis. I appreciate their help with the analysis and for the lively discussions. I really enjoyed working with them. I would like to thank Patricia for the help with Coulomb corrections. Many thanks go to Tanja for being available with useful advice and suggestions.

I am grateful to Hall C staff and engineers for their contribution to E03-103. I would also like to thank all the professors and students who took shifts, or provided assistance during the running of E03-103. Special thanks to Rolf and Walter.

My colleagues Mikayel and Narbe were always just a phone call away and offered their help and assistance whenever I was in trouble. I would also like to thank Victor for being a good friend. I always enjoyed talking to them, and deeply appreciate their friendship. Also, I would like to thank the Tohoku group, especially Okayasu and Matsmura. Thanks to Kalyan and Chiranjib for their friendship and, of course, help with tennis practice.

As an undergraduate student at the NSS college, Pandalam, I received a great deal of encouragement and support from the faculty and my classmates. I owe a great deal to my teachers Mohan and Shali Kumar. Also, I would like to thank all my friends and classmates at I.I.T Madras for their assistance and support during my graduate studies. Special thanks to Professor Mahaseshasayee for her guidance and support during my graduate life at I.I.T.

I would like to thank all the staff at the Physics Department of the University of Houston. I also appreciate the inputs and comments from the doctoral committee members. Also, colleagues Siva and Tegye deserve special mention for helping me during my studies at U.H.

I would like to thank all my grand parents, cousins, aunts and uncles for their support and constant encouragement. I am grateful to my friends and family in Dallas, for their care, patience and constant support. Special thanks to my cousins, Joel and Mary, for keeping me sane during my time at graduate school and during this research.

There are many people who go unmentioned here. Be assured that although your names are not mentioned here, your help and support is deeply appreciated.

**PRECISE MEASUREMENT OF THE NUCLEAR DEPENDENCE OF
THE EMC EFFECT AT LARGE X**

An Abstract of a Dissertation
Presented to
the Faculty of the Department of Physics
University of Houston

In Partial Fulfillment
of the Requirements for the Degree
Doctor of Philosophy

By
Aji Daniel
December 2007

ABSTRACT

Experiment E03-103, carried out in Hall C at the Thomas Jefferson National Accelerator Facility, measuring inclusive electron scattering cross sections from nuclear targets over a broad range of x ($0.3 < x < 1$) up to $Q^2 \approx 8 \text{ GeV}^2$. The bulk of the data were taken at a beam energy of 5.8 GeV, with beam currents ranging from 30 to 80 μA . This dissertation describes the experiment in detail, and presents the extracted EMC ratios for the cryogenic targets ^3He , ^4He and solid targets Be, C, Cu, and Au. Our data provide the first measurement of the EMC effect in ^3He at $x > 0.4$, and improve the known precision of the existing measurements of the effect in ^4He and other nuclear targets at large x . The data have also been analyzed in terms of the structure function F_2^A to examine the scaling of the inelastic scattering in x and ξ .

DEDICATION

To my parents.

TABLE OF CONTENTS

ABSTRACT	vi
LIST OF FIGURES	xi
LIST OF TABLES	xv
CHAPTER 1 INTRODUCTION	1
CHAPTER 2 INCLUSIVE ELECTRON SCATTERING AND STRUCTURE FUNCTIONS	3
2.1 Overview of Electron Scattering off Nucleus	3
2.2 The DIS Cross Section	6
2.3 Structure Functions in Quark-Parton Model	12
2.4 Operator Product Expansion Approach	13
2.5 Low Q^2 Scaling and Quark-Hadron Duality	16
2.5.1 Quark-Hadron Duality and Nuclear Structure Functions	19
CHAPTER 3 THE EMC EFFECT	23
3.1 Overview of Experiments	26
3.2 Models of the EMC Effect	30
3.3 EMC Effect in Light Nuclei	34
3.4 EMC Effect at Large x	35
3.5 E03-103 at JLAB	37
CHAPTER 4 THE EXPERIMENTAL SETUP	39
4.1 The Accelerator	39
4.2 Hall C Beam Line Instrumentation	41
4.2.1 Beam Position Monitors	42
4.2.2 Beam Energy Measurement	43
4.2.3 Beam Current Monitors	43
4.2.4 Beam Rastering System	44

4.3	Targets	45
4.4	High Momentum Spectrometer	49
4.5	HMS Detector Package	51
4.5.1	Drift Chambers	52
4.5.2	Hodoscopes	54
4.5.3	Gas Čerenkov Detector	56
4.5.4	Lead Glass Calorimeter	57
4.6	Trigger and Data Acquisition	59
CHAPTER 5 DATA ANALYSIS		63
5.1	The Analysis Software	63
5.2	Event Reconstruction and Tracking	65
5.3	Detector Calibrations	67
5.3.1	Hodoscope Timing Calibration	68
5.3.2	Čerenkov Counter Calibration	68
5.3.3	Drift Chamber Calibration	70
5.3.4	Calorimeter Calibration	71
5.3.5	BCM Calibration	72
5.4	Kinematic Offsets and Corrections	74
5.5	Methodology of Cross Section Extraction	77
5.6	Dead Times	79
5.6.1	Electronic Dead Time	80
5.6.2	Computer Dead Time	82
5.7	Efficiencies	84
5.7.1	Trigger Efficiency	85
5.7.2	Tracking Efficiency	85
5.7.3	Calorimeter Cut Efficiency	87
5.7.4	Čerenkov Cut Efficiency	89
5.8	Background Processes and Estimation	92

5.8.1	Background from Target Cellwalls	93
5.8.2	Pion Contamination	95
5.8.3	Charge Symmetric Background	98
5.9	Target Boiling Corrections	101
5.10	Event Selection	103
5.11	Acceptance Correction	103
5.12	Cross Section Extraction	106
5.12.1	Bin Centering Corrections	106
5.12.2	Radiative Corrections	107
5.12.3	Coulomb Corrections	111
5.13	Cross Section Model	114
5.13.1	Isoscalar Corrections	116
5.14	Systematic Uncertainties	118
5.15	Differential Cross Section Results	123
CHAPTER 6	RESULTS	125
6.1	Structure Functions	125
6.2	Q^2 Dependence of F_2 Structure Function	129
6.3	Cross Section Ratios	130
6.3.1	Cross Section Ratios for Heavy Nuclei	136
CHAPTER 7	CONCLUSIONS AND OUTLOOK	143
APPENDIX A	Calculation of effective cryotarget thicknesses	146
REFERENCES	151

LIST OF FIGURES

2.1	Schematic excitation spectra for the electron scattering	5
2.2	Lowest order Feynman diagram for DIS	7
2.3	World data on F_2^P and F_2^D	10
2.4	A -dependence of R as a function of Q^2	12
2.5	Duality in the F_2^P structure function	17
2.6	Kinematic plot showing the traditional division into DIS and resonance region based on a cut on W^2	19
2.7	Structure function for iron as a function of x and ξ	20
2.8	Resonance region F_2^A/A for different targets	21
2.9	F_2^D vs Q^2 at fixed values of ξ	22
3.1	F_2 structure function ratio measured by NA2 collaboration at CERN	24
3.2	Representative EMC ratios	25
3.3	Cross section ratios from SLAC E139	28
3.4	Cross section ratios from JLab E89-008	29
3.5	Existing cross section ratios for ^4He	35
3.6	Comparison of cross section ratios for Fe and Cu with a mean field calculation	36
3.7	E03-103 kinematics	38
4.1	The CEBAF accelerator	40
4.2	Hall C beam line instrumentation	41
4.3	Beam profile with fast raster in operation	45
4.4	Side view of target ladder	46
4.5	Run by run areal thickness of cryotargets	48
4.6	Side view of the HMS	50
4.7	Side view of the HMS detector package	52

4.8	A schematic view of the HMS drift chamber	53
4.9	Hodoscope geometry	55
4.10	Calorimeter geometry	58
4.11	HMS trigger logic diagram	61
5.1	Focal plane quantities	66
5.2	Typical Čerenkov ADC and photoelectron distribution	69
5.3	Typical drift time and drift distance distributions for the HMS drift chamber	70
5.4	Example of BCM calibration	72
5.5	Residuals of the BCM calibration with respect to the global calibrations	73
5.6	Computed dW values after applying kinematic offsets	74
5.7	Ratio of experimental and Monte Carlo $H(e, e')$ normalized yields for the elastic data	76
5.8	Experimental and Monte Carlo $H(e, e')$ distributions	77
5.9	Electronic live time as a function of pretrigger rate	81
5.10	Ratio of luminosity normalized yields as a function of difference in their computer dead time	83
5.11	Tracking efficiency as a function of scintillator rate	86
5.12	Calorimeter energy vs number of photoelectrons in the Čerenkov detector.	88
5.13	Calorimeter cut efficiency as a function of E'	89
5.14	Shift in calorimeter distribution	90
5.15	Čerenkov efficiency for representative elastic runs	91
5.16	Parameterized Čerenkov efficiency applied to a production run	92
5.17	Count distributions showing dummy subtraction procedure	93
5.18	Correction factors to dummy yield due to difference in geometry of the cellwall and dummy targets	94
5.19	Pion background estimation	96
5.20	Pion contamination as a function of E'	97
5.21	Relative difference in normalized yields of π^+ and π^- as function of E' . .	98
5.22	Charge symmetric background as a function of x for 40 degree data. . . .	99

5.23	Charge symmetric background as a function of x for 50 degree data. . . .	100
5.24	Offset corrected, normalized yield vs current for the ^3He target.	101
5.25	Representative plot showing acceptance of the HMS	105
5.26	Feynman diagrams for the lowest-order radiative processes	107
5.27	Schematic representation of various processes that contribute to the measured cross sections	108
5.28	Measured and extracted Born cross section for Au at 40 degrees	109
5.29	Radiative correction factor for 40 degree data	111
5.30	Coulomb correction factor as a function of x for 50 degree data.	113
5.31	Different F_2^n/F_2^p parameterizations.	117
5.32	Magnitude of isoscalar corrections for ^3He and Au	118
5.33	Differential Born cross sections on ^2H , ^3He , ^4He , and Be.	123
5.34	Differential Born cross sections on C, Cu, and Au.	124
6.1	Structure function per nucleon vs x and ξ for ^2H and C	126
6.2	Structure function per nucleon vs x and ξ for ^3He and ^4He	127
6.3	Structure function per nucleon vs x and ξ for Be and Cu	128
6.4	Structure function per nucleon vs x and ξ for Au	129
6.5	Björken scaling in ^2H	130
6.6	Nachtmann scaling in ^2H	131
6.7	Q^2 dependence of the EMC ratios for C as a function of x	132
6.8	Q^2 dependence of the EMC ratios for C as a function of ξ	133
6.9	Cross section ratios for C as a function of x	134
6.10	Cross section ratios for ^4He as a function of x	135
6.11	Comparison of the EMC ratios for C and ^4He as a function of x	136
6.12	Cross section ratios for ^3He as a function of x	137
6.13	Cross section ratios for Be as a function of x	138
6.14	Cross section ratios for Cu as a function of x	140
6.15	Cross section ratios for Au as a function of x	141

6.16	Cross section ratios for heavy nuclei as a function of x	142
A.1	Absolute density of helium targets on a run by run basis	148
A.2	Areal density correction factor due to beam position fluctuation	149

LIST OF TABLES

4.1	Solid target thicknesses	47
4.2	Cryo target areal thicknesses	47
4.3	Systematic uncertainties for the cryotarget thicknesses	49
4.4	HMS performance characteristics	51
5.1	PID cuts used in the analysis	87
5.2	Dummy to cellwall ratio	95
5.3	Acceptance cuts used in the analysis	103
5.4	Magnitude of the energy shift in the Coulomb corrections	112
5.5	Summary of systematic uncertainties.	119
A.1	Detailed calculation of cryotarget thicknesses	147

CHAPTER 1

INTRODUCTION

Hadron physics studies strongly interacting matter in terms of its building blocks: quarks and gluons. Quantum chromodynamics (QCD) is the theory governing the strong interaction, with quarks and gluons as elementary degrees of freedom. The interaction between quarks is mediated by gluons as the gauge bosons.

Understanding QCD in terms of the elementary quark and gluon degrees of freedom remains the greatest unsolved problem of the Standard Model of particle physics. The challenge arises from the fact that quarks and gluons cannot be examined in isolation. The degrees of freedom observed in nature (hadrons and nuclei) are different from the ones typically used in the QCD formalism (quarks and gluons). However, detailed studies of the structure of hadrons (mainly protons and neutrons) provide a wealth of information on the nature of QCD.

One of the fundamental questions from a nuclear physics perspective is how do quark distributions of the nucleon change in the nuclear environment. Nuclei consist of protons and neutrons bound together by the strong nuclear force with a binding energy small compared to the nucleon mass. The typical energy scales in nuclear physics (e.g., binding energies, Fermi momenta, etc.) are of the order of several MeV. This is orders of magnitude less than the magnitude of energy transfers in scattering experiments used to determine the structure functions of nucleons. One would naively expect the structure functions to be the same for scattering off free nucleons and scattering off nucleons bound in nuclei (except for kinematic effects due to Fermi motion of the nucleons in the nucleus). Therefore, it came as a surprise when this expectation was found to be incorrect because a definite influence of the surrounding nuclear medium on the momentum distribution of the quarks was observed [1]. This

phenomenon was called the European Muon Collaboration (EMC) effect.

Since the discovery of the EMC effect, many dedicated experiments have been performed to map out the precise nature of the nuclear dependence of the structure functions. However, there are very few data on the lightest nuclei and the existing data for heavy nuclei at large x (typically interpreted as the momentum carried by the struck quark) has limited precision. Data on light nuclei are important in order to understand the models used to explain the effect for heavier nuclei. Data at large x are important to provide a reliable baseline for binding and Fermi motion calculations.

This dissertation describes the analysis of a precision measurement of the EMC effect in light to heavy nuclei and at large x . The experiment (E03-103 Collaboration [2]) was carried out at Thomas Jefferson National Accelerator Facility (JLab), Newport News, VA, USA.

The dissertation is organized as follows. The second chapter gives a brief description of electron scattering and structure functions. The third chapter describes the EMC effect in detail, followed by the motivation behind E03-103. Chapter 4 describes in detail the experimental apparatus used for data acquisition. Chapter 5 describes the data analysis procedures, including the detector efficiencies and other corrections. The experimental results and conclusions will be presented in Chapters 6 and 7.

Throughout this dissertation we use the convention $c = \hbar = 1$. Cross sections and structure functions are defined per target nucleon (unless mentioned otherwise).

CHAPTER 2

INCLUSIVE ELECTRON SCATTERING AND STRUCTURE FUNCTIONS

2.1 Overview of Electron Scattering off Nucleus

Electron scattering is one of the most powerful tools to investigate the interior of a nucleus. Hadrons, and to some extent real photons, are composite objects and they are less suited to probe the structure of the target. Interactions between electrons and nuclei are described by the exchange of virtual photons and are calculable in Quantum Electrodynamics (QED). Electron-nucleus interactions have the advantage that the nucleus remains more or less in its ground state throughout the reaction. Contrary to nucleus-nucleus collisions, where the created fireball is rapidly expanding, lepton-nucleus reactions therefore provide rather clear constraints, and the interaction of the probe with the target is theoretically better understood compared to the hadronic interactions. The relative weakness of the electromagnetic interaction implies that the virtual photon can penetrate the nuclear surface and interact with the nuclear current throughout the entire nuclear volume. The main drawback of electron scattering experiments are the relatively small cross sections, and the fact that the electron mass is small, meaning that one must take care of the radiative processes. Often these calculations are quite involved.

Inclusive electron scattering (in this case only the scattered electrons are detected, also see Figure 2.2) is quite useful to study the magnetic moment and charge density distributions of nuclei. If one wants to study the complete four-dimensional space time structure of the target, one needs to go beyond inclusive scattering and detect the final state of the target. In the work presented here, we

will be dealing with unpolarized, inclusive electron scattering under the assumption that only a single virtual photon is exchanged during the interaction.

In 1911, Rutherford used α particles to extract the charge structure of gold atoms by measuring the scattering angles of α particles. Fifty years later, Hofstadter *et al.*, [3] determined the nuclear form factors and nuclear radii using electrons of some hundreds of MeV. In the relativistic limit, the Mott cross section for an electron with energy E , scattering off a point-charge with spin 1/2 and with charge Z (in units of electron charge) is given by [4]:

$$\left(\frac{d\sigma}{d\Omega}\right)_{Mott} = \frac{4 Z^2 \alpha^2 E'^2}{Q^4} \frac{E'}{E} \cos^2 \frac{\theta}{2}. \quad (2.1)$$

In this equation $\alpha = e^2/4\pi \simeq 1/137$ is the fine structure constant, E' and θ are the energy and scattering angle of the electron and Q^2 is square of the transferred four momentum. In the expression above, the factor E'/E accounts for the target recoil. But as the four momentum transfer increases, the Mott cross section is modified due to the spatial extension of the target and this spatial extension is described by two form factors. The interaction of an electron with the nuclear charge and its magnetic moment gives information about both the electric and magnetic distributions. The angular distribution of the scattered electrons off a nucleon is then given by the Rosenbluth formula [5]:

$$\frac{d\sigma}{d\Omega} = \left(\frac{d\sigma}{d\Omega}\right)_{Mott} \left[\frac{G_E^2(Q^2) + \tau G_M^2(Q^2)}{1 + \tau} + 2\tau G_M^2(Q^2) \tan^2 \frac{\theta}{2} \right] \quad (2.2)$$

where $\tau = Q^2/4M^2$, and $G_E^2(Q^2)$ and $G_M^2(Q^2)$ are the electric and magnetic form factors which give information about the radial charge distributions and magnetic moments of a nucleon of mass, M . However, in the case of inelastic scattering, the dynamics of the reaction is discussed in terms of structure functions as opposed to the form factors as in the case of elastic scattering.

A schematic excitation spectrum for electron scattering off a nuclear target with mass number A is shown in Figure 2.1 as a function of Q^2 and $\nu = E - E'$. It is useful to define $x = \frac{Q^2}{2M\nu}$ and $W^2 = M^2 + 2M\nu - Q^2$ (see the following section for a formal definition). The qualitative features of the spectra are as follows.

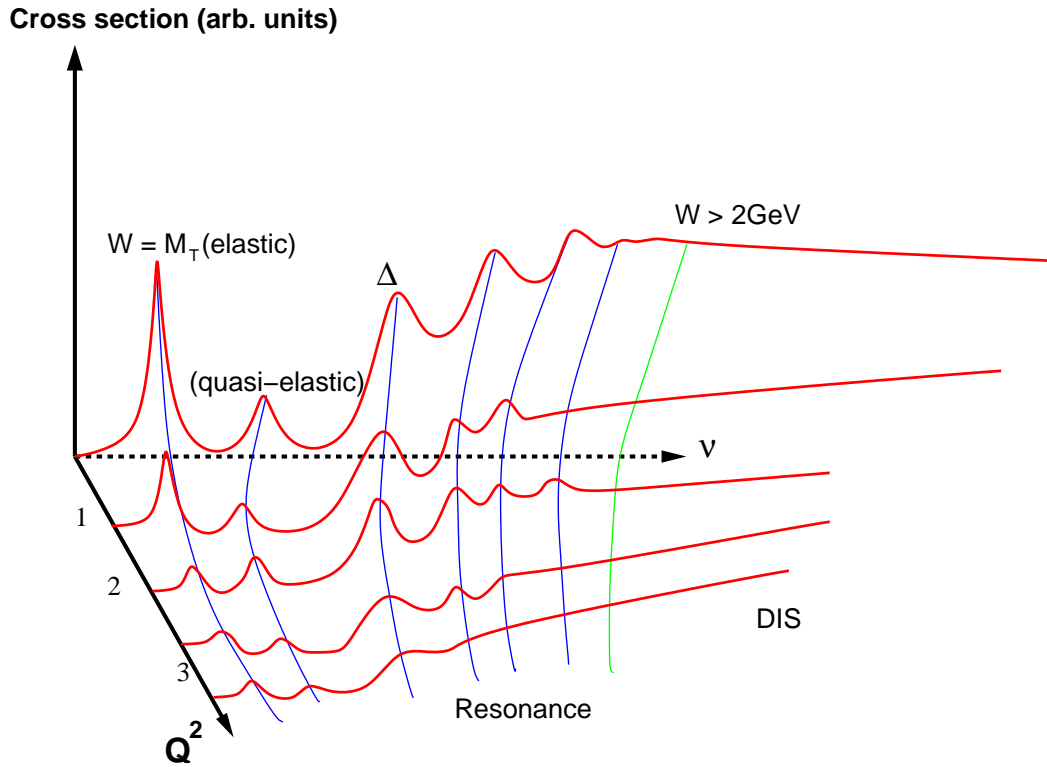


Figure 2.1 Schematics showing the main features of the excitation spectra for the electron scattering.

- Elastic scattering

At small Q^2 and ν , the distances probed are not small enough to see the composite nature of the target, and electrons interact with the entire nucleus leaving it intact. For elastic scattering $W = M$ and $x = 1$ for nucleons, and $x = A$ for nuclei. This region is interesting since it allows one to measure the charge radius and magnetic distributions of the nucleons without interference from other reaction channels because of the constrained kinematics. The width observed in the elastic peak is due to the finite resolution of the instrumentation.

- Quasi-elastic (QE) scattering

As ν increases, electrons start to scatter elastically from nucleons inside nuclei, and if the energy transferred is much greater than the binding energy, the struck nucleon does not remain bound. Since the nucleons are not at rest inside nuclei

(in the lab frame) this causes a characteristic broadening of the spectrum at $x = 1$ (there is no quasi-elastic peak for scattering from nucleons). The width and the shift of the quasi-elastic peak contains information about the internal nucleon sub-structure of nuclei.

- Resonance scattering

At higher excitation energies nucleon resonances start to appear in the spectrum. Typically this region is defined by $1.2 < W < 2 \text{ GeV}$. The existence of these states is a proof that the nucleon is a composite system. Resonances have decay width as well as width due to Fermi motion. They decay into nucleons by emitting mesons. Prominent resonances are $\Delta(1232)$, $D_{13}(1520)$ and $S_{11}(1520)$.

- Deep inelastic scattering (DIS)

At a further increase in excitation energy, nucleons lose their identity and individual resonances cannot be distinguished. Conventionally, this kinematic region is defined as $W > 2 \text{ GeV}$ and $Q^2 > 1 \text{ GeV}^2$. Here the virtual photon interacts with point like constituents inside the nucleon and probes the correlations of sizes smaller than the nucleon radius.

2.2 The DIS Cross Section

Consider electron scattering off a stationary target nucleon through a single virtual photon¹ exchange as shown in Figure 2.2.

$$e^-(k) + N(P) \longrightarrow e^-(k') + X \quad (2.3)$$

where k and k' are the four momenta of the initial and scattered electrons and P is the four momentum of the target nucleon. The four momentum of the incoming electron is $k = (E, \vec{k})$ and of the scattered electron is $k = (E', \vec{k}')$. Since the target is at rest in the laboratory frame its four momentum is $P = (M, \vec{0})$ where M is the nucleon mass. Experimentally, the produced hadrons X are not observed. Only

¹The contribution from multi (virtual) photon exchange is neglected because of the smallness of the electromagnetic fine structure constant, α .

the scattered electron energy E' and the scattering angle θ relative to the incident beam of fixed energy E are measured. The scattering process takes place through the electromagnetic interaction by the exchange of a virtual photon γ^* , with energy, $\nu = E - E'$ and momentum \vec{q} . The two characteristic Lorentz invariant quantities for

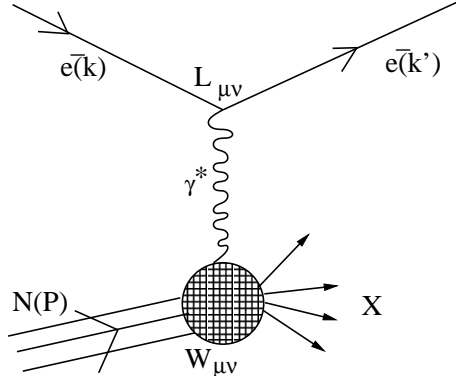


Figure 2.2 Lowest order Feynman diagram for DIS electron-nucleon scattering.

the process are the virtuality of the photon, $q^2 = \nu^2 - |\vec{q}^2|$, and the invariant mass square, $W^2 = (P + q)^2$, of the final hadronic state. The de-Broglie wavelength of the virtual photon is inversely proportional to the momentum transferred to the struck hadron by the scattered electron ($\lambda = \frac{h}{q}$). Since it is space-like ($q^2 < 0$), we define a positive quantity $Q^2 = -q^2$. Q^2 is a kinematic parameter that sets the spatial size for which the scattering process is sensitive. With increasing Q^2 , the wavelengths of the exchanged photons are decreased, and hence the spatial resolution is increased. In the laboratory frame;

$$Q^2 = 4 E E' \sin^2(\theta/2) \quad (2.4)$$

$$W^2 = M^2 + 2M\nu - Q^2. \quad (2.5)$$

It should be noted that for Eqn. 2.4 we have ignored the electron mass *i.e.* $k^2 = k'^2 = 0$. This is a valid assumption compared to the typical energy scale of the processes that we are dealing with. Assuming single photon exchange, the interaction can be separated into two parts [4, 6, 7]:

- a leptonic part $L_{\mu\nu}$, which consists of the emission of a virtual photon of energy

ν and four momentum q ; and

- a hadronic part $W^{\mu\nu}$, which contains information about the structure of the struck nucleon.

The double differential one photon exchange absorption cross section is:

$$\frac{d^2\sigma}{d\Omega dE'} = \frac{\alpha^2 E'}{Q^4 E} L_{\mu\nu} W^{\mu\nu}, \quad (2.6)$$

where $L_{\mu\nu}$ is the leptonic tensor, $W^{\mu\nu}$ is the hadronic tensor and $d\Omega$ is the solid angle into which the electron is scattered. The spin averaged electron tensor can be written as:

$$\begin{aligned} L_{\mu\nu} &= \frac{1}{2} \sum_{s,s'} \bar{u}(k', s') \gamma_\mu u(k, s) \bar{u}(k, s) \gamma_\nu u(k', s') \\ &= 2 \left[k'_\mu k_\nu + k_\mu k'_\nu - g_{\mu\nu} (k \cdot k') \right] \end{aligned} \quad (2.7)$$

where \bar{u} and u are lepton spinors obeying the Dirac equation, and s and s' are the spin of the lepton in the initial and final state. The hadronic tensor describes the photon-nucleus vertex and includes all possible transitions of the nucleon from its ground state to any hadronic final state, X .

$$W_{\mu\nu} = \frac{1}{4\pi} \sum_X (2\pi)^4 \delta^4(P + q - p_X) \langle P | J_\mu(0) | X \rangle \langle X | J_\nu(0) | P \rangle \quad (2.8)$$

Here, J_μ represents the electromagnetic quark current operator. Since the nucleon is not a point particle, an explicit expression of its tensor cannot be calculated within the framework of QCD. The most general form of the hadronic tensor is derived using the requirements of Lorentz invariance, translational and time reversal invariance, hermiticity and parity conservation. Together with the electromagnetic current conservation, which implies electromagnetic gauge invariance, $q_\mu W^{\mu\nu} = W^{\mu\nu} q_\nu = 0$, the hadronic tensor for unpolarized scattering can be written as:

$$\begin{aligned} W^{\mu\nu} &= W_1(\nu, Q^2) \left[-g^{\mu\nu} + \frac{q^\mu q^\nu}{q^2} \right] + \frac{W_2(\nu, Q^2)}{M^2} \left[P^\mu - q^\mu \frac{(P \cdot q)}{q^2} \right] \\ &+ \left[P^\nu - q^\nu \frac{(P \cdot q)}{q^2} \right]. \end{aligned} \quad (2.9)$$

Here, W_1 and W_2 are the two independent scalar response functions of two independent variables ν and Q^2 . Substituting Eqs. 2.9 and 2.7 into Eqn. 2.6, the differential cross section in the laboratory frame can be written as:

$$\frac{d^2\sigma}{d\Omega dE'} = \frac{4\alpha^2 E'^2}{Q^4} [2W_1(\nu, Q^2) \sin^2(\theta/2) + W_2(\nu, Q^2) \cos^2(\theta/2)]. \quad (2.10)$$

For a point-like particle, the W structure functions can be rewritten in terms of the dimensionless quantities as:

$$2MW_1(\nu, Q^2) = \frac{Q^2}{2M\nu} \delta\left(\frac{Q^2}{2M\nu} - 1\right) \quad (2.11)$$

$$\nu W_2(\nu, Q^2) = \delta\left(\frac{Q^2}{2M\nu} - 1\right) \quad (2.12)$$

Usually ν is replaced by another Lorentz-invariant quantity, x , the Björken scaling variable.

$$x \equiv \frac{Q^2}{2(P \cdot q)} \quad (2.13)$$

$$= \frac{Q^2}{2M\nu} \text{ (lab frame)}. \quad (2.14)$$

Similar to the fall off of elastic cross sections (due to the $1/Q^4$ dependence of the cross section, also see Eqn. 2.10), it was expected that the inelastic cross sections would fall rapidly with increasing Q^2 . Using current algebra, Björken found that [8] when Q^2 and $\nu \rightarrow \infty$, the structure functions will only depend on the ratio $\frac{Q^2}{\nu}$ or equivalently on the variable x . Thus, for large Q^2 ;

$$2MW_1(x, Q^2) = F_1(x), \quad (2.15)$$

$$\nu W_2(x, Q^2) = F_2(x). \quad (2.16)$$

The proton structure function measured at SLAC in the DIS region [9] is almost independent of Q^2 , and clearly exhibits the scaling above. More extensive measurements of structure functions have since been performed in several facilities over different orders of magnitude in x and Q^2 . A representative plot of the F_2 structure function data for the proton and deuteron is shown in Figure 2.3. It should be noted that this scaling is only approximate at low Q^2 , low x , and very high x regions due to gluon

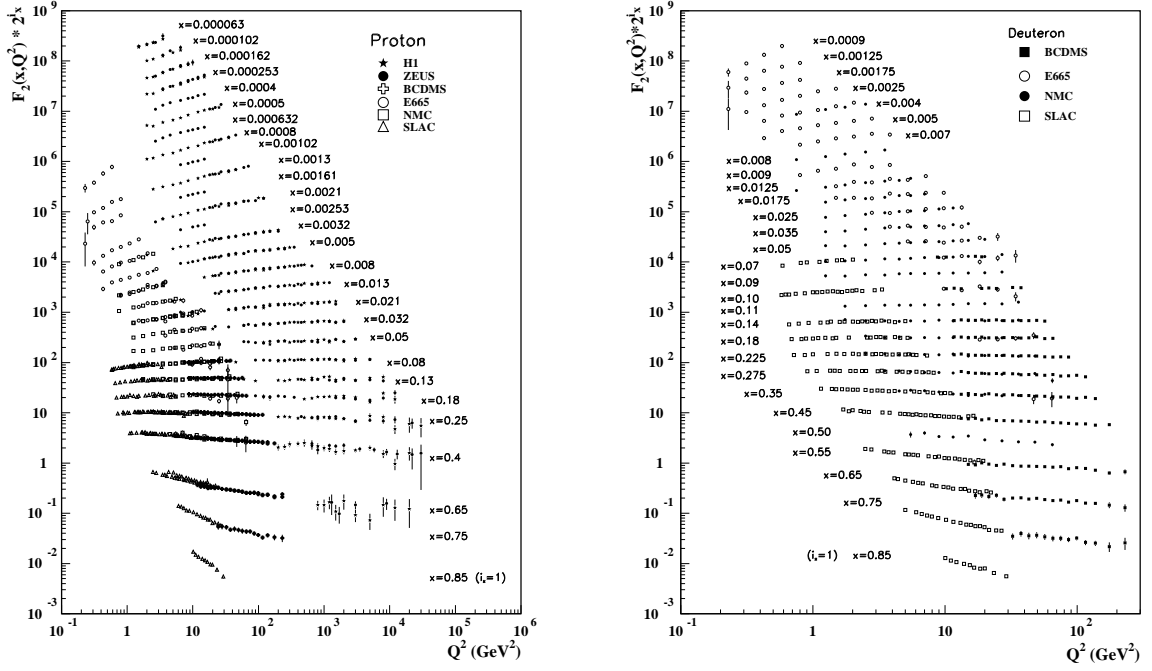


Figure 2.3 World data on the F_2 structure function of the proton and deuteron. Note that, for clarity the structure functions are multiplied by a scale factor for a given x bin (Figure from [10]).

radiation and higher twist effects. This will be further discussed in the following sections.

Analogous to the absorption cross section for real photons, the W_1 and W_2 structure functions can be expressed in terms of longitudinal (σ_L) and transverse (σ_T) virtual-photon cross sections [11]:

$$\frac{d^2\sigma}{d\Omega dE'} = \Gamma [\sigma_T(x, Q^2) + \epsilon \sigma_L(x, Q^2)], \quad (2.17)$$

where

$$\begin{aligned} \epsilon &= \frac{\Gamma_L}{\Gamma_T} \\ &= \left[1 + 2 \left(1 + \frac{Q^2}{4M^2 x^2} \right) \tan^2 \frac{\theta}{2} \right]^{-1} \end{aligned} \quad (2.18)$$

is the virtual polarization parameter, Γ is the virtual photon flux, and Γ_L and Γ_T defines the probability that a lepton emits a longitudinally or transverse polarized

virtual photon (transverse means that the direction of electric and magnetic field are perpendicular to the direction of motion, as in the case of real photons, while longitudinal means electric and magnetic field oscillate in the direction of motion of the photons). The structure functions, $F_1(x, Q^2)$ and $F_2(x, Q^2)$, can be expressed in terms of σ_L and σ_T in the following way:

$$F_1(x, Q^2) = \frac{M\sqrt{\nu^2 + Q^2}}{4\pi\alpha^2}\sigma_T \quad (2.19)$$

$$F_2(x, Q^2) = \frac{\nu Q^2}{4\pi\alpha^2\sqrt{\nu^2 + Q^2}}(\sigma_T + \sigma_L) \quad (2.20)$$

Thus, $F_1(x, Q^2)$ represents a pure transverse component while $F_2(x, Q^2)$ is a mixture of transverse and longitudinal components. The ratio of longitudinal to transverse virtual-photon absorption cross section is given by:

$$R(x, Q^2) = \frac{\sigma_L}{\sigma_T} = \left[\left(1 + \frac{\nu^2}{Q^2} \right) \frac{M F_2(x, Q^2)}{\nu F_1(x, Q^2)} \right] - 1. \quad (2.21)$$

The direct way to obtain information on σ_L and σ_T is to use a Rosenbluth separation method. For this method, one measures the DIS cross section at various beam energies at the same value of x and Q^2 , and, hence, at different values of ϵ . Two (or more) cross section measurements at different values of ϵ make it possible to extract values of σ_L and σ_T using Eqn. 2.17.

Now let us consider the per-nucleon cross section (cross section divided by the total nucleon number) ratios for two different nuclei A_1 and A_2 . With the help of Eqn. 2.10

$$\frac{\sigma_{A_1}}{\sigma_{A_2}} = \frac{F_2^{A_1} (1 + \epsilon R_{A_1}) (1 + R_{A_2})}{F_2^{A_2} (1 + \epsilon R_{A_2}) (1 + R_{A_1})} \quad (2.22)$$

It is interesting to note that when $\epsilon = 1$ or $R_{A_1} = R_{A_2}$, the ratio of the F_2 structure function is identically equal to the per-nucleon cross section ratios. In that case:

$$\frac{\sigma_{A_1}}{\sigma_{A_2}} = \frac{F_2^{A_1}}{F_2^{A_2}}. \quad (2.23)$$

In other words, the nuclear dependence of the structure function is directly given by the ratio of cross sections. All the existing measurements are consistent with little nuclear dependence in R . Representative world data [12, 13] for $\Delta R = R_{A_1} - R_{A_2}$ relevant for the E03-103 kinematics are shown in Figure 2.4.

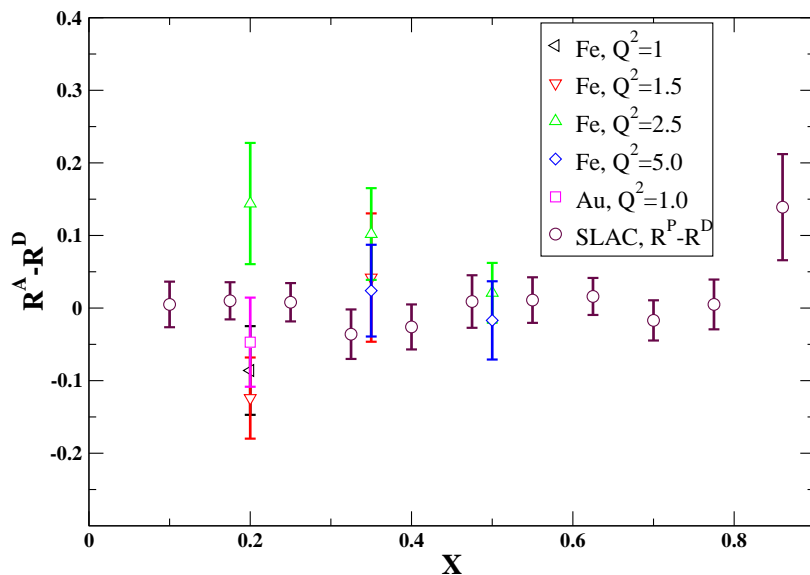


Figure 2.4 A -dependence of R as a function of x for different Q^2 values (in GeV^2). Data are from [12, 13].

2.3 Structure Functions in Quark-Parton Model

The parton model is a simple model, which has been derived from the picture of quarks being pointlike constituents of the nucleon. When $\nu \rightarrow \infty$, the lifetime of the proton virtual states is very large because of time dilatation. When $Q^2 \rightarrow \infty$, the interaction time, $\frac{1}{Q^2}$, becomes very small. So when $\frac{Q^2}{\nu} \rightarrow \infty$, the virtual photon sees a frozen state of quasi-real, quasi-free point like objects called partons [14].

In this model, the two structure functions can be expressed as a sum over all quark flavors as:

$$F_1(x) = \frac{1}{2} \sum_i e_i^2 q_i(x); \text{ and} \quad (2.24)$$

$$F_2(x) = \sum_i e_i^2 x q_i(x). \quad (2.25)$$

The distribution function $q_i(x)$ is the expectation value of the number of partons of type i in the hadron, whose longitudinal momentum fraction lies within the interval $[x, x + dx]$ and e_i is the charge of the parton, in units of electron charge. From the equations above, it follows that $F_2(x) = 2xF_1(x)$ which is known as the Callan-Gross

relation [15] and this leads to $\sigma_L/\sigma_T = R = 0$. This is a direct consequence of the helicity conservation in electromagnetic interactions combined with the spin half nature of partons, and the quark parton model predicts that R should be identically zero in the Björken limit.

Though the simple parton model is in good agreement with data qualitatively, a closer look at the available world data clearly shows the structure function is not constant, but it evolves with Q^2 . This can be seen in Figure 2.3. The structure function, F_2 , increases with Q^2 at small values of x and decreases with increasing Q^2 at large values of x . This is called the scaling violation and is not caused by a finite size of the quarks, but due to QCD gluon radiation which gives a $\ln Q^2$ dependency to the structure functions [4].

Perturbative QCD is unable to predict the shape of the structure function at fixed Q^2 . However, it predicts a logarithmic rate of change of the structure functions with Q^2 at a fixed value of x . Given the distribution function at some reference point $q(x, Q_0^2)$ we can compute it for any value of Q^2 (and, hence, the structure functions) using the Altarelli-Parisi equations [16]. Though the parton model is a simple formalism which helps to understand the qualitative features of DIS data, it is not a field theory and fails to explain the observed scaling violations. The formal basis to understand the scaling of structure functions (and the violations) is through the operator product expansion (OPE) and renormalization group equations in QCD. This will be briefly discussed in the following section.

2.4 Operator Product Expansion Approach

As mentioned in the last section, in addition to the logarithmic scaling violations, at low Q^2 , there are corrections called power corrections of the form $O([1/Q^2]^n)$. One type of power correction is kinematic corrections due to the non-vanishing mass of the target hadron. This correction falls off like M^2/Q^2 [17]. Another correction is sensitive to multi-parton correlations in the target (dynamical corrections). In this

section we will discuss the Q^2 evolution of the hadronic tensor in terms of the Operator Product Expansion (OPE). The basic idea is to express the moments of the structure functions in terms of hadronic matrix elements of the various operators (which is process dependent and not calculable in general). The Q^2 dependence of the coefficient functions is specified by renormalization group equations. Thus, structure functions can be calculated from the moments via the inverse Mellin transform [18, 19].

It is useful to express the amplitude for forward compton scattering, $T_{\mu\nu}$, in terms of hadronic tensor $W_{\mu\nu}$. Thus if,

$$T_{\mu\nu} = i \int d^4y e^{i q \cdot y} \langle P | T(J_\mu(y) J_\nu(0)) | P \rangle, \quad (2.26)$$

then the hadron tensor is connected to the imaginary part of the forward compton amplitude through the optical theorem [20]:

$$W_{\mu\nu} = \frac{1}{2\pi} \text{Im} T_{\mu\nu}. \quad (2.27)$$

The time ordered product of the currents can be expanded in a generalization of a Taylor series [18], and the expansion is found to be target independent. Thus, the general form of the light-cone OPE is [21]:

$$J_\mu(y) J_\nu(0) \sim \sum_{i,n} \tilde{C}_i^n(y^2) y_{\mu_1} \dots y_{\mu_n} \mathcal{O}^{\mu_1 \dots \mu_n}(y, 0), \quad (2.28)$$

where the sum is over different types of operators with spin n . In DIS, the $\mathcal{O}^{\mu_1 \dots \mu_n}(y, 0)$ are the quark and gluon operators with mass dimension d and spin n . They represent soft, non-perturbative physics while the coefficient functions \tilde{C}_i^n describes the hard, photon-quark interactions and is calculable within perturbative QCD. The twist τ is defined as mass dimension minus spin of the corresponding operator, $\tau = d - n$.

Using a dispersion relation [18] for T ,

$$T_{\mu\nu}(x', Q^2) = \sum_n x'^{-n} \int_0^1 dx' (x')^{n-1} W_{\mu\nu}(x', Q^2) \quad (2.29)$$

and making use of the optical theorem for the F_2 structure function [19];

$$M_2^n(Q^2) = \int_0^1 dx x^{n-2} F_2(x, Q^2) = \sum_i C_i^n(Q^2) \mathcal{A}_i^n. \quad (2.30)$$

Here, the weighted x integrals are called the moments of the structure function (Cornwall-Norton moments [22]). Thus, the product of the $C_i^n(Q^2)$ and \mathcal{A}_i^n , the moments of appropriate structure functions, is a measurable quantity. The Q^2 independent but target dependant \mathcal{A}_i^n corresponds to short distance contributions. The target independent but Q^2 dependant $C_i^n(Q^2)$ can be calculated to a given order in perturbation theory directly from the renormalization group equations [18]. This introduces a logarithmic Q^2 dependant scaling violation in the structure functions in the OPE approach. For the free field case the coefficients $C_i^n(Q^2)$ are independent of Q^2 and at high Q^2 , the higher twist terms can be neglected. Thus, we have Björken scaling for the parton model.

In terms of the twist expansion the equation above becomes [19]:

$$M_2^n(Q^2) = \sum_{\tau=2,4,\dots}^{\infty} \frac{A_\tau^{(n)}(\alpha_s(Q^2))}{Q^{\tau-2}} \quad n = 2, 4, \dots; \quad (2.31)$$

where $A_\tau^{(n)}$ are the matrix elements with twist $\leq \tau$. Because of the symmetry properties, the twist expansion, M_2^n , is defined for positive, even integers n and the Q^2 dependence of the matrix elements can be calculated perturbatively with a power series in $\alpha_s(Q^2)$. As $Q^2 \rightarrow \infty$, the leading-twist ($\tau = 2$) terms dominate the moments. In the absence of perturbatively generated corrections, these give rise to the Q^2 independence of the structure function moments, and the scaling behavior is recaptured.

For the massless case, only operators with spin n contribute to the n^{th} Cornwall-Norton moments defined by Eqn. 2.30. However, for massive partons, the trace terms in the expansion also will contribute additional terms $\sim M^2/Q^2$ and many spins contribute to the n^{th} moment [23]. Thus, the Cornwall-Norton moments in terms of x are appropriate in the region of kinematics where Q^2 is much larger than typical hadronic mass scales, where the target mass corrections can be neglected. By redefining the moments in terms of a generalized scaling variable, ξ , Nachtmann [24]

found a way to project out pure spin = n contribution even at finite M^2/Q^2 . For the F_2 structure function:

$$M_2^{n(N)}(Q^2) = \int_0^1 dx \frac{\xi^{n+1}}{x^3} \frac{3 + 3(n+1)r + n(n+2)r^2}{(n+2)(n+3)} F_2(x, Q^2) \quad (2.32)$$

is referred to as Nachtmann moments, where $r = \sqrt{1 + \frac{4M^2x^2}{Q^2}}$ and

$$\xi = \frac{2x}{1 + \sqrt{1 + \frac{4M^2x^2}{Q^2}}}. \quad (2.33)$$

It is clear that if $Q^2 \rightarrow \infty$ or $x \rightarrow 0$, then $\xi \rightarrow x$. Thus we recover Björken scaling, which is valid only for very high Q^2 and ν^2 while keeping Q^2/ν^2 finite. The difference between ξ and x can be ignored in the case of high energy scattering or at low x , but cannot be ignored at large x and low Q^2 , as is the case of the work presented here. It is interesting to examine the scaling (and violations) of the structure functions in ξ at finite values of Q^2 . However, examining the scaling in terms of ξ instead of x is only an approximate way of applying target mass corrections, but it is a reasonable approximation for the proton. The appropriate prescription for target mass corrections in nuclei is not well defined [25, 26].

2.5 Low Q^2 Scaling and Quark-Hadron Duality

The term duality refers to describing the same phenomena in two different languages. In QCD, at high enough energies, the interactions between quarks and gluons become weak and quarks can be considered asymptotically free. In this realm, observed phenomena are more efficiently described in terms of quarks. However, at low energies the effects of confinement become large, a better description of observed phenomena can be made in terms of collective degrees of freedom, *i.e.* the physical mesons and baryons. Thus, the duality between the quark and hadron descriptions reflects the relationship between confinement and asymptotic freedom, and is related to the nature of the transition from non-perturbative (low energy) to perturbative QCD (high energy). The following section will briefly discuss the quark-hadron duality observed in structure functions. A recent review of duality studies in a broader context can be found in [19] while a pedagogical introduction is available in [27].

The concept of duality in electron scattering was introduced for the first time by Bloom and Gilman when they were examining the early inclusive electron-proton scattering data from SLAC [28, 29]. They noticed an equivalence between the smooth x dependence of the inclusive structure function at large Q^2 and the average over W^2 of the nucleon resonances. Furthermore, this equivalence appeared to hold in each resonance, for restricted regions in W . If the average is defined as the integral of the structure function taken over the whole resonance region, $1 \leq W^2 \leq 4 \text{ GeV}^2$, then it is called *global duality*. On the other hand, if the averaging is performed over smaller W^2 ranges, extending over single resonances, it is known as *local duality*.

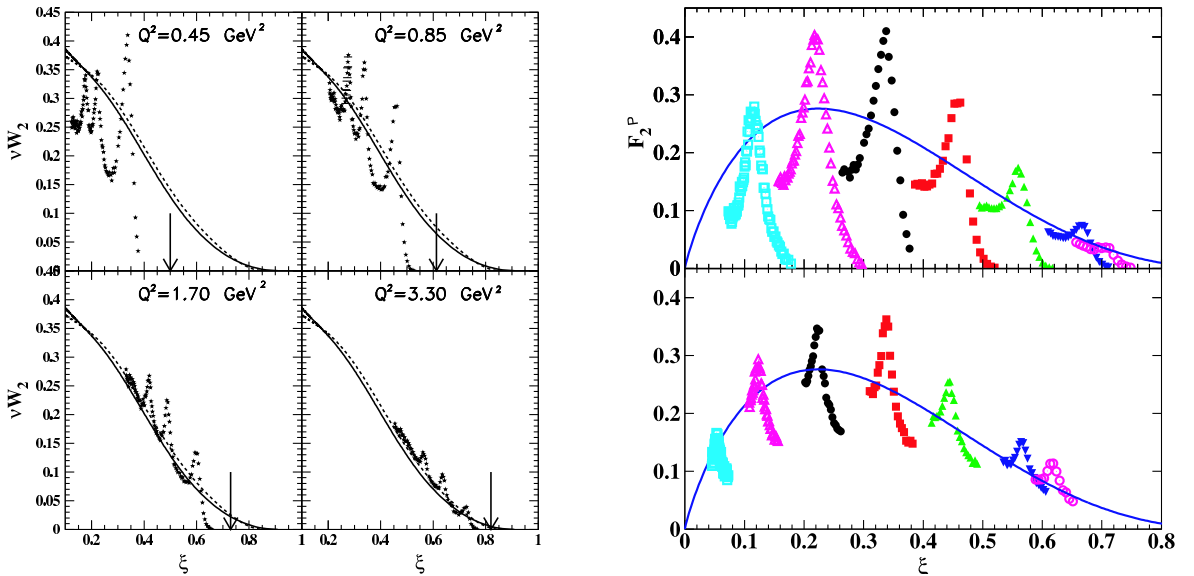


Figure 2.5 The left panel shows the F_2^P structure function data in the resonance region as a function of ξ . The right panel shows the F_2^P function for Δ (top) and $S_{11}(1535)$ (bottom) resonances as a function of ξ for different Q^2 values (represented by different colors and symbols). See the text for more details (figures from [30, 19]).

An early experiment carried out at Jefferson lab [30] revisited the Bloom-Gilman duality by measuring the unpolarized F_2 structure function in the resonance region for $0.3 < Q^2 < 4 \text{ GeV}^2$. Recently, these studies are extended up to $Q^2 = 7.5 \text{ GeV}^2$ and for x up to 0.92 [31]. Figure 2.5 shows a sample of data from reference [30] which verifies the early observations made by Bloom and Gilman down to surprisingly low Q^2 values. The left panel of Figure 2.5 shows the F_2^P structure

function plotted vs ξ . The elastic peak position is indicated by the vertical arrows. Smaller values of ξ correspond to higher W^2 kinematics. The curves are the fits from NMC DIS data [32] at the same ξ but at higher W^2 and Q^2 (dashed lines are for $Q^2 = 5 \text{ GeV}^2$ and solid lines are for $Q^2 = 10 \text{ GeV}^2$). From the figure it can be seen that, in the resonance region, the data oscillates around the scaling curve, and on average is equivalent to the scaling curve. Also, in the resonance region the data slides along the DIS scaling curve with increasing Q^2 , conclusively verifying the original observations of Bloom and Gilman about global duality. Note that the scaling curves are not that different, showing little Q^2 dependence. But the resonance data shows a strong Q^2 dependence.

The right panel in Figure 2.5 shows the F_2^p structure function plotted vs ξ for the first ($P_{33}(1232)$ or Δ) and second ($S_{11}(1535)$) resonance regions with Q^2 values ranging from 0.5 to 4.5 GeV^2 . As Q^2 increases (denoted by different symbols), the resonances move to larger ξ , always sliding along the scaling curve. However, on average, individual resonances follow the Q^2 dependency of the scaling curve. This is a manifestation of local duality. It should be noted the scaling curves shown in Figure 2.5 are fit to DIS data and scaled to the Q^2 values mentioned above. For a more quantitative comparison one should take into account the Q^2 evolution of the structure functions.

As mentioned in [19], there are many practical applications of duality. As an example, it is well known that counting rates are very low (due to the $1/Q^4$ dependence in the Mott cross section) for measurements in the DIS region ($W > 2 \text{ GeV}$) compared to measurements in the resonance region ($W < 2 \text{ GeV}$). A consequence of this subdivision (see Figure 2.6) is that a large amount of data are removed from the data analysis to strictly remain in the DIS region. The large x region is known as deep valance region (which is mostly free from QCD radiative effects) and is of great interest to both experimentalists and theorists. From Figure 2.6 we can see that in order to make a measurement of an observable at $x = 0.8$, we need $Q^2 \geq 15 \text{ GeV}^2$ in the DIS region, while this can be done at $Q^2 \sim 2 \text{ GeV}^2$ in the resonance region. This makes the large x measurements difficult. However, duality allows one to make

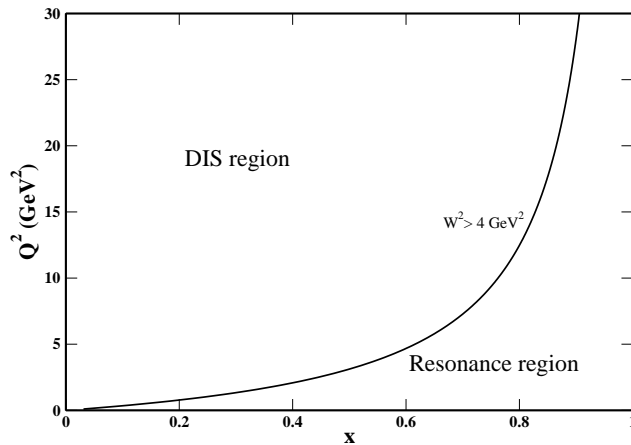


Figure 2.6 The plot shows the traditional division into DIS and resonance region based on a cut on W^2 . The region left side of the solid line represents the DIS region.

a connection between the observables in the easily attainable resonance and DIS regions. The following section will further discuss the impact of duality on the work presented here.

2.5.1 Quark-Hadron Duality and Nuclear Structure Functions

Most duality studies have focused on the free nucleon. However, there have been measurements on deuterium and heavy nuclei in the high x and moderate Q^2 region which have revealed information about duality in nuclear structure functions. As mentioned earlier, the scaling of structure functions for nucleons is expected to hold only in the standard DIS region ($Q^2 > 1 \text{ GeV}^2$ and $W^2 > 4 \text{ GeV}^2$), because of higher twist effects. For nuclei, at finite Q^2 and at large x , additional scaling violations can come from the resonance contributions and quasi-elastic scattering from a nucleon in the nucleus, rather than scattering off of a single quasi-free quark. However, deviations from $\ln Q^2$ scaling at finite Q^2 are smaller when we examine the data in terms of ξ rather than x . Inclusive measurements designed to probe $x > 1$

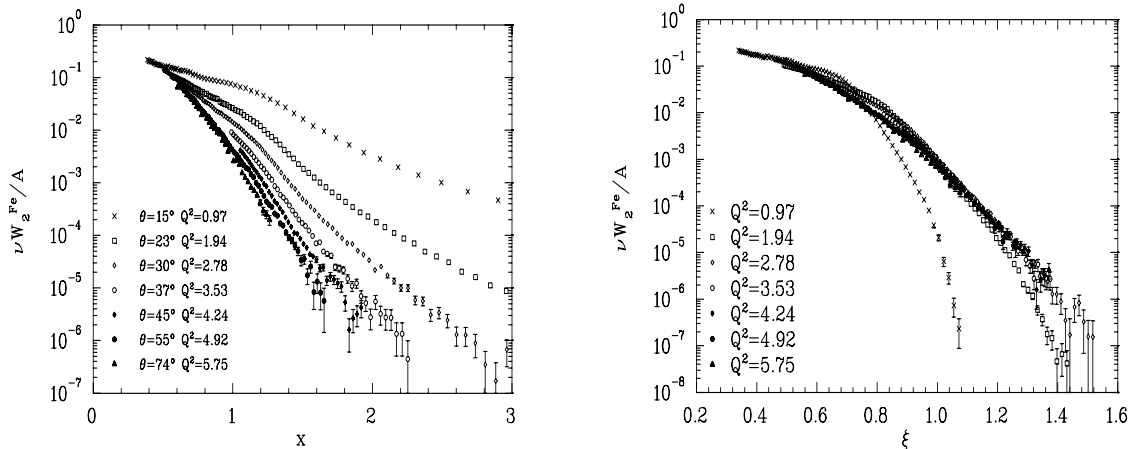


Figure 2.7 The structure function for iron as a function of x (left panel) and ξ (right panel). Data are taken at fixed scattering angle and the quoted Q^2 is the value at $x = 1$ (figure from [33]).

observed that scaling in the scattering from nuclei occurred at kinematics far from the canonical DIS region [26, 34]. This section briefly discusses the scaling of nuclear structure functions at large ξ .

Figure 2.7 shows F_2^A/A for Fe, plotted as a function of x and ξ . Data were taken with an electron beam energy of 4.045 GeV and $1.0 < Q^2 < 7 \text{ GeV}^2$ (E89-008 experiment at Jefferson Lab [33, 34]). The left panel shows the per nucleon cross sections as a function of the Björken scaling variable. The Q^2 values quoted in the figure corresponds to the value at the quasi-elastic peak ($x = 1$). Scaling is seen only for low x values where DIS dominates and quasi-elastic contributions are negligible. However, when the same data are plotted (in the right panel) as a function of ξ , the data shows scaling for nearly all values of ξ . Smearing caused by Fermi motion of the nucleon causes the visible resonance structure, clearly observable for the free nucleon, and the quasi-elastic peak, to vanish. Once the resonance structure is washed out, scaling is observed at all values of ξ for a large range of Q^2 . Thus, nuclear ξ scaling is even more dramatic than for the nucleon case. Rather than appearing as a local agreement between DIS and resonance data, scaling in nuclear structure functions in the resonance region is directly observed at all values of ξ without additional averaging.

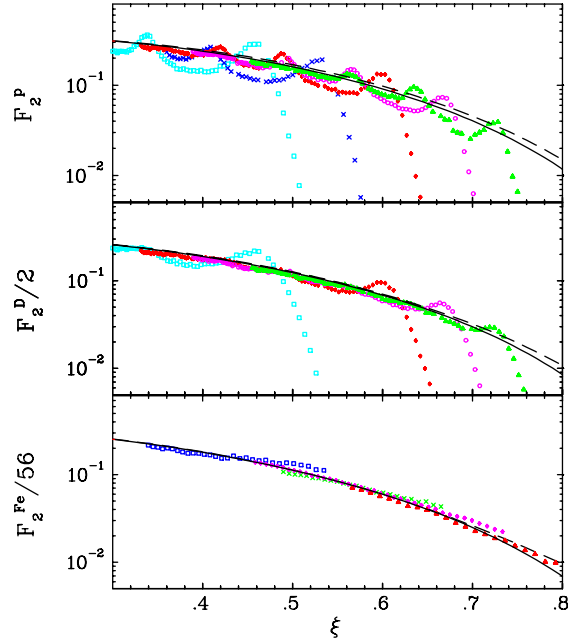


Figure 2.8 The resonance region F_2^A/A for different targets hydrogen (top), deuterium (middle) and iron (bottom). Different symbols represents data in different Q^2 ranges (figure from [26]).

Figure 2.8 shows this dramatic transition from nucleon to nuclei [26]. For hydrogen and deuterium the data covers $0.8 < Q^2 < 3 \text{ GeV}^2$, and for iron $Q^2 < 5 \text{ GeV}^2$. The curves are MRST [35] (solid) and NMC [32] (dashed) parameterizations of the structure functions at $Q^2 = 4 \text{ GeV}^2$, with a parameterization of the EMC effect [36] applied to produce the curve for iron. It is interesting to note that the significant resonance structure that was visible for hydrogen becomes less pronounced in the case of deuterium, with only Δ giving a clear peak. For iron data, even the Δ is no longer prominent.

The quality of scaling in the resonance region can be studied by examining the Q^2 dependence of the structure function at fixed ξ . Figure 2.9 shows the per nucleon cross sections (solid symbols) as function of ξ for a deuterium target [33]. The data above $W^2 = 4 \text{ GeV}^2$ are mostly from SLAC [12] (hollow symbols) and are in the typical DIS region. However, essentially all the data, both above and below $W^2 = 4 \text{ GeV}^2$, lie on the perturbative curves, which are denoted by different dashed

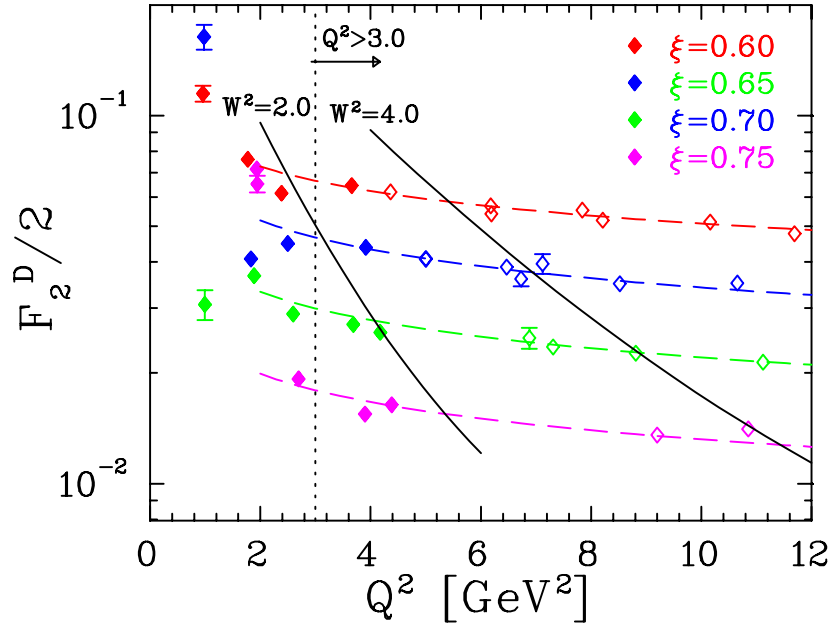


Figure 2.9 F_2^A/A vs Q^2 at fixed values of ξ for deuterium (figure from [26]). See the text for more details.

lines. This makes it practically impossible to distinguish between the hadronic and partonic regimes. Deviations appear only at very low Q^2 , $Q^2 = 1 - 2 \text{ GeV}^2$, where the quasi-elastic peaks become visible. These deviations decrease as Q^2 increases making the large ξ consistent with the perturbative dependence even at values of W^2 well below the conventional DIS limit.

Chapter 3 discusses in detail how the structure functions for different nuclei can be compared using the nuclear inelastic cross sections. A description of the EMC effect will be followed by the theoretical and experimental efforts to understand the observed nuclear dependence of the structure function ratios. Finally, the kinematics and the underlying physics motivation behind the work presented in this dissertation will be discussed.

CHAPTER 3

THE EMC EFFECT

Before 1983, it was widely believed that, at large enough Q^2 , nucleons contribute incoherently to F_2 . Thus, in the region $0.05 < x < 0.7$, the nuclear structure function would be the sum of the nucleon structure functions. A nucleus was viewed as a collection of quasi-free nucleons, and quarks were believed to be insensitive to the nuclear environment. Thus, the nuclear structure function would take the form:

$$F_2^A = Z F_2^p + (A - Z) F_2^n, \quad (3.1)$$

where F_2^p and F_2^n are nucleon structure functions. Since nuclei consist of protons and neutrons bound together by the strong nuclear force with nominal binding energies (a few MeV) compared to the typical energy scales in DIS (\sim GeV), it was believed that the binding energy would not play a big role in DIS from nuclear targets. However, since the photons do not resolve individual nucleons within the nucleus for small x or Q^2 , the cross section cannot grow as rapidly as A , and shadowing is expected to play a big role in nuclear structure functions at small x values. On the other hand, at very high x , Fermi smearing of the nucleon's momentum distribution combined with the rapid falloff of F_2^N , also invalidates Eqn. 3.1.

As part of a comprehensive study of muon scattering, the European Muon Collaboration compared data from iron with data from deuterium [1] by forming a per-nucleon structure function ratio ($R_{F_2}^A$) of these targets. The result is shown in Figure 3.1. As mentioned, the deviation of the ratio from unity was unexpected. It should be noted that the original data was wrong at $x < 0.2$, but the large x trend was confirmed. This target-mass number dependence in deep inelastic scattering is known as the EMC effect. The nuclear dependence of the EMC effect has been under intense theoretical and experimental study since the original observation.

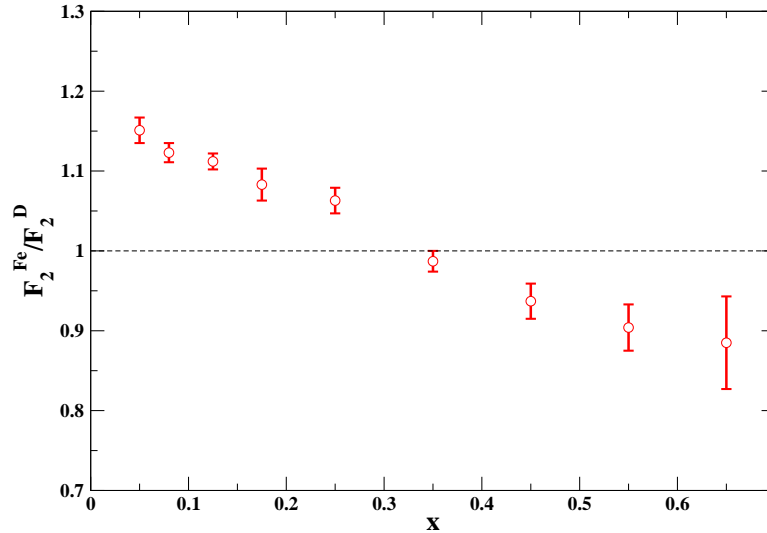


Figure 3.1 Ratio of the F_2 structure function per nucleon in iron to F_2 per nucleon in deuterium as a function of x . Data are from [1]. An additional normalization uncertainty of 7% is not shown on the plot.

It is known that the x distributions of up and down quarks differ, so it is inappropriate to compare the data from heavy nuclei to hydrogen. However, the deuteron is very weakly bound and represents an ideal isoscalar target, so the EMC ratios are usually taken with deuterium in the denominator, ignoring possible nuclear effects in deuterium. A representative plot showing the main features of $R_{F_2}^A$ is presented in Figure 3.2. Though the boundaries are somewhat arbitrary, generally $R_{F_2}^A$ is divided into four regions in x . The gross features of the data are:

- Shadowing region ($x < 0.1$)

In this region, $R_{F_2}^A$ is found to be smaller than unity. At lower Q^2 , this is described in terms of generalized vector meson dominance models. The basic idea is that the bare photon can fluctuate into a superposition of vector mesons which have the same quantum numbers. These mesons then interact strongly with the nucleons on the surface of the target nuclei and are absorbed so that the probe does not penetrate into the interior of the nucleus. Thus, the cross section (per nucleon) in a nucleus is smaller than for a free nucleon and $R_{F_2}^A$ is found to be weakly Q^2 -dependant. A recent review of nuclear shadowing can

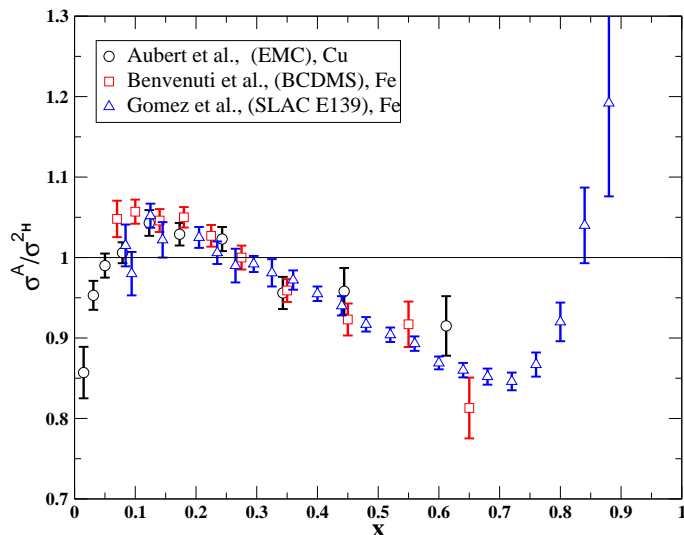


Figure 3.2 Cross section ratios (Fe or Cu to ${}^2\text{H}$) measured at different facilities with different beam types and energies. Data are from [37, 38, 36].

be found in [39].

- Anti-shadowing region ($0.1 \leq x < 0.3$)

$R_{F_2}^A$ is found to be larger than unity by a few percent. There is no common explanation for the observed enhancement. But it is often explained in terms of an enhancement due to the pion field in a nucleus.

- The EMC effect region ($0.3 \leq x < 0.8$)

In this region $R_{F_2}^A$ decreases, reaching a minimum around $x = 0.7$, and then increases. This region is commonly known as the *EMC effect* region and constitutes the main kinematic region for the work presented here. It was observed that the magnitude of the maximum depletion grows approximately logarithmically with A .

- Fermi-motion region ($x > 0.8$)

In this region, $R_{F_2}^A$ increases and grows beyond unity due to the motion of nucleons inside a heavy nucleus. In the laboratory frame, x is determined under the assumption that the nucleon is stationary. However, for nuclear targets the

Fermi motion of the nucleon inside nuclei creates a momentum distribution of nucleons, so that the nuclear structure function is a convolution of the nucleon structure function with the momentum distribution function of the nucleons. Thus, the motion of the nucleons in nuclei compared to ${}^2\text{H}$ causes the increase of $R_{F_2}^A$.

While many models have had some success, they typically reproduce only a part of the observed x dependency or are in conflict with other measurements (like the nuclear dependence of the Drell-Yan reaction). In the following sections we will briefly discuss the experimental and theoretical efforts to understand the observed nuclear dependence in relationship to the present study. There are excellent reviews on this subject available in the literature (e.g., see [18, 40, 41, 42] and references therein). We closely follow the discussions in the reviews above providing only the main features.

3.1 Overview of Experiments

EMC experiments at CERN

The first experimental DIS result on a nucleus was from CERN NA2 [1]. The experiment investigated Fermi motion effects in heavy nuclei, but the anomaly observed in the ratios was unexpected. Note that the Fe and ${}^2\text{H}$ data were taken at different times and under different running conditions which increased the systematics. The uncertainties were further refined by Aubert *et al.*, [37] who fixed a $\sim 3\%$ normalization error. This experiment used muon beams and the kinematics were $8 < Q^2 < 20 \text{ GeV}^2$ for $x = 0.05$ and $35 < Q^2 < 200 \text{ GeV}^2$ for $x = 0.65$.

Further experiments were performed by the same collaboration to reduce the systematic errors, and also included several other targets. The first follow-up experiment (CERN NA2' [43]) included targets of carbon, copper, tin and deuterium with incident muon energies ranging from 100 to 280 GeV. The kinematic range covered was $0.03 < x < 0.6$ and $4 < Q^2 < 40 \text{ GeV}^2$. The second measurement [44] was taken with deuterium and copper simultaneously in the beam.

BCDMS experiments at CERN

The BCDMS collaboration at CERN (CERN NA4) measured nitrogen, iron and deuterium cross sections [45]. They also used a muon beam and covered $0.08 < x < 0.7$ and $0.2 < x < 0.7$ with $26 < Q^2 < 200 \text{ GeV}^2$ and $46 < Q^2 < 200 \text{ GeV}^2$ for nitrogen and iron respectively. The same collaboration later published [38] a high statistics study of F_2^{Fe}/F_2^{2H} with $0.07 < x < 0.65$ and $14 < Q^2 < 200 \text{ GeV}^2$. The extracted structure function ratios were consistent with little Q^2 dependency.

NMC experiments at CERN

The New Muon Collaboration at CERN (CERN NA37 [46, 47]) measured the structure function ratios of He, Li, C, and Ca spanning a kinematic range of $0.0085 < x < 0.5$ and $0.8 < Q^2 < 17 \text{ GeV}^2$. This combination of targets allows one to compare structure function ratios of pairs of isoscalar nuclei with differing radii and nuclear densities. These data were reanalyzed [48] mainly to introduce new radiative corrections. NMC carried out a high statistics study [49, 50] with solid targets (Be, C, Al, Ca, Fe, Sn, and Pb) to map out the x and Q^2 dependencies of the structure function ratios. The data cover the kinematic range $0.01 < x < 0.8$ with $2 < Q^2 < 70 \text{ GeV}^2$. The results were consistent with little Q^2 dependence and confirmed that the A dependence is approximately logarithmic. Further, they carried out experiments [51] to study the x and Q^2 dependence of F_2^{2H}/F_2^H , in the kinematic range $0.001 < x < 0.8$ and $0.1 < Q^2 < 145 \text{ GeV}^2$ with small statistical and systematic errors. From this they extracted F_2^n/F_2^p . This data are important in order to correct nuclei for neutron or proton excess (the so called isoscalar correction, see section 5.13.1).

Experiments at SLAC

The first result on the EMC effect was confirmed by a reanalysis of data taken ten years earlier by the experiments at SLAC [52, 53, 54]. Their result was consistent with the EMC NA2 result taken at a much higher Q^2 . The first dedicated experiment to study the EMC effect was SLAC E139 and was published in [55]. An updated analysis (mainly with improved radiative corrections) was later published by Gomez *et al.*, [36]. The experiment took data on ^2H , ^4He , Be, C, Al, Ca, Fe, Ag,

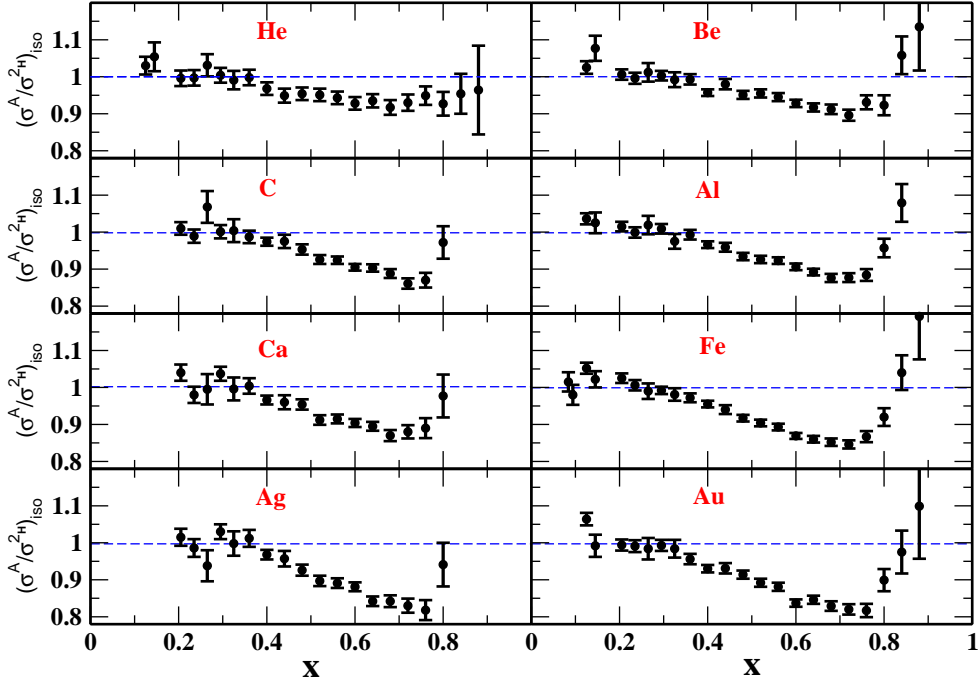


Figure 3.3 Q^2 averaged isoscalar corrected cross section ratios from SLAC E139. The errors shown are the combined statistical and point-to-point systematic errors. In addition to this there is a target-to-target systematic error and an overall normalization error of $\sim 1\%$ dominated by deuterium density.

and Au in the range $0.09 < x < 0.9$ and $2 < Q^2 < 15 \text{ GeV}^2$ using electron beams of energy between 8 and 24.5 GeV. Deuterium and heavy targets were frequently exchanged to minimize systematic errors. The resulting structure function ratios from this experiment are shown Figure 3.3. The general shape is the same for all nuclei except for ^4He , where the error bars at high x are relatively large. The A -dependence is approximately logarithmic but again ^4He deviates the most from a fit of A -dependence done at $x = 0.6$. Though the error bars are large, this is the most comprehensive data set in which the Fermi motion effects are clearly visible at high x .

The HERMES experiment at HERA

The HERMES collaboration at HERA [56] measured DIS cross sections on

^1H , ^2H , ^3He , N, and Kr with $0.013 < x < 0.65$ and $0.5 < Q^2 < 45 \text{ GeV}^2$ by colliding positrons with nuclei at 27.5 GeV. They found a dramatic divergence in the shadowing region when compared to NMC, while the high x agreed with SLAC data. The observed difference was originally attributed to an A -dependence of the ratio σ_L/σ_T . But subsequent analysis [57] showed that this anomaly was due to a peculiar instrumental effect, which was not corrected in the original analysis. The data on ^3He in the anti-shadowing region are consistent with 1.0, but data at high x has very large uncertainty.

Experiments at JLAB

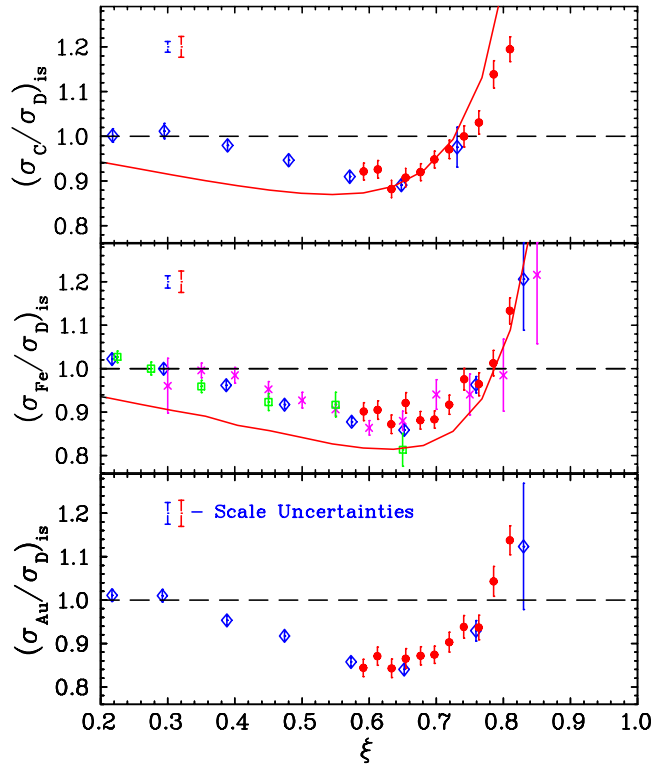


Figure 3.4 Isoscalar corrected cross section ratios (C, Fe and Au) in the resonance region from JLab E89-008 compared with the DIS data from SLAC E139 (hollow diamonds), SLAC E87 (crosses) and BCDMS (hollow squares). The curves are an updated version of the calculation [58] (figure from [26]).

Cross section ratios extracted from Jefferson lab experiment E89-008 (see section 2.5.1) are shown in Figure 3.4 along with SLAC and BCDMS data taken in the canonical DIS region. It should be noted that the JLab data are in the resonance region $1.2 < W^2 < 3.0 \text{ GeV}^2$ with $Q^2 \sim 4 \text{ GeV}^2$. Nevertheless, the size and ξ dependence of nuclear modifications in the JLab data agrees with the DIS data. In the DIS region, the Q^2 dependence of the structure functions is predicted by perturbative QCD, while additional scaling violations, target mass corrections and higher twist effects, occur at lower Q^2 and W^2 values. Thus, the cross section ratios in the resonance region are not expected to show the same behavior as the cross section ratios in the DIS region. The agreement between the resonance region and the DIS region result is viewed as a natural consequence of quark-hadron duality [19]. Another observation is that the large ξ cross-over shifts to larger ξ for heavy nuclei. The curves shown are an updated version of the calculations from [58] which uses a manifestly covariant form of the convolution formula.

3.2 Models of the EMC Effect

In general, the conventional models that describe the observed EMC effect are based on the fact that for a bound nucleon the effective x is shifted and the virtual photon probes an altered valance quark distribution as compared to a free nucleon. These models are often called x rescaling or binding models.

Inside the nucleus, the nucleons are moving in single particle orbits (Fermi motion). For a stationary nucleon, $x = (Q^2/2P \cdot q) = (Q^2/2m\nu)$. However, for a bound nucleon in the rest frame of the nucleus, the effective x is given by $x' = (Q^2/2P' \cdot q)$ where P' now includes the motion of the nucleons. In this case, on average, the virtual photon probes a lower value of x for a bound nucleon than for a free nucleon. Since the structure functions are larger at smaller values of x , the ratio of the bound to the free nucleon structure function should increase. This simple x rescaling explains the rise of the structure function ratios at large x .

However, Fermi motion is linked to nuclear binding. Consider that DIS is

taking place from a composite nucleus. The structure function of the nucleus is given by the incoherent sum of the contributions from the individual hadrons which constitutes the nucleus. The most important constituent hadrons are the nucleons themselves. In the convolution picture [59, 40]:

$$F_2^A(x) = \int_x^A dz f_N^A(z) F_2^N\left(\frac{x}{z}\right), \quad (3.2)$$

where the longitudinal momentum distribution function for the nucleon is given by,

$$f_N^A(z) = \int d^4p S(p) \delta\left(z - \left(\frac{pq}{mq_0}\right)\right). \quad (3.3)$$

Here, $S(p)$ is the spectral function of the nucleus and p, q are the four-momenta of the struck nucleon and virtual photon, m is the mass of the nucleon and q_0 is the energy transferred by the virtual photon. In the simplest mean field approximation, the nucleon energy can be represented by a potential energy plus a kinetic energy term, and can be written as $E_N = m + V + p^2/2m$. Since the nucleon is bound, there must be an attractive potential such that the sum of the potential and the kinetic terms are negative. This can be translated into an effective nucleon mass $m^* < m$, and, hence, a shift in ($x = Q^2/2m\nu$) to higher values in the intermediate x regions. Thus,

$$F_2^A(x, Q^2) \sim F_2^D(x/\bar{z}, Q^2), \quad (3.4)$$

where $\bar{z} = 1 + \langle\epsilon\rangle/m$, is the rescaling parameter which is related to the mean nucleon separation energy, $\langle\epsilon\rangle$. Thus, pure Fermi motion leads to ratios greater than unity, and the inclusion of binding changes the Fermi smearing prediction to a ratio less than unity in the intermediate x regions, reproducing the qualitative features of the EMC ratios. One of the main problems with this method lies in the determination of the correct value for $\langle\epsilon\rangle$ [18]. Models based on single nucleons are able to qualitatively explain the observed depletion of $R_{F_2}^A$ beyond $x \sim 0.3$, but fail to explain the rise for $x \sim 0.2$ [40].

Another approach recognizes that, potentially, all the momentum of the nucleus is not carried by the nucleons alone. There is nonzero probability of finding other hadrons in the nucleus (pions, deltas, multi-quark clusters ...). Thus, the most

general form of the convolution form can be written as:

$$F_2^A(x) = \sum_i \int_x^A dy f_i^A(y) F_2^i\left(\frac{x}{y}\right). \quad (3.5)$$

For example, if we include the contribution from pions also with nucleons, then Eqn. 3.2 becomes:

$$F_2^A(x) = \int_x^A dz f_N^A(z) F_2^N\left(\frac{x}{z}\right) + \int_x^A dy f_\pi^A(y) F_2^\pi\left(\frac{x}{y}\right), \quad (3.6)$$

where F_2^π is the pion structure function and $f_\pi^A(y)$ is the momentum distribution of pions in nucleus. In the equation above, it is assumed that there is no medium modification to nucleon and pion structure functions. For a stationary pion in the nucleus, $x < \frac{m_\pi}{m} \sim 0.15$. This implies that if there are more pions in the bound nucleon compared to the free nucleon, their contribution is more significant in the low x region. Because the pion is composed of a valance quark anti-quark pair, any model with such pion enhancement will naturally lead to an enhancement of anti-quarks at low x . In general, pion models describe the experimental data fairly well from $0.2 < x < 0.8$ but are less successful in explaining Drell-Yan data [60]. These models [61] predict a strong enhancement of the anti-quark distribution, which is not seen in the data.

Another approach supposes that, since the nucleus is a dense system, there is a possibility that the valance quarks in the nucleus can form clusters of a color singlet state containing 6, 9, 12... quarks [62]. For example, we can extend the convolution model to include the quark clusters:

$$F_2^A(x) = \int_x^A dz f_N^A(z) F_2^N\left(\frac{x}{z}\right) + \int_x^A dy f_6^A(y) F_2^6\left(\frac{x}{y}\right), \quad (3.7)$$

where F_2^6 is the structure function for the six quark cluster and f_6^A its longitudinal momentum distribution in nucleus. As in the case of pions, the momentum carried by the six quark cluster changes at the hadronic level. The success of the cluster model relies on the fact that a quark in a 6 or 9 quark bag has the possibility of carrying the momentum of two or three nucleons. Neglecting Fermi motion, the structure function of the nucleon (the conventional picture based on 3 quark state) vanishes for $x \geq 1$.

On the other hand, for a multi-quark configuration the structure function extends beyond $x = 1$ [18]. This implies that once we normalize the structure function, the momentum carried by the valance quark in the cluster is smaller than in the nucleon for $0 < x < 1$. Though the multi-quark cluster models make predictions for F_2^A at $x > 1$, such models have little predictive power for the small x region and the structure functions and momentum distributions of these clusters are not that well known [40].

Another category of models are related to the size of quark confinement in nuclear matter. The change in size changes the width of quark momentum distributions due to uncertainty principle. Some models assume a change in nucleon radius while some other models are based on deconfinement. In terms of QCD, a change in confinement means a change in Q^2 . Thus, QCD evolution starts at lower Q^2 for a free nucleon, and, hence, the QCD radiative processes per nucleon are larger in a bound nucleon than in a free nucleon. In this case, scaling is referred to as “dynamic” because of the evolution of the quark, anti-quark and gluon distributions. Dynamical rescaling was introduced by [63] when the authors observed that the iron structure functions from the EMC data resembled the deuterium structure function at a higher Q^2 . Thus, one has;

$$F_2^A(x, Q^2) \sim F_2^D(x, \xi_A(Q^2), Q^2). \quad (3.8)$$

In perturbative QCD, the target dependence is contained in the non-perturbative matrix element (see section 2.4). It can be shown that [18] if one starts at a scale $Q^2 = \mu^2$, the moments of the nucleon structure function evolve according to perturbative QCD and the rescaling parameter can be written as:

$$\xi_A(Q^2) = \left[\frac{\mu_N^2}{\mu_A^2} \right]^{\frac{\alpha_s(\mu_N^2)}{\alpha_s(Q^2)}}. \quad (3.9)$$

The range of applicability of these models is $0.2 < x < 0.8$, since at large x and very small x next to leading order QCD corrections become important. These models have no mechanism to describe Fermi motion effects at large x .

There are color conductor models which basically state that at large Q^2 , nucleonic structure is not important, as quarks and gluons extend over the whole

nuclear volume. In these models, the effective nucleon radius is assumed to increase until color conductivity sets in [64]. These models are related to Q^2 rescaling models in the sense that the change in the confinement radius is related to a change in the Q^2 scale.

There are models that consider the modification of the structure of a single nucleon caused by its presence in the nuclear medium. In these type of models the quark wavefunction of a single nucleon is modified by external fields provided by the surrounding nucleons. Quark-meson coupling models [65] include the effect of the nuclear medium by allowing quarks in nucleons to interact via meson exchange and additional vector and scalar fields. These models have been applied to the study the EMC effect [66]. Miller *et al.*, used a chiral soliton model to study nucleon properties and used the medium modified wave functions to make specific predictions for the EMC effect [67, 68].

Many of these models have had some success in restricted x ranges. Some of them reproduce only a part of the observed enhancement or suppression, or are in conflict with the limitations set by other measurements. The EMC effect may be fully described by one of the mechanisms currently being examined, or within some new frame-work. Binding and Fermi motion are minimal effects that must be included to explain the observed effect. Once these contributions are understood we will have a reliable baseline, and then we can look for new exciting physics. In order to distinguish between, and constrain the models based on their specific predictions, we need high quality data over a broad range in x , Q^2 and A .

3.3 EMC Effect in Light Nuclei

Though the EMC effect has been measured in heavy nuclei, there are very few measurements using light nuclei. While the EMC effect for ^4He is measured by SLAC (see Figure 3.3) the error bars are large, and for ^3He there is no data on the unpolarized structure function in the valence region. Data on light nuclei are important in understanding the microscopic origin of the EMC effect. Measurements of the

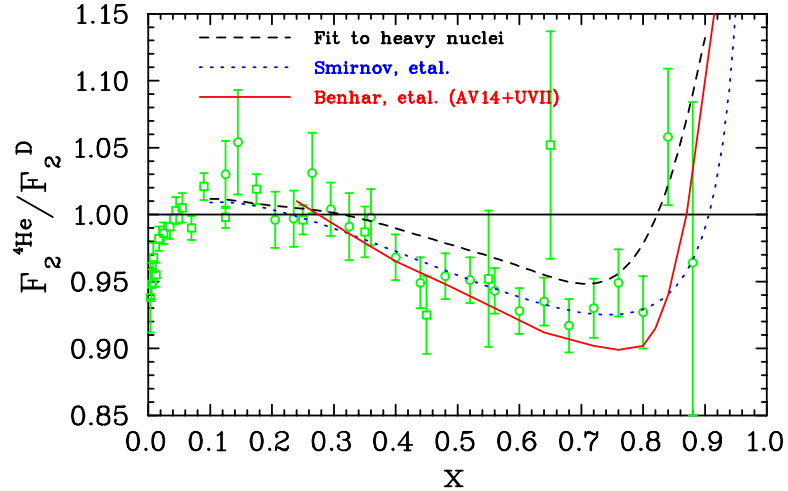


Figure 3.5 ${}^4\text{He}$ cross section ratios as a function of x . Hollow squares are from NMC [46], hollow circles are from SLAC [36]. Also shown are the fit to heavy nuclei (scaled to $A = 4$) and two calculations (figure from [2]).

EMC effect in ${}^4\text{He}$ and ${}^3\text{He}$ allow direct comparison to exact, few-body calculations. All heavy nuclei show the same x dependence of the EMC effect, but several models predict a significantly different shape in few-body nuclei [69, 70]. These models differ in their predictions not only at the point of maximum suppression but also in the high x cross over region. For example, Figure 3.5 shows the existing ${}^4\text{He}$ data along with three different models for x dependence. Since the uncertainties in nuclear structure are small for light nuclei, more precise data can constrain the binding models.

3.4 EMC Effect at Large x

As mentioned earlier, in the large x region mean-field calculations agree qualitatively with the data. But existing data at large x are of limited precision (see Figure 3.3). A sophisticated mean-field calculation by Marco *et al.*, [72] uses relativistic nucleon spectral functions in an attempt to avoid the somewhat *ad hoc* corrections that often are necessary in non-relativistic mean field calculations. The EMC effect is calculated in terms of an interacting Fermi sea and include the effects

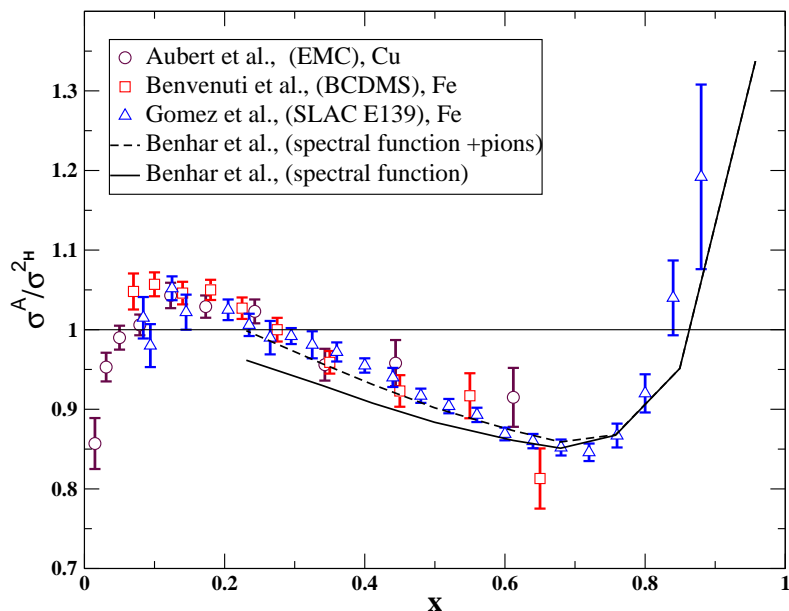


Figure 3.6 Cross section ratios as a function of x for Fe and Cu. Data are from BCDMS (squares), SLAC (circles) and EMC (triangles). Also shown are two mean-field calculations from [71]. The solid line is a binding-only calculation, while the dotted line includes a calculation of the contribution from nuclear pions.

of extra ρ and π meson contributions to the structure functions. The agreement of their calculation with data are poor at the very large x region, but this may be due to nuclear effects in deuterium, which are neglected in the calculation. In their calculation, the high x cross-over changes very little as A changes from $A = 6$ to $A = 56$. Another fully relativistic calculation by Luiti *et al.*, [58] predicts a rather different behavior at large x . In their calculation, the cross-over is predicted to shift to higher x for large A (also see Figure 3.4). Both of these calculation use fully relativistic nucleon spectral functions and give different qualitative behavior at large x .

Because of the lack of data to constrain the effects of binding, and the limited data for few-body nuclei, many calculations of the EMC effect are performed for nuclear matter, and extrapolated to lower density when comparing to the nuclear parton distributions. In this case, it is difficult to be certain that the traditional effects of binding and Fermi motion are modeled well enough to examine the effect of

more exotic effects, such as the contributions of nuclear pions or modification of the nucleon structure. Figure 3.6 shows one example of a detailed binding calculation from Benhar *et al.*, [71]. The solid line is their binding-only calculation, while the dotted line includes the contribution from nuclear pions, to explain the additional enhancement needed at small x values.

The large x data are particularly sensitive to the details of nuclear structure. Since the available world data at large x are of limited precision, more precise data in this region are needed to test binding calculations. From Fig 3.6, it is clear that the effects of binding and Fermi motion exist over the entire x region, not just at the largest x values, and modify the distribution at all x values. Data at large x , and the nuclear dependence of the high x cross over allows for tests of the prescriptions chosen for binding and Fermi motion. Since the conventional nuclear effects lead to modifications of the structure functions at all x values, a quantitative understanding is important before the addition of more exotic effects which may be required to explain the detailed nuclear dependence.

3.5 E03-103 at JLAB

In order to address the above mentioned issues, a measurement of inclusive electron scattering from light to medium heavy nuclei, giving emphasis in the large x region was proposed [2]. The E03-103 experiment was run in Hall C at Jefferson Lab during the second half of 2004. Most of the data were taken at 5.77 GeV beam energy with beam currents ranging from 30 and 80 μA . The cryogenic targets ^1H , ^2H , ^3He , ^4He and solid targets Be, C, Cu and Au were studied. All the target materials were unpolarized. Also the electron beam was unpolarized when averaged over time. Data on all targets were taken at 40° and 50° , and the cross section ratios with respect to deuterium were extracted. At high x , the kinematics were not in the conventional DIS region ($W^2 < 4 \text{ GeV}^2$), so additional data at 4 other angles covering 18° to 32° were collected at a beam energy of 5.77 GeV. Data were also collected for a detailed Q^2 dependency study at 4 angles on C and ^2H at a beam energy of 5.01 GeV. The

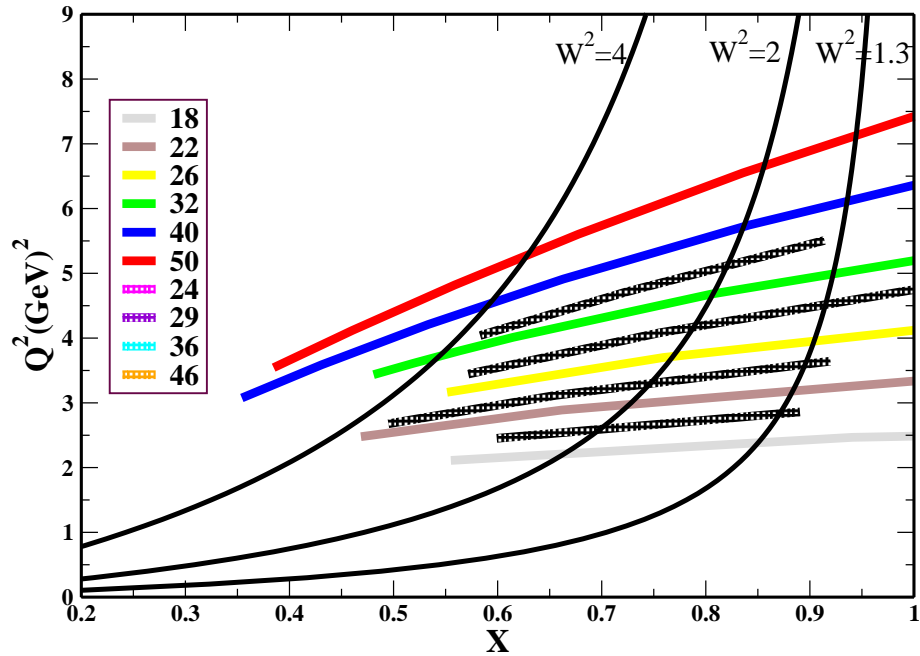


Figure 3.7 E03-103 kinematics. Contours of constant invariant mass square are shown with black lines. Different colors represent different angles as mentioned in the legend. Solid lines represent data with 5.77 GeV beam energy while hatched lines represent data taken with 5.01 GeV beam energy. Note that the units of angle and W^2 are degree and GeV^2 , respectively.

kinematics for E03-103 are shown in Figure 3.7. Scattered electrons were detected in the High Momentum Spectrometer in Hall C. The following chapters will discuss the details of the apparatus used for the data acquisition and the analysis used to extract the inclusive cross sections, and, hence, the cross section ratios.

CHAPTER 4

THE EXPERIMENTAL SETUP

Experiment E03-103 was carried out at the Thomas Jefferson National Accelerator Facility (TJNAF), where the Continuous Electron Beam Accelerator Facility (CEBAF) delivered beam to three experimental halls. E03-103 took place in experimental Hall C and this chapter provides a brief description of the setup and instrumentation used in the experiment.

4.1 The Accelerator

The CEBAF accelerator is a super-conducting radio frequency (SRF) accelerator with which one can study the structure of mesons, nucleons and nuclei using a high power electron or photon beam [73]. The accelerator can deliver beam energies up to 6 GeV with an energy spread within 0.01%, 100% duty factor, currents up to 200 μA and beam polarization better than 80%. The primary electron beam from the accelerator is separated and sent to three different experimental halls (A, B and C). The CEBAF accelerator has a race track shape, is almost 1.4 km long, and is located ~ 8 m underground. The main parts of the accelerator are the injector, two linacs (North and South), two recirculation arcs (East and West), a beam switchyard with transport elements to the halls, and beam dumps. Figure 4.1 shows a schematic view of the CEBAF accelerator. The pulsed beam originates from a gallium arsenide photocathode gun. After passing through emittance-defining apertures, an RF chopping system (operating at 499 MHz) segments this beam into three bunches (providing a beam frequency of 1497 MHz). The bunches are then adiabatically reduced to 2 ps

and accelerated to 67 MeV by superconducting cavities. Every third pulse is delivered to a different hall, resulting in a frequency of 499 MHz or one pulse every 2 ns (a CW beam with respect to most detector electronics).

The beam from the injector is accelerated in the recirculating beam-line with two linear accelerators joined by two 180 degree arcs with radius 80 m. The beam passed through each linac up to 5 times with an increase in energy of up to 1.15 GeV after each full pass. The energy of the extracted beam is always a multiple of the combined linac energies, plus the initial injector energy. Currently CEBAF is capable of delivering ≈ 6 GeV . Since the beams from different passes have their own beam pipes and steering magnets, the three halls can be run simultaneously.

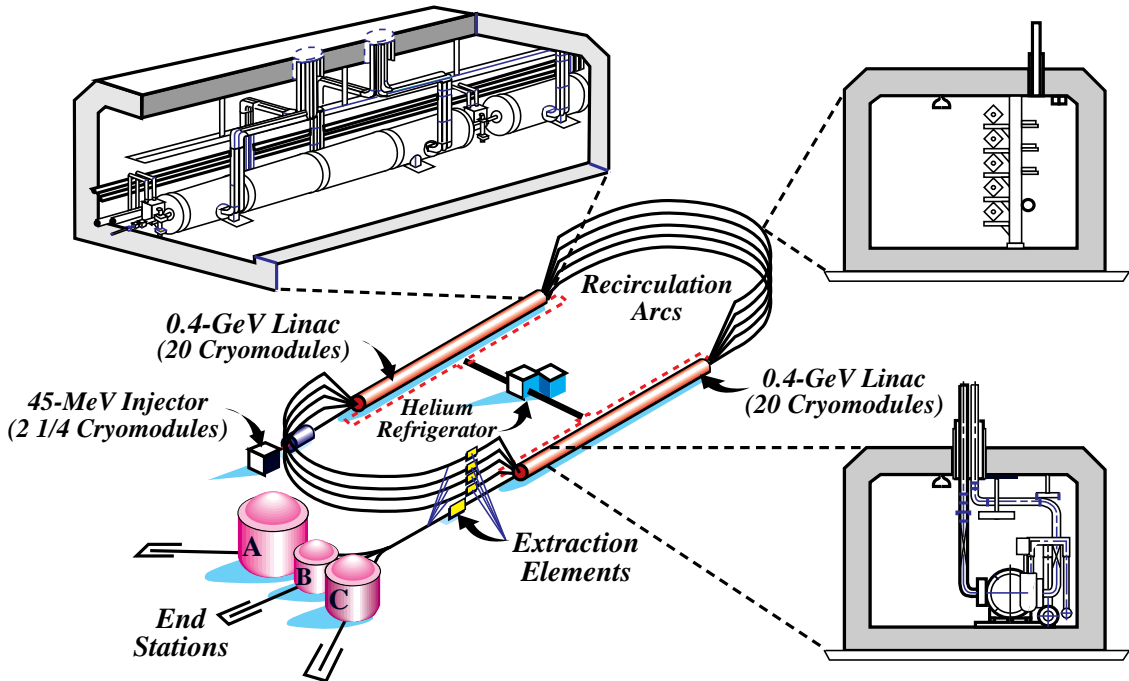


Figure 4.1 The CEBAF Accelerator. In the upper right corner, the blowup shows the cross section of five recirculating arcs in the tunnel. In the lower right corner the cross section of a cryomodule and in the upper left corner a magnified version of cryomodule cross section are also shown. The linacs have been designed to accelerate the electrons with 0.4 GeV gradient, but the energy actually reached about 0.55 GeV at the time of this experiment.

4.2 Hall C Beam Line Instrumentation

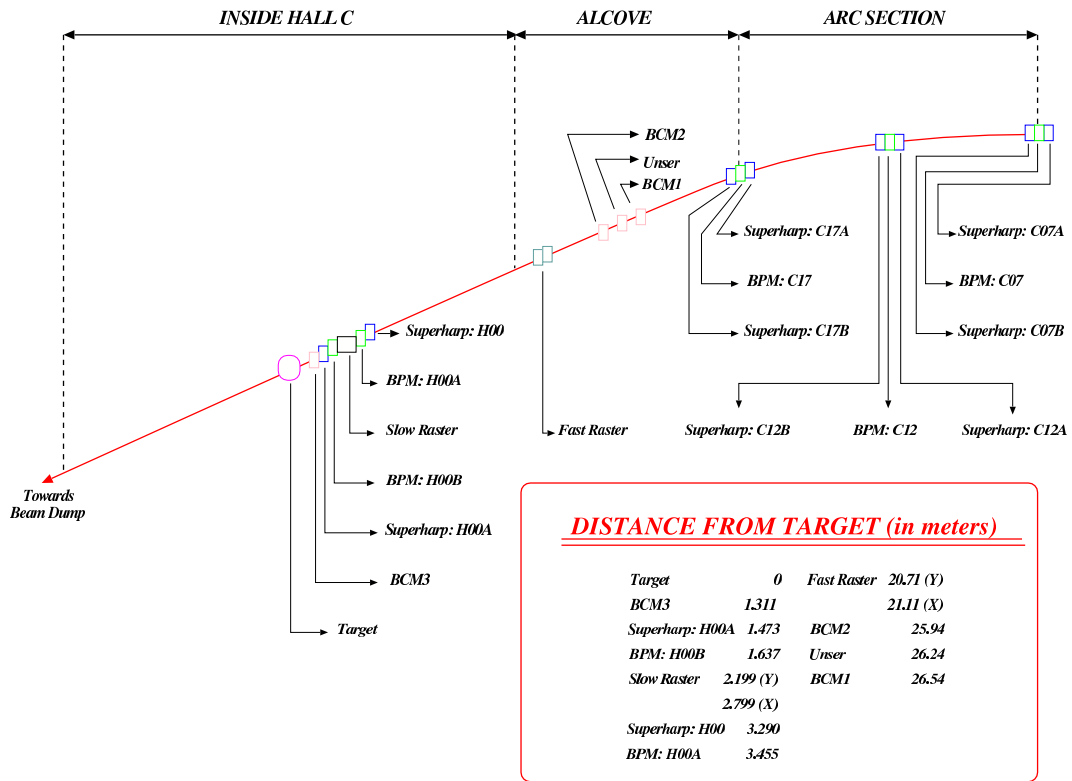


Figure 4.2 Schematics of the Hall C beam line.

The electron beam is sent to the Hall C target from the beam switchyard through the Hall C beam line. Figure 4.2 provides a schematic representation of this beam handling system. Along this beam line there are several monitors used to measure the energy, position and current of the beam as well as several magnets to focus and steer the beam. The Hall C beam line contains a fast raster system to spread the profile of the beam, and, hence, to avoid localized target boiling. After passing through the scattering chamber, the beam terminates in a beam dump located in an alcove at the rear of the experimental hall. What follows in this section is a brief discussion of the Hall C beam line elements.

4.2.1 Beam Position Monitors

Superharps make a destructive but extremely precise measurement of the beam position and profile. Superharps [74] are forked frames with three Tungsten wires mounted so that they can pass wires through the beam path. The Superharp detects the signal generated in the Tungsten wire as it moves through the beam. The frame is moved in the beam by a stepper motor and the absolute position of the frame is measured by a position encoder. With the position information and the ADC measurements, the position and profile of the beam can be reconstructed. Because the beam is interrupted in the course of the measurement, one needs dedicated runs for this type of measurement.

The beam position can also be monitored with beam position monitors (BPM). A BPM is a resonant cavity with a fundamental frequency to match both the 1497 MHz accelerator and 499 MHz Hall C beam frequencies. It is mounted in the beam line with four antennae rotated $\pm 45^\circ$ (to minimize synchrotron damage) with respect to the horizontal and vertical axis. The ratio of the voltage difference to voltage sum from two antennas in the same plane is proportional to the deviation of the beam position from the axis [75]. The amplitude of the signal is detected, processed and the passed to CAMAC electronics. Then it is recorded in the EPICS database. This method provides a position measurement which is non-destructive and relatively insensitive to beam current.

BPM information is mainly used by accelerator operators for steering the beam. However, the BPMs closest to the target (BPMs H00A, H00B and H00C in Figure 4.2) are closely monitored by the shift crew to ensure the consistency of the beam position at the target. BPM measurements can be utilized to check the beam position stability throughout the course of a run period. During the cryotarget running, the beam position was typically kept within ± 0.5 mm of the nominal beam positions. Using H00A and H00B, we can reconstruct the beam position at the target and then check for any systematic variations in the beam position during data taking.

4.2.2 Beam Energy Measurement

The superharps and the arc dipole magnets can be used to determine the energy of the electron beam. With only the dipoles energized, the arc between the beam switchyard and Hall C can be used as a spectrometer. When a charged particle traverses through a magnetic field, it experiences a force (Lorentz force) and will be deflected by a known angle. The force on the particle is

$$\frac{d\vec{p}}{dt} = e\vec{v} \times \vec{B}, \quad (4.1)$$

and the deflection angle is

$$d\theta \approx \tan \theta = \frac{d\vec{p}}{\vec{p}}. \quad (4.2)$$

Using the equations above, the electron momentum (equal to energy, neglecting electron mass) is

$$P = \frac{e}{\theta} \int \vec{B} \cdot d\vec{l}, \quad (4.3)$$

where e is the electron charge, θ is the bend radius of the arc (34.3°) and $\int \vec{B} \cdot d\vec{l}$ is the magnetic field integral. Only the dispersive elements are used for the beam energy measurement, and, hence, the measurement cannot be performed simultaneously with data acquisition. Using the arc method the absolute beam energy can be measured with a precision of $\approx 5 \times 10^{-4}$, limited mainly by the variations in the beam path length and uncertainties in the magnetic field measurement [76].

4.2.3 Beam Current Monitors

The beam charge delivered to Hall C was measured using the beam current monitors (BCM) and the Unser monitor. Though the BCMS have extremely stable zero offsets, the gain drifts slightly with time. On the other hand, Unser has a very well measured and stable gain, but has zero offset that can drift over relatively short periods of time, and, hence, cannot be used alone for absolute charge and current measurements. The BCMS are cross-calibrated with the Unser monitor over short time periods to avoid problems with zero drift. This section gives a brief description of these devices, and a more detailed description can be found in [77].

A BCM is a resonant cavity similar to a BPM. It consists of a cylindrical waveguide, mounted in the beam line so that the beam travels along the axis of cylinder. When the waveguides are tuned to the frequency of the beam, the output voltage is proportional to the beam current. The geometry was selected in such a way that the 499 MHz structure of the beam excites the 1497 MHz TM_{010} mode in the waveguide. For the TM_{010} mode, the signal is only sensitive to the beam current and relatively insensitive to the beam position. Variation of temperature can affect the resonant frequency, and, hence, will cause an error in the beam current measurement. In order to reduce the temperature fluctuations, the cavity was thermally insulated and maintained at a nearly constant temperature of 110°F.

The Unser monitor is a parametric DC transformer. It is a toroidal transformer placed in a feedback loop of an operational amplifier and is relatively insensitive to environmental factors (stray magnetic field, electromagnetic interference, mechanical vibrations, etc.). The Unser has a gain which is well known and very stable. As mentioned earlier, the Unser monitor suffers from small offsets which change over the course of minutes, and it has a poor signal-to-noise ratio. Hence, it was not used in the experiment to determine the accumulated charge. Every several days dedicated calibration runs were taken and the well-known Unser gain was used to calibrate the BCMs. During a calibration run the beam was alternately turned off (thus establishing a zero current baseline for the Unser) and on for ~ 2 minute intervals. During the beam-on periods, the gains of the BCM could be calibrated against the known gain and the measured offset of Unser. The calibration procedure and the uncertainties are described in section 5.3.5.

4.2.4 Beam Rastering System

The electron beam delivered to Hall C is CW and high current with a small transverse size ($200 \mu A$ FWHM). During our experiment, the beam current varied between 30 to $100 \mu A$. A fast raster is used to spread the heat due to the beam over a large area of the target, thus preventing solid targets from melting, and reducing the dependence of cryo-target density on current. The fast raster system is located

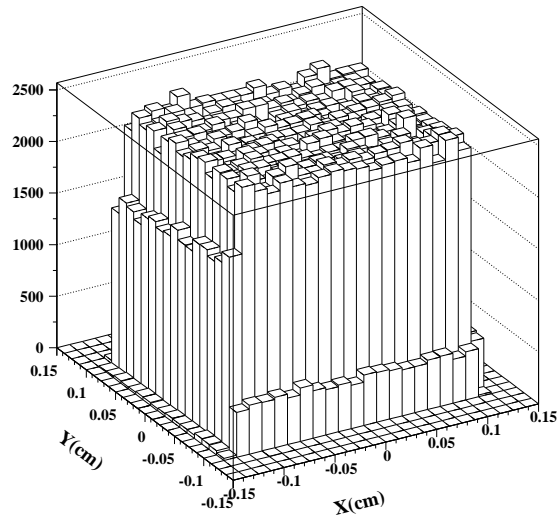


Figure 4.3 Raster pattern used during E03-103. The fast raster current is read back for each event and is correlated with the x and y position of the events at the target.

~ 20 meters upstream of the target and consists of two sets of steering magnets. The first set rasters the beam in the vertical direction while the second one in the horizontal direction at 25 kHz. Currents in the fast raster magnets were monitored and recorded in the data stream. For E03-103, we used $\approx \pm 1$ mm rectangular raster size and the raster pattern for one of the runs is shown in Figure 4.3. The reduction of the power density by this method was not completely sufficient to avoid the cryo target density fluctuations. This will be further discussed in section 5.9.

4.3 Targets

E03-103 measured the inclusive electron scattering from a wide range of nuclei which includes several cryogenic and solid targets. This experiment used the standard Hall C target ladder (see Figure 4.4) which was placed inside a cylindrical vacuum scattering chamber. The scattering chamber had entrance and exit openings for the beam as well as a vacuum pumping port and several view ports. The beam-line connects directly to the scattering chamber, so the beam does not pass through

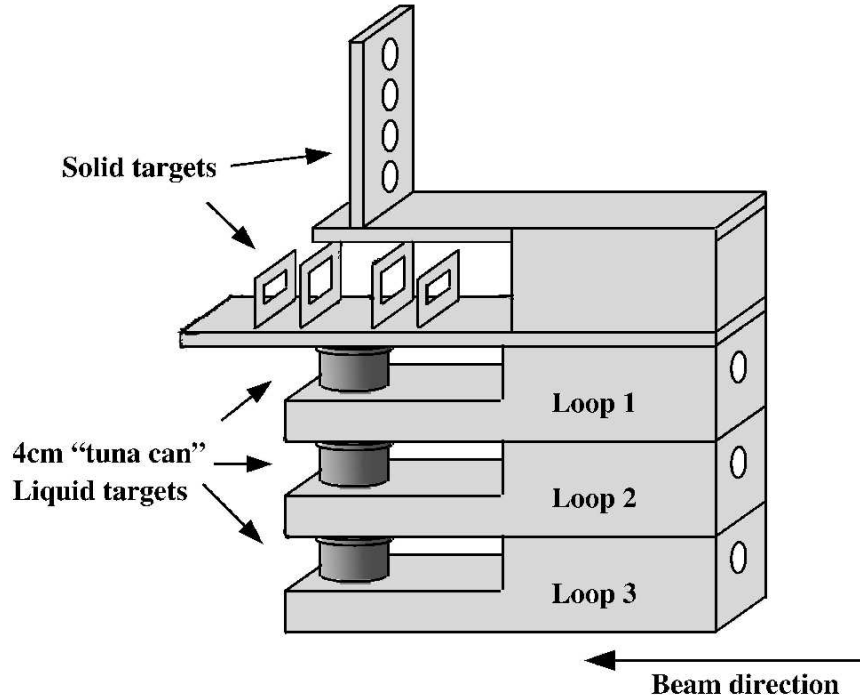


Figure 4.4 A schematic side view of Hall C target ladder.

any solid entrance window. There are two cutouts on the chamber for the two spectrometers to detect the scattered particles, which are covered with thin aluminum windows.

The target assembly contains several loops for cryogenic targets and the solid target ladder was attached above the optics sled (see Figure 4.4). The target stack can be raised or lowered by an actuator in order to put the desired target in the beam path. The cryogenic targets were cylindrical with a diameter of ≈ 4 cm and the cryogen was contained in cylindrical aluminum cans (so-called "tuna can" geometry). Each loop consisted of a circulation fan, a target cell, heat exchangers and high powered heaters. The target liquid in each loop was cooled with helium gas using a heat exchanger. The liquid moved continuously through the heat exchanger, to the target cell and back. A high power heater regulated the temperature of the cryogenic targets, compensating for the power deposition by the beam during low

Target	Thickness (cm)	Density ρ (g/cm ³)	Areal thickness X (g/cm ²)	R. L. X_0 (g/cm ²)	R. R. L. (X/X_0) (%)	Purity (%)
Be	1.012	1.848	1.8703	65.19	2.87	99.0
C	0.2943	2.265	0.6667	42.66	1.56	99.95
Cu	0.0891	8.96	0.7986	12.86	6.21	99.995
Au	0.0196	19.32	0.3795	6.46	5.88	99.999
Al foil1	0.0973	2.699	0.2626	24.01	1.09	98.0
Al foil2	0.0976	2.699	0.2633	24.01	1.10	98.0

Table 4.1 Thicknesses and related information of the solid targets. Here, R. L. represents the radiation length and R. R. L. is the relative radiation length and represents the amount of material in the path of the beam, in units of radiation length.

current or beam off periods. Solid targets were attached above the optics sled and all the foils in the solid target ladder were separated vertically.

Target	$\langle t \rangle$ (cm)	Density ρ (g/cm ³)	Areal thickness (X) (g/cm ²)	R.L (X_0) (g/cm ²)	R.R.L (X/X_0) (%)	Purity (%)
¹ H	3.865	0.0723	0.2794	61.28	0.456	99.99
² H	3.860	0.167	0.6446	122.6	0.526	99.95
³ He	3.865	0.0708	0.2736	65.27	0.419	99.9
⁴ He	3.873	0.135	0.5229	94.32	0.554	99.99
¹ H	3.890	0.0763	0.2968	61.28	0.484	99.99
² H	3.894	0.167	0.6503	122.6	0.530	99.95

Table 4.2 Cryo target areal thicknesses and related information. Here, $\langle t \rangle$ represents the offset corrected cryogen in the path of the beam. The rows at the bottom list the cryo target information in the summer run period while the top rows contains information about fall run period. A detailed explanation of the thickness calculation can be found in Appendix A.

The optics sled contained a dummy target, which consisted of two aluminum foils (aluminum alloy Al-6061-T6) placed ~ 4 cm apart. These dummy targets mimicked the cellwalls of the cryogenic target and facilitated the measurement of the background originating from the cellwalls. It should be noted that these dummy targets were not exact replicas of the cellwalls. The dummy targets were flat aluminum

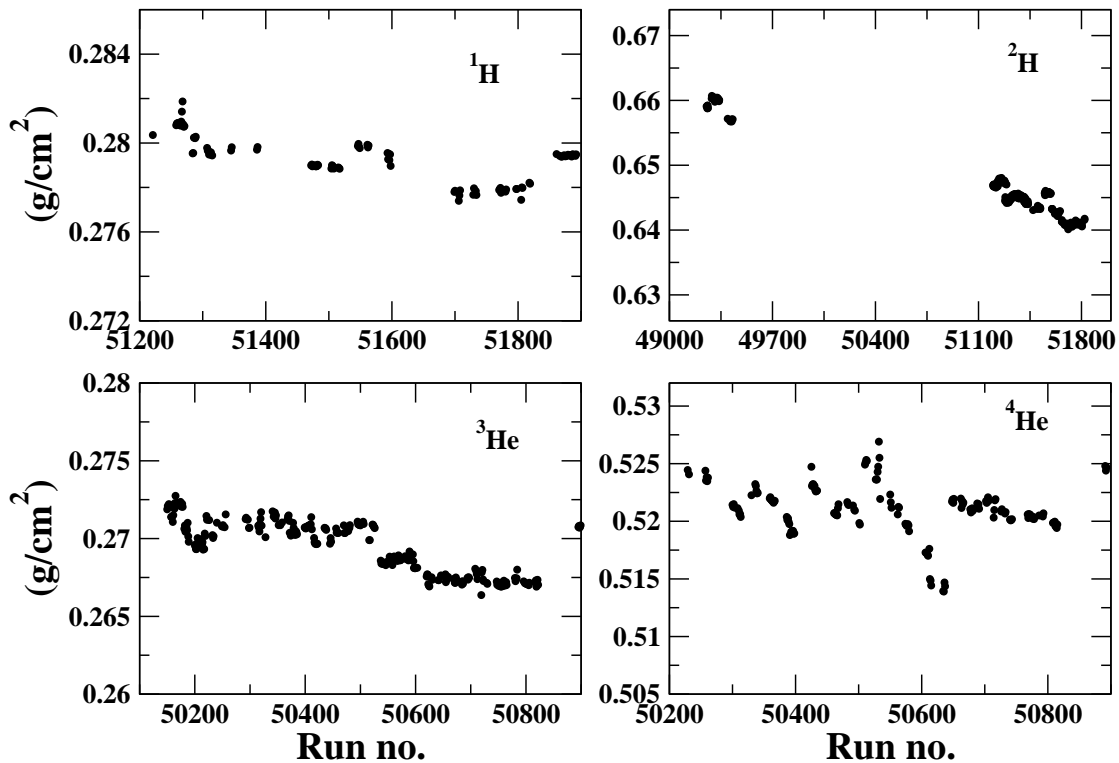


Figure 4.5 Run-by-run areal thickness of cryotargets vs run number for all the cryotargets used in E03-103. This is used in the analysis on a run by run basis and includes all the corrections discussed in Appendix A.

foils and were approximately 7 times thicker than the walls of liquid targets thus reducing the time needed for background measurement. This geometry has some effect on the radiative corrections and will be further addressed in section 5.8.1. For a more detailed description of the target system and the general workings of the cryogenic targets, see Ref. [78, 79].

Since the target cans are cylindrical, the effective target length seen by the beam can be different from the nominal diameter of can if the beam does not intersect the geometrical center of the targets. Careful analysis is needed to account for different offsets. Areal thicknesses of the cryo targets were computed from the target density and the length of the cryogen in the path of the beam. The target density was calculated using the knowledge of temperature and pressure. During the experiment it was found that there was a leak in the helium target cells. This density

variation was found to be significant, and it was decided to compute the densities on a run by run basis. Table 4.2 gives the final cryo target areal thicknesses used in the analysis. Fluctuations in the beam position can also affect the effective target length over the course of the run. This was computed on a run by run basis and applied to all the cryo targets. The effective areal thicknesses for all the cryotargets throughout the course of the experiment are shown in Figure 4.5. Detailed calculation of the cryotarget areal thicknesses and corrections due to beam position fluctuations can be found in Appendix A.

Thicknesses of the solid targets were calculated using measurements of the mass and area of the targets. For solid targets, there is an uncertainty coming from the angle of the target relative to beam direction, and this is found to be $< 0.01\%$. Table 4.3 shows the best estimate of the systematic uncertainties associated with the target thicknesses. In addition, there were uncertainties due to target boiling effects, and this will be further discussed in section 5.9.

Source of error	^1H	^2H	^3He	^4He
Beam position at target (%)	1.3	1.3	1.3	1.3
Equation of state (%)	0.5	0.5	1.0	1.0
Pressure (%)	0.2	0.01	0.6	0.2
Temperature (%)	<0.1	<0.1	1.7	0.9
Cell diameter (%)	0.2	0.2	0.2	0.2
Target purity (%)	<0.01	<0.05	<0.1	<0.01
Total (%)	1.4	1.4	2.4	1.9

Table 4.3 Different sources that contribute to the systematic uncertainties for the cryotarget thicknesses. Total uncertainty is given by the quadrature sum of the different individual uncertainties.

4.4 High Momentum Spectrometer

This experiment used the High Momentum Spectrometer (HMS) to detect the scattered electrons from the interaction vertex. The HMS is a 25° vertical bend spectrometer, which consists of three quadrupole magnets, one dipole magnet and a

detector package. The detectors are housed inside a shielded concrete enclosure and this hut is mounted on a steel carriage which can be rotated on a pair of concentric rails to the desired angle. Changes to the spectrometer angle and magnetic field were made remotely from the counting room. The HMS has a large solid angle and momentum acceptance ($\pm 10\%$ nominal, but is limited to $\pm 8\%$ because of the knowledge of the acceptance) and it can be used to detect particles with central momentum up to 7.3 GeV. A schematic side view of the HMS is shown in Figure 4.6. The following sections will discuss the magnets and optical properties of the HMS as well as the detector package used for the particle identification. A more detailed description of HMS and the detector package can be found in [34].

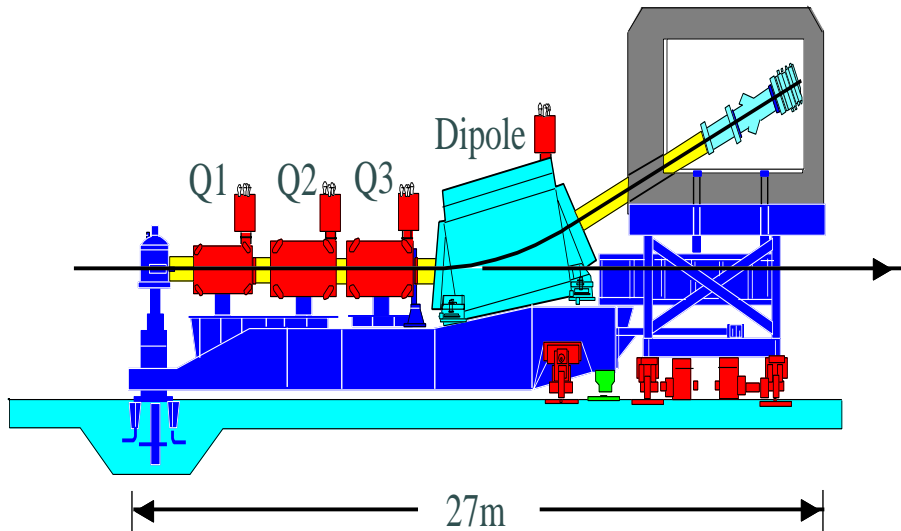


Figure 4.6 A schematic side view of the HMS.

All magnets in the HMS are superconducting and are cooled with 4° K liquid helium. The focusing properties and acceptance of the HMS are determined by the quadrupole magnets, and the central momentum is determined by the dipole. The magnetic field in the quadrupole is regulated by the current in the magnets, while the magnetic field in the dipole is monitored using a nuclear magnetic resonance probe inserted in the magnet. The HMS was operated in point-to-point tune in

which quadrupole magnets Q1 and Q3 focused in the dispersive direction whereas quadrupole Q2 focused in the transverse direction. The nominal “focal plane” is defined to be the plane perpendicular to the central trajectory, positioned roughly halfway between the two drift chambers. A slit system was installed in front of Q1, allowing insertion of various collimators. The angular acceptance is fixed by this collimator. These collimators are made of 2.48 inch thick HEAVYMET (machinable Tungsten with 10% CuNi) and effectively stops all the electrons that strike it, aside from those that hit the inside edge and create a shower of particles. Those events can be removed by tracking cuts. A summary of HMS performance characteristics is given in Table 4.4.

Parameter	Value
Maximum central momentum (GeV/c)	7.3
Momentum acceptance (%)	± 10
Momentum resolution (%)	< 0.1
Solid angle (msr)	6.5
Scattering angle acceptance: in-plane (mrad)	± 32
Scattering angle acceptance: out-of-plane (mrad)	± 85
Scattering angle resolution: in-plane (mrad)	± 0.5
Scattering angle resolution: out-of-plane (mrad)	± 0.8
Extended target acceptance (cm)	10

Table 4.4 HMS performance characteristics in a point-to-point tune.

4.5 HMS Detector Package

Figure 4.7 shows the arrangement of the detector elements of the HMS. The detector package consists of two drift chambers (DC1 and DC2) to measure the particle trajectories, two sets of $x - y$ scintillator hodoscopes used for triggering and time-of-flight measurements (S1X, S1Y, S2X and S2Y), and a threshold gas Čerenkov and lead-glass calorimeter to distinguish electrons from pions and other particles. The following subsections will briefly discuss the detector components. Detailed information about the detector operation, geometry, and performance can be found in [34, 80].

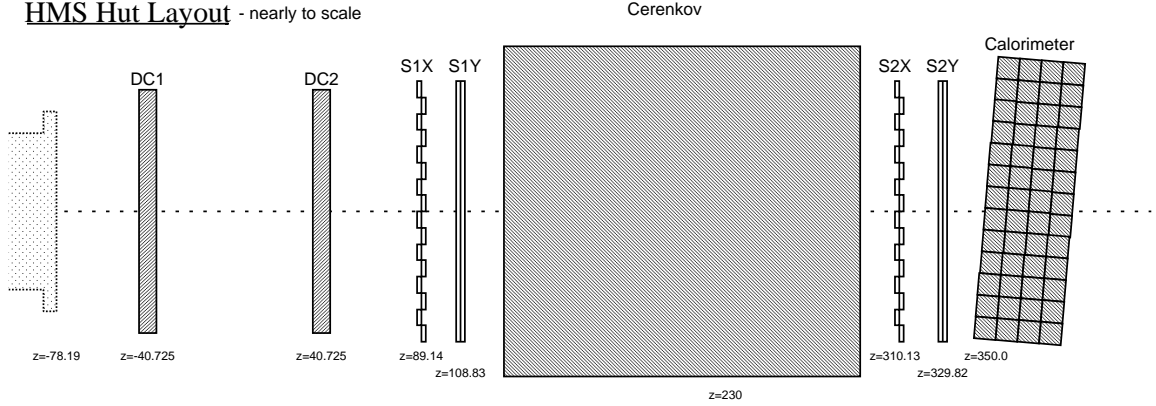


Figure 4.7 A schematic side view of the HMS detector package.

4.5.1 Drift Chambers

The drift chambers are used to find the position and trajectory of the particle at the focal plane, and this is required to determine the position and momentum of the scattered particle at the interaction vertex. The drift chambers are spaced ≈ 80 cm apart and measure the track of a particle as it traverses the detector hut. A drift chamber is basically an ionization gas detector filled with a gas or gas mixture. A number of layers of cathode “field” wires kept at negative potential and anode “sense” wires kept at positive potential are positioned inside the chamber. A drift chamber consists of different drift cells, and as charged particle passes through these cells, they ionize the gas molecules. These electron-ion pairs are accelerated towards the anode and cathode. During this motion it collides with other gas molecules which results in a nearly uniform motion of charges towards the anode and cathode. The distance from the origin of the electrons to anode is known as the drift distance, while the time required for the electrons to move this drift distance is the drift time. The drift distance is

$$x = \int_{t_0}^{t_1} u dt, \quad (4.4)$$

where t_0 is the arrival time of the particle in the chamber, t_1 is the time at which the signal appeared at the anode and u is the drift velocity. In this analysis, the drift

time is taken with respect to the time of the event trigger. Thus, with the knowledge of the absolute position of the sense wires and the drift time from the TDC, the position of the particle at each plane can be determined by the tracking software. The tracking software then uses the position and direction information gathered from both chambers to reconstruct the trajectory of the particle through the hut.

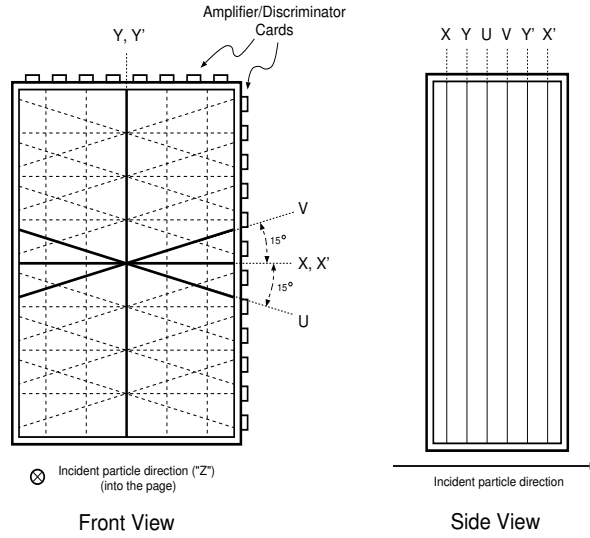


Figure 4.8 A schematic view of the HMS drift chamber.

There are two drift chambers in the HMS located at the front of the detector stack to minimize the effect of multiple scattering on track reconstruction. Each chamber consists of 6 planes of wires, arranged in order X, Y, U, V, Y', X' with 1.4 cm spacing between the planes. Each plane consists of a set of alternating field and sense wires, with the field wires at negative high voltages (1800-2500 V), while the sense wires are held at ground potential. In addition, guard wires are used to create a roughly equipotential surface around each sense wire. The voltage is dependent on the distance from the nearest sense wire. The X and X' planes of wires measures the position in the dispersive direction, while Y and Y' planes measure the position in the non-dispersive direction. The U, V planes are rotated by $\pm 15^\circ$ with respect to the X and X' planes. Orientation of the wires is illustrated in Figure 4.8. The planes that measure the position in the same direction have their wires offset by 5 mm to

resolve left-right ambiguities.

The gas used in the HMS drift chambers is an equal part argon-ethane (1:1 by mass) mixture bubbled through isopropyl alcohol, and controlled by a gas handling system located outside the experimental hall. Argon is an effective multiplier at relatively low electric field. But the excited argon atoms may induce continuous discharge. Ethane suppresses this effect [80] by absorbing and thermally dissipating the radiation from recombination of electrons with the argon atoms. However, the recombination of ionized ethane fragments may create a polymer, which affects chamber performance over time. A small amount of alcohol can effectively retard the polymer growth.

The readout electronics consisted of LRS 2735DC and Nanometrics N-227 preamplifier/discriminator cards mounted directly on the chambers. On receiving a trigger from the trigger supervisor, the signals are amplified and digitized if they are above a threshold. The discriminator thresholds can be remotely adjusted from the counting house. The digitized signals are sent to an LRS 1887 96 channel pipeline FASTBUS TDC via twisted pair cable. Signals were then carried to the Hall C counting house and then sent to the data acquisition computer.

The tracking algorithm, efficiency studies and the performance of drift chamber are further discussed in Chapter 5. More details about HMS drift chambers can be found in [81].

4.5.2 Hodoscopes

When a charged particle passes through a scintillating material, it ionizes electrons in the material, and leaves the atoms or molecules in higher energy states. The material emits light upon spontaneous de-excitation to the ground state. When coupled with a conversion and amplifying device, these scintillations can be converted to electrical pulses.

The main purpose of the scintillator hodoscope is to supply a trigger for the

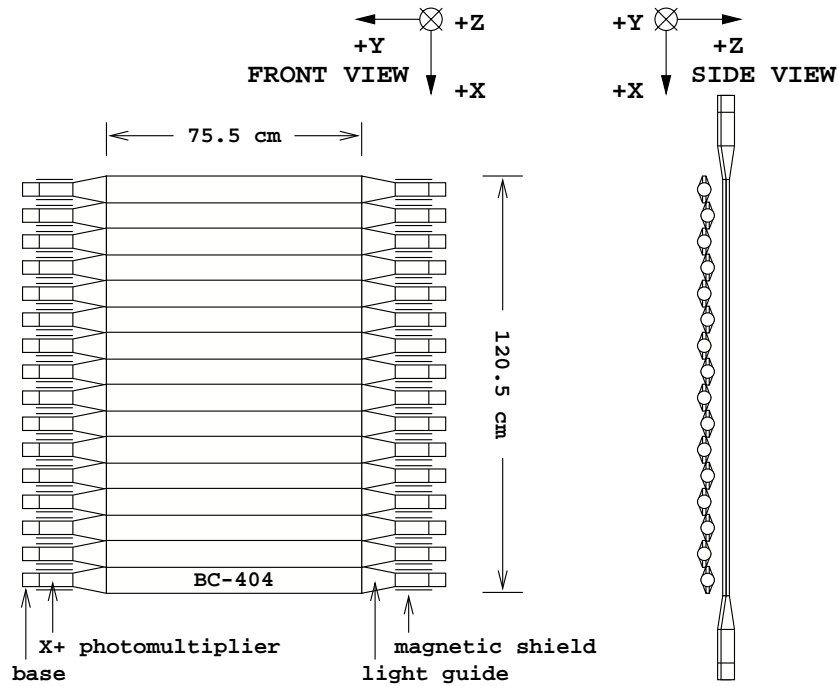


Figure 4.9 Hodoscope geometry for an X plane.

detector and allow the identification of heavy particles using the difference in time (time-of-flight) between two separated scintillator planes (for E03-103 the momentum is too high to differentiate pions and electrons using a TOF cut, hence, we mainly use the hodoscope for triggering purposes). The HMS has four planes of hodoscopes (S1X, S1Y, S2X and S2Y) arranged in two $x - y$ planes which were positioned as shown in Figure 4.7. Each X hodoscope consists of 16 horizontally (in the non-dispersive direction) oriented paddles while the Y hodoscopes consist of 10 vertically (in the dispersive direction) oriented paddles. The X paddles are 75.5 cm long, the Y paddles 120.5 cm long and all of them are 8 cm wide and 1 cm thick. The paddles are staggered in the beam direction to ensure that the active area is fully covered. This geometry is illustrated in Figure 4.9. The segments are made of BC-404 plastic (a polymer of alkyl benzene). The scintillator must be light tight in order to minimize the loss of light produced in the scintillation process, and more importantly to prevent leaking of external light into the system. This is accomplished by wrapping the scintillator

with a reflective material (aluminized mylar) and then covering the elements with Tedlar [34].

Each paddle is terminated by two photomultiplier tubes (Philips XP2282B) connected to lucite lightguides. The analog signals from the PMTs are routed via a patch panel to the electronics rack in the counting house. Each signal is then split in two with 1/3 and 2/3 of the original amplitude. The smaller signal goes to analog-to-digital converters that measure the integral of the pulse. The larger signals are discriminated. One set of the digital output is sent (with appropriate delays) to TDCs for the timing information, and also to VME scalars. The other set of output is utilized for the trigger logic and sent directly into a Lecroy 4654 logic module. A more detailed description of the hodoscopes can be found in [34]. The hodoscope trigger logic will be further discussed in section 4.6.

4.5.3 Gas Čerenkov Detector

The HMS contains a threshold gas Čerenkov counter used for electron identification. When a charged particle moves in a medium with a velocity greater than the velocity of light in that medium, it emits electromagnetic radiation. This is known as Čerenkov radiation. The radiation is emitted in a conical pattern [80] with the half angle θ is given by

$$\cos \theta = \frac{1}{\beta n}, \quad (4.5)$$

where n is the index of refraction of the medium and β is the relative velocity of the particle with respect to velocity of light. For threshold production of radiation,

$$\beta c \geq \frac{c}{n}. \quad (4.6)$$

This threshold property of the detector can be used in a very effective way to discriminate between species of differing mass at the same momentum. Using Eqn. 4.6, the threshold energy for the production of Čerenkov radiation can be written as

$$E = \gamma mc^2 = \sqrt{m^2 c^2 + p^2 c^2}, \quad (4.7)$$

where $\gamma = (1 - \beta^2)^{-\frac{1}{2}}$.

The HMS Čerenkov detector is a large cylindrical tank (inner diameter ≈ 150 cm and length ≈ 165 cm) and is positioned between the S1Y and S2X scintillator planes (see Figure 4.7). It has two front reflecting mirrors which focus the light onto two PMTs. The circular end of the tank is covered with 0.1 cm aluminum windows. For E03-103, the detector was filled with 5.15 psi (~ 0.35 atm) of Perfluorobutane (C_4F_{10}) at room temperature. At this pressure and temperature, the index of refraction of the gas is 1.0005. In this case, the threshold momentum is ~ 16 MeV for electrons and ~ 4.3 GeV for pions. This was well below the momentum range of E03-103 except for the lowest angles. However, when an electron passes through the aluminum entrance window of the Čerenkov detector, there is a chance that it can produce knock-on electrons¹ which subsequently trigger the Čerenkov detector. These background electrons cannot be removed with a cut on the number of photoelectrons produced by the Čerenkov detector, and thus we need another detector for particle identification.

The signals from the PMTs were sent to readout electronics in the counting house. The signals are split: one output goes to the ADC module while the other is summed and discriminated (threshold set to ≈ 0.5 photoelectron) to supply signals to TDCs and trigger logic in order to form the Čerenkov trigger. The calibration of the Čerenkov counter and cut efficiency studies will be further discussed in Chapter 5.

4.5.4 Lead Glass Calorimeter

A lead glass calorimeter detector was used in conjunction with the Čerenkov detector for electron identification. A calorimeter is a detector that uses the total absorption of electrons to measure their energy. Since this is a destructive measurement, the calorimeter is usually used as the last element in a detector package. When a high energy electron passes through a medium, the electric field created by the atoms of that medium will cause a deflection of the electron's path, with emission

¹Also called delta rays, knock-on electrons are emitted from atoms by the passage of charged particles through matter.

of photons. This so-called bremsstrahlung, or braking radiation, will in turn generate electron-positron pairs. These pairs also radiate photons as they pass through the medium, resulting in a shower of particles. The charged particles produce Čerenkov radiation in the glass, which are detected by photomultiplier tubes. The signal produced is proportional to the total track length of the particles in the calorimeter with velocity above the Čerenkov threshold. This is approximately proportional to the initial energy of the incident electron. The electromagnetic shower stops when the particles no longer have enough energy to radiate bremsstrahlung.

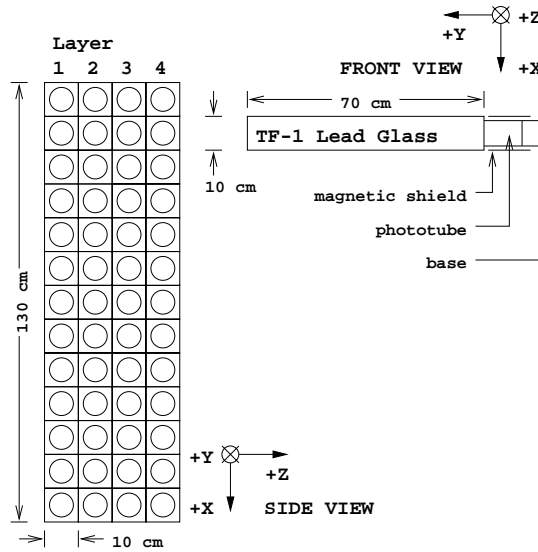


Figure 4.10 Schematics of the HMS calorimeter.

On the other hand, hadrons that reach the calorimeter (mostly pions) have a different behavior. Hadrons are too heavy to initiate bremsstrahlung radiation. In fact, most pions will not be stopped inside the lead glass detector unless they undergo a strong interaction (for example, a charge exchange reaction, $\pi^- p \rightarrow \pi^0 n$) with a nucleus in the lead glass. In this case, essentially the full energy of the neutral pion will be deposited in the calorimeter if the photons from the π^0 decay are completely absorbed. The photons can lead to showers similar to those created by electrons or positrons. Electrons or positrons entering the calorimeter deposit their entire energy,

and the normalized energy spectrum (E_{cal}/p = ratio of the deposited energy of e^- or e^+ in the calorimeter to the reconstructed energy of the particle from tracking) is 1. Pions typically deposit ~ 300 MeV in the calorimeter, and, hence, for a 1 GeV pion, the E_{cal}/p distribution peaks around 0.3 GeV. The pion's energy distribution at low normalized energy spectrum has a tail that contaminates the electron distribution (also see Figure 5.12). Calorimeter calibrations, cut efficiency and pion contamination studies will be further discussed in Chapter 5.

The HMS calorimeter consists of 10 cm \times 10 cm \times 70 cm blocks of TF-1 lead glass, positioned at the rear of the detector hut. The blocks are arranged in four layers with 13 blocks per layer (for a total thickness of 16 radiation lengths, along the particle direction). The calorimeter geometry is illustrated in Figure 4.10. The energy deposition of a shower peaks within the first two blocks and the entire energy of the incident electron is absorbed within the four layers. The calorimeter is rotated by 5° from the spectrometer optical axis to prevent any losses that would result from particles passing through the spaces between the blocks. Phototubes attached to the (read out on both sides for first two layers) blocks collect the Čerenkov light. These signals are sent to the counting house where they are split: one half is sent to the ADC for pulse height measurement and the other half is routed to the trigger logic unit.

4.6 Trigger and Data Acquisition

The purpose of the trigger circuit is to select a particular reaction of interest from competing background events. It is often not possible to record all the events (this will increase the computer deadtime significantly, see section 5.6 for more details), but all events of interest must be retained. The main aim of the trigger logic is to reduce computer deadtime and total data volume, while simultaneously accepting events of interest. During E03-103, the data acquisition rate was limited to ~ 1 kHz when the deadtime was kept below 20%. Some events can be lost because the trigger

signal was not generated thus causing a trigger inefficiency, while a loose trigger allows too many background events resulting in considerable deadtime. Thus, one must optimize the trigger system to reject background events while keeping the efficiency as high possible. What follows is a brief outline of the structure and implementation of the HMS trigger pertaining to this analysis.

A primary component of the HMS trigger is the scintillator hodoscope system. For a given plane in the hodoscope, a logical OR of all the phototubes on the “positive” side are formed (For example: $\mathbf{S1X}_+ \equiv \mathbf{S1X1}_+ \cdot \text{OR} \cdot \mathbf{S1X2}_+ \cdot \text{OR} \cdot \dots \cdot \mathbf{S1X16}_+$). Similarly, there are equivalent sets of signals for the “negative” side of each plane (for more details about the geometry see section 4.5.2). The next step is to form a logical AND of the sets of tubes on each side of the planes to get $\mathbf{S1X}, \mathbf{S1Y}, \mathbf{S2X}, \mathbf{S2Y}$ (e.g., $\mathbf{S1X} \equiv \mathbf{S1X}_+ \cdot \text{AND} \cdot \mathbf{S1X}_-$). These four output logic signals indicate which of the hodoscope planes are active. Then the front and back pairs are formed by the logical OR of the X and Y signals to give $\mathbf{S1}$ and $\mathbf{S2}$, where $\mathbf{S1} \equiv \mathbf{S1X} \cdot \text{OR} \cdot \mathbf{S1Y}$ and similarly for $\mathbf{S2}$. The last step is to form the “time of flight” trigger, $\mathbf{STOF} \equiv \mathbf{S1} \cdot \text{AND} \cdot \mathbf{S2}$ and the scintillator trigger \mathbf{SCIN} (also known as “the 3/4 signal”) with the requirement that at least three of the four scintillator layers of both hodoscopes are fired. Since there is no particle identification involved in \mathbf{SCIN} , this will provide data to study the electron efficiency and pion rejection of both the Čerenkov detector and calorimeter.

As mentioned earlier, the trigger level Čerenkov signal (\mathbf{C}) requires 0.5 photoelectrons. In the case of the calorimeter, the signals from the blocks in each layer are summed to give the energy deposition in that layer ($\mathbf{SUM-A}, \mathbf{SUM-B}, \mathbf{SUM-C}$ and $\mathbf{SUM-D}$). The $\mathbf{SUM-A}$ signal (also called the preradiator signal) and the sum of the energy deposited in the entire calorimeter were discriminated to give three logic signals for the trigger. The trigger \mathbf{PRHI} (\mathbf{PRLO}) is set if the energy deposited in the first layer exceeds a high (low) threshold. The signal \mathbf{SHLO} is set if the total calorimeter energy deposited exceeds another low threshold. These signals are used to construct electron and hadron triggers as shown in Figure 4.11.

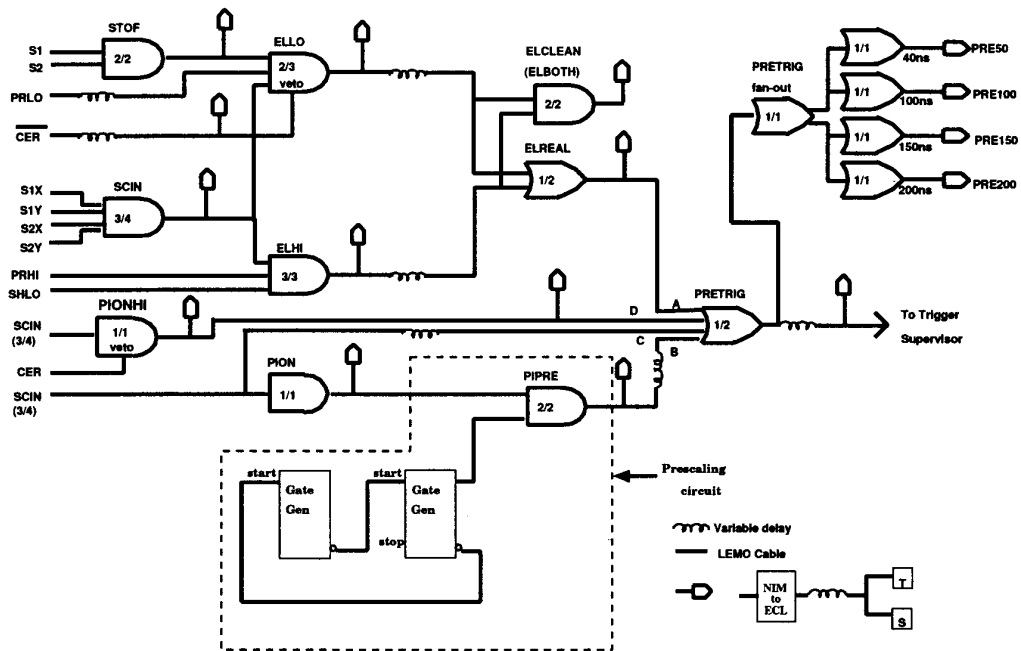


Figure 4.11 Schematics of the HMS trigger (figure from [82]).

- The “low” level electron trigger **ELLO**

ELLO is formed by requiring that at least two out of the three signals **STOF**, **PRLO** and **SCIN** are present. The presence of the Čerenkov signal is also required and the main difference between **ELLO** and **ELHI** is this particular requirement in the trigger.

- The “high” level electron trigger **ELHI**

This requires all of the following signals: **SCIN**, **PRHI** and **SHLO**. **ELHI** requires that an event not only has valid scintillator signal but also eliminates a significant fraction of the pions by placing a relatively strong restriction that the event has a large calorimeter signal. Thus, **ELHI** is primarily determined by the calorimeter.

- The electron trigger **ELREAL** is formed if either **ELHI** or **ELLO** is satisfied, while **ELCLEAN** requires both.

ELCLEAN is a strict electron trigger and needs both calorimeter and

Čerenkov signals present, and helps to greatly increase the pion rejection, thus providing a clean electron sample. There is an additional pion trigger, **PION**, which is basically **SCIN** vetoed by a Čerenkov signal. These triggers are prescaled away with a dynamical prescaling circuit to form **PIPRE** signal.

The raw spectrometer signal **PRETRIG** is formed, if **ELREAL** or **PIPRE** is satisfied. **PIPRE** is fanned out into four logic units with gate widths set between 40 and 200 ns. This allows a study of the electronic dead time. Copies of all of the logic signals are counted in scaler modules and sent to TDCs, making it possible to study the efficiency of separate trigger legs [83].

When a run starts, the first 1000 pedestal triggers are generated by **PEDPRETRIG**. Then the data acquisition starts to record physics events whenever a **PRETRIG** is formed. The raw spectrometer trigger and additional logic provided the final trigger for the Trigger Supervisor (TS) which generated the necessary ADC gates and TDC stop and start signals for the event. A pretrigger is formed for each event even if the TS was busy. The difference in the number of events actually processed by the data acquisition system and the number of pretriggers generated is due to the dead time, and will be further discussed in section 5.6.

The data acquisition system used for E03-103 was the CODA (CEBAF Online Data Acquisition) software package. Signals from detectors were processed by FASTBUS and VME crates which were then read out by a PC in the counting house. Data files contain both event information and slow control readouts. Scalers (the output quantities that are not necessarily associated with a particular track) were sampled every two seconds while the ADCs and TDCs were read out for each event. The slow controls are those with constant or slowly changing parameters (high voltage settings, beamline instrumentation, magnet settings, etc.) and are read by EPICS [84]. The DAQ queried the EPICS database for these values, formed an EPICS event and injected events into the data stream every 30 seconds.

CHAPTER 5

DATA ANALYSIS

The goal of the E03-103 data analysis is to determine the inclusive cross sections and cross section ratios from the raw data recorded during the experiment. This chapter will discuss the analysis methodology starting with analysis software and event reconstruction. Then it will discuss the calibration of individual detectors, and efficiencies of the cuts, followed by a detailed description of the cross section extraction.

5.1 The Analysis Software

The standard Hall C analysis code, ENGINE [85] was used to process the raw data files. It reads the raw data written by the data acquisition system, decodes the detector hits, locates possible tracks and particle identification information for each event, and calculates different physics variables. Input and output of the ENGINE are handled using the CEBAF Test Package (CTP). ENGINE makes use of CERN HBOOK libraries and provides output as ASCII report files (scalers, integrated charge ...), histogram files (ADC/TDC spectra for different detectors) and the reconstructed event-by-event data as ntuples. Most of the analysis software is written in FORTRAN (except for CTP and some machine-dependant routines). After obtaining the output from ENGINE, stand-alone FORTRAN and PAW codes were used to calculate physics quantities of interest.

The Hall C ENGINE consists mainly of four parts: initialization, main event loop, event reconstruction and output. It starts by reading the main configuration file which contains several run time flags and pointers to the data file, the output file,

and various parameter files. Then output file names are given as well as their format (ASCII, histograms, ntuples ...). After initialization is completed, the ENGINE starts looping through the events, in the main event loop.

In the main event loop, the events are processed according to the event type (scaler, EPICS or physics event). For a scaler event, the total counts for a given quantity are recorded and the hardware scaler counts are updated. Also the total charge and run time are computed. If the event is an EPICS event (Experimental & Physics Industrial Control System), the EPICS variables are dumped to ASCII files and analyzed separately. Then the physics events are analyzed. At the start of each run, 1000 pedestal triggers are taken. These triggers are generated by a pulser, and are used to determine the pedestal values for each ADC channel. The raw detector hits are read and passed to the main reconstruction routine where the events are reconstructed. This involves obtaining and storing the tracking and particle identification informations. The desired physics quantities are calculated for each event, and the corresponding histograms are filled. There are also routines record statistics in order to compute the efficiency of each detector element.

Event reconstruction proceeds as follows. The hodoscope ADC and TDC signals are decoded and corrected for gains, offsets, etc. This information is used to determine the velocity of the incident particle and the time at which it passed through the drift chambers. This determines the start time for the event. After this, information from all other detectors are decoded, and track-independent quantities are calculated. Next the tracking routine is called. The charged particle trajectories are reconstructed using information from the drift chambers. Track-dependent quantities (focal plane positions, angles, etc.) are calculated for each track. Then for each track, the time-of-flight is recalculated using hodoscope hits that lie near the track. The particle velocity is calculated and from its momentum (as determined by track reconstruction), the mass of the particle can be calculated. Other quantities used for particle identification are then calculated for each track. A series of cuts are made to reject bad tracks (the χ^2 fit to the track, energy loss, particle velocity, etc.). During the analysis we use a different set of cuts to select electrons. This will be

further discussed in section 5.7. Using the optical properties of the spectrometer, the particle's track is propagated backwards through the spectrometer to find the positions and momenta at the interaction vertex. The energy of the particle, which is computed from the track momentum, is corrected for the average energy loss during this process. After the HMS tracks have been reconstructed, CTP routines are called, which evaluates the user defined tests and increments the scalers and histograms.

At the end of the analysis, several routines are called to determine tracking and detector efficiencies. Finally the ENGINE writes several different output files. The scaler report files contain accumulated charge, estimated detector efficiencies, computer and electronic dead time, etc. The histogram files contain a summary of the detector's performance, while the ntuples contain event-by-event information. A detailed overview of the analysis ENGINE can be found in [34].

5.2 Event Reconstruction and Tracking

Determination of particle's trajectory and momentum involves finding the trajectory in the detector hut and then propagating that trajectory back to the target. The detectors directly measure the particle position and angle (relative to the central ray) in the detector hut after passing through the magnetic elements of the spectrometer. The trajectory of the particle is measured by two drift chambers, and the absolute positions of the drift chambers are known from a survey. The position of the particle passing through a drift chamber plane is obtained by adding the hit wire position to the drift distance of the particle. A detailed description of tracking can be found in [86].

At least 5 of the 6 planes in each chamber are required to have one or more single wire "hits" before tracking is attempted. All intersections of non-parallel pairs of wires that were hit in each chamber are identified and used to form "space points". The space points within a chamber are then linked to form "stubs", which are a track fragment through a chamber. Each hit has a left-right ambiguity because of the radial symmetry of the field. To solve this left-right ambiguity, the tracking

algorithm performs a χ^2 minimization to fit a straight line through both chambers with the requirement that the resulting track is consistent with the stubs in each chamber. However, the minimum χ^2 criteria does not always give the right track. New algorithms were developed [86] to tackle this situation and the E03-103 analysis was done with this new algorithm.

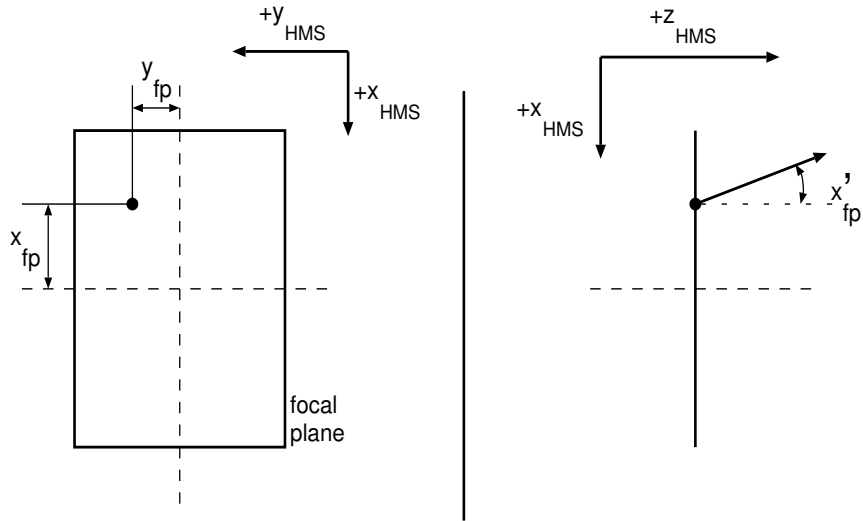


Figure 5.1 Schematics of focal plane quantities: the right panel shows the side view and the left panel shows the front view.

Once a particle is tracked, its focal plane quantities are determined. The “focal plane” is located near the midpoint of the two drift chambers, and is not the true optical focal plane of the spectrometer [87]. Projecting the fitted track to the focal plane yields the position (x_{fp}, y_{fp}) and slopes (x'_{fp}, y'_{fp}) for the particle track at $z = 0$.

Using the focal plane quantities one can reconstruct the fractional momentum of the particle ($\delta = \frac{p-p_c}{p_c}$, where p_c is the central momentum of the spectrometer), the position and slope in the non-dispersive plane (y_{tar}, y'_{tar}) and the position and slope

in the dispersive plane (x_{tar}, x'_{tar}) of the event in the target. The reconstruction of the position, angle and relative momentum are carried out using a Taylor expansion (in focal plane variables) of the solutions of the equation of motion of a charged particle in the magnetic field of the spectrometer. The reconstruction transformation for each target quantity is a multidimensional polynomial up to 6th order, and the transfer coefficients are called matrix elements. Thus, the target quantities are related to the focal plane quantities by the following equation

$$x_{tar}^i = \sum_{j,k,l,m}^{j+k+l+m \leq 6} M_{jklm}^i (x_{fp})^j (y_{fp})^k (x'_{fp})^l (y'_{fp})^m. \quad (5.1)$$

The matrix elements M_{jklm}^i are optimized using an iterative fitting procedure, where the starting model is a COSY INFINITY calculation [88]. The projected slopes relative to the spectrometer's coordinate system are converted to the scattering angle relative to beam axis using the following equation:

$$\cos \theta = \frac{y'_{tar} \sin \theta_c + \cos \theta_c}{\sqrt{1 + x_{tar}'^2 + y_{tar}'^2}} \quad (5.2)$$

where θ_c is the central angle of the spectrometer.

5.3 Detector Calibrations

Calibration analysis helps to achieve a consistent treatment of the detector responses for the entire data set. Hodoscope signal velocities and timing offsets are first determined. This ensures a proper start time for the drift chamber and allows for the proper calculation of drift distances using the drift time. Calibration of the Čerenkov detector requires normalization of signals from each phototube. Calibration of the lead glass calorimeter is needed because of possible gain variations between different modules and the attenuation in the lead glass block. What follows is a brief discussion of the various software calibrations. A detailed account of the procedures involved can be found in [34, 89, 90].

5.3.1 Hodoscope Timing Calibration

Scintillator hodoscopes provide a clean trigger for the DAQ system and are used to get the time of flight (TOF) of a particle in the spectrometer. To determine the actual time when a particle hits a scintillator paddle, one needs to convert the TDC signal of a hit to the time of the hit. Since the timing signal comes from a fixed threshold discriminator, the exact time at which the threshold is exceeded depends on the height of the signal, and these corrections are called pulse height corrections. To do these corrections, mean time information from crossed pairs of scintillators are used. Another correction is the variation in the propagation time for the signal in the paddle. Once the pulse height correction is known, the velocity of light propagation along the scintillator can be measured by taking the difference in the hit times of the PMTs on the opposite sides of the scintillator bar. This difference, in general, depends on the index of refraction and the geometry of the scintillator. In addition to these corrections one needs to account for different offsets (due to variations in cable length and different response times) for each PMT. These corrections were made with a standalone offline calibration routine originally developed for the SLAC NE18 experiment which is modified for use in Hall C [89]. Once these corrections are applied, the relativistic velocity of the scattered particle between the two scintillator planes should agree with the velocity of the particle determined using the TOF. For E03-103, the TOF calibration was done using one run and it was verified that the β ($= \frac{v}{c}$) distribution peaked at 1, as expected for high energy electrons. It should be noted that during E03-103, the spectrometers were detecting negative particles with momenta too high to cleanly separate pions from electrons using only a TOF cut.

5.3.2 Čerenkov Counter Calibration

Calibration of the Čerenkov detector requires normalization of the signals from the phototubes. The normalization is accomplished by selecting electrons in the spectrometer, and converting the ADC signal to the number of detected photoelectrons. In order to perform the conversion, the ADC channel number corresponding

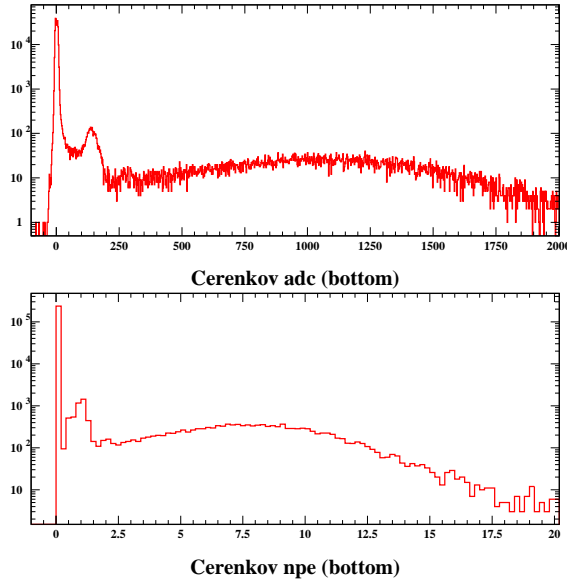


Figure 5.2 A typical ADC distribution from the bottom PMT in the HMS Čerenkov detector. The plot in the bottom panel is the calibrated photoelectron distribution. The pronounced peak around 1 is due to the single photoelectron peak.

to one photoelectron is needed. Figure 5.2 shows a representative ADC spectrum from Čerenkov detector. The pedestal-subtracted ADC readout from the PMTs was scaled to units of photoelectrons using a calibration constant, and this is also shown in Figure 5.2. The single photoelectron peak is found by fitting the ADC distribution with a Gaussian. For E03-103, we used a single run to calibrate the Čerenkov detector. The stability of the single photoelectron peak was checked for each analyzed run and found to be stable at the 5 – 10% level.

The sum of the photoelectrons from both tubes serves as the Čerenkov signal. Putting a constraint on the number of photoelectrons helps to distinguish between electrons and pions. However, later it was found that the Čerenkov counter’s response had some position dependence. Small misalignments of the mirror combined with the relatively low gas pressure (leading to a relatively small total number of photoelectrons) resulted in non-uniform photoelectron yield across the acceptance. This was apparent near the overlap of the two mirrors as well as at the edges of the acceptance and will be further discussed in section 5.7.4.

5.3.3 Drift Chamber Calibration

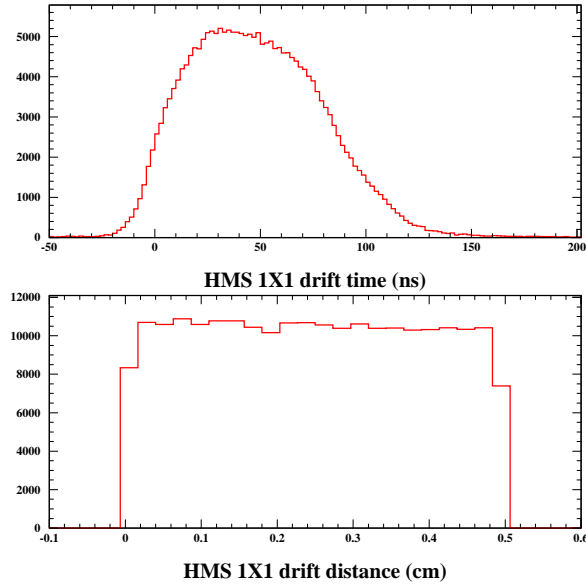


Figure 5.3 Drift time and drift distance distribution for one of the X planes of the HMS drift chambers. The drift time can be negative, because the overall offset between the times measured by the drift chamber and the time measured by the hodoscope is not removed. The apparent reduction of counts in the extreme bins are caused by partial overlap of those bins in the 0.5 cm region (in the bottom panel).

The drift chamber provides tracking information for particles entering the spectrometer. The raw output is in the form of a list of hits for each event, along with the TDC values for each event. Using hodoscope time information as a TDC (STOP), the drift chamber TDC (START) value can be converted into drift time. To determine the distance between the sense wire and the trajectory of the particle, the drift velocity per chamber has to be known.

To determine how far the hit is from a sense wire (drift distance), the following procedure is used [34]. The TDC values from all wires in a given plane are taken for a large number of events (~ 50 k). This gives the drift time spectrum $F(t)$ as shown in the upper panel of Figure 5.3. Though the drift position distribution over a single cell is non-linear, it was assumed that after averaging over all cells, the distribution is linear. After applying a loose cut to reject random noise hits, the time

spectrum is integrated to get the distance spectrum.

$$D = D_{\max} \frac{\int_{t_{\min}}^T F(t) dt}{\int_{t_{\min}}^{t_{\max}} F(t) dt}, \quad (5.3)$$

where D_{\max} is the maximum possible distance (half of the cell width = 0.5 cm), t_{\min} and t_{\max} are the limits of the time interval corresponding to D_{\max} , T is the time recorded by the TDC and $F(t)$ is the measured drift time distribution. Since the probabilities that a hit will occur at every point of the cell surface are equal, the drift distance distribution should be flat. A typical example of the drift distance distribution is shown in the bottom panel of Figure 5.3.

For each plane of drift chambers, a time-to-distance map was created. For E03-103, time-to-distance calibrations were performed for several runs and checked for each analyzed run. Since the deviations caused by electronics, temperature variations and other factors were negligible, it was decided to use a single time-to-distance map for all runs.

5.3.4 Calorimeter Calibration

For E03-103, the calorimeter was used to distinguish electrons from pions. As mentioned earlier, an electron deposits all its energy into the calorimeter, while a pion deposits a constant amount of energy per layer. Since each block was read only by one PMT (first 2 layers are read out on both sides), this gave a signal variation with the distance of the hit from the PMT. This attenuation was corrected by multiplying the signal with a factor based on the hit position. Besides this attenuation correction, the gain of each module must be calibrated. This calibration was performed using a sample of very high energy electrons.

The measured ADC values are translated into energy by summing over the signal from each ADC after multiplying by a calibration constant specific to that channel. The calibration constants are found by minimizing the difference between the energy as determined by the tracking information and the energy of the electron summed over the entire calorimeter. This is done with a pure sample of electrons

(selected with a strong cut on the number of photoelectrons of the Čerenkov detector). For E03-103, a single set of calibration constant was generated and used for all runs.

5.3.5 BCM Calibration

As mentioned in section 4.2.3, the beam current was continuously monitored using two BCMs and the Unser monitor. The total beam charge is the time integral of the beam current. Since the Unser monitor has a very stable gain (but a drifting offset), the BCMs (which have a slight drift in gain) are calibrated with respect to the Unser monitor. To convert the scaler data from the current monitors into current and charge measurements, we need to know the gain and the offset. The current is given by

$$I = G \times (\nu_{on} - \nu_{off}), \quad (5.4)$$

where ν_{on} is the frequency of the device (BCM2, Unser) when the beam is on and ν_{off} the frequency when the beam is off, and G is the gain of the device.

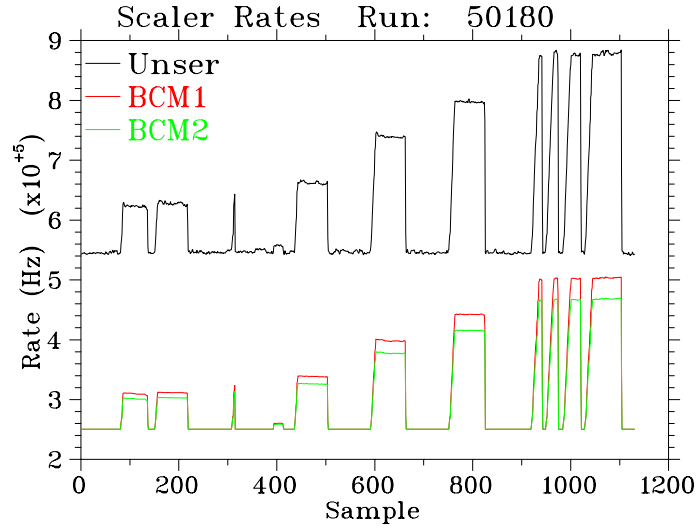


Figure 5.4 An example of a BCM calibration run showing the beam on and off periods. Alternate beam on and off periods help to determine the drift in the Unser offset over the course of a run.

For a BCM calibration run, the beam is turned off and on over ≈ 2 minute

time intervals with a known increment in the beam current as shown in Figure 5.4. The absolute value of the current is calculated using the Unser, and its known gain combined with the beam on and off frequencies. The beam-off frequency is obtained by averaging over two beam-off periods just before and after a beam on period. This gives the current of the Unser through Eqn. 5.4. If one plots the current vs the BCM beam on frequencies, then the slope of the curve is the gain of the BCM and the intercept will give information about the offset (beam-off frequencies). This offset and gain can be used to measure the current during a run. The product of the current and beam-on time results in the total integrated charge for that run.

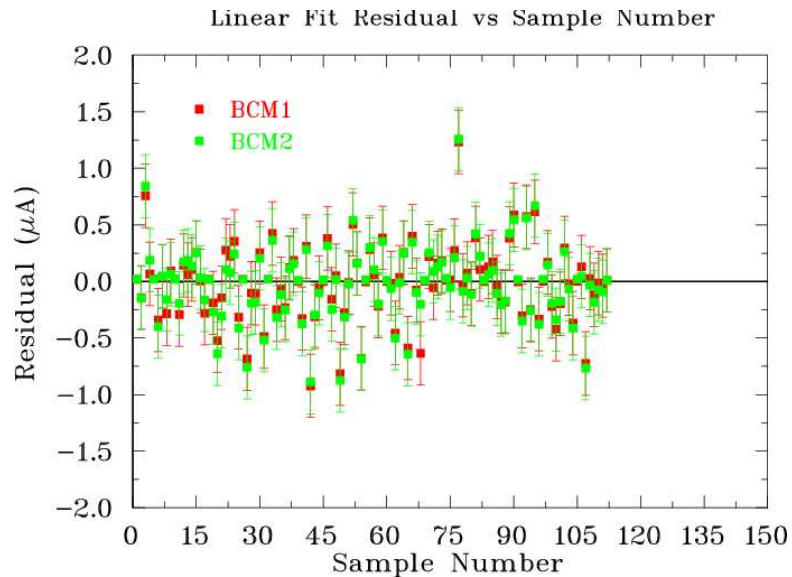


Figure 5.5 Residuals of the BCM calibration with respect to the global calibrations over the course of run period [91].

Several BCM calibrations were made over the course of the run period and gave consistent calibration factors. A global calibration was made using all the individual BCM calibration runs. This global calibration was used to compute the charge for all runs. More details about the BCM calibrations for E03-103 can be found in [83, 91]. The residuals from the individual BCM calibrations relative to the global calibration are shown in Figure 5.5, and the scatter in the plot represents

the uncertainty of the measurement of beam current ($0.25 \mu\text{A}$). Additional systematic uncertainties are due to calibration techniques and possible beam losses between BCMs and target (see section 5.14).

5.4 Kinematic Offsets and Corrections

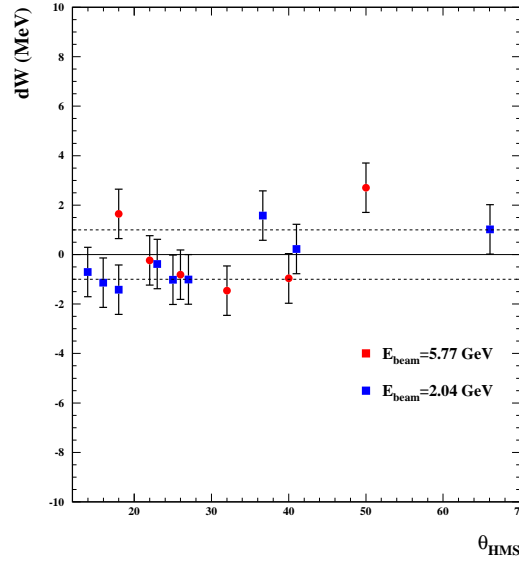


Figure 5.6 The figure shows the computed dW values (after applying appropriate kinematic offsets) plotted against scattering angle at two different beam energies. Here, dW is the difference between the measured invariant mass and proton mass.

Since the electron-proton elastic scattering process is kinematically constrained, it can be used to reduce the uncertainties in the kinematic parameters (angles, incident and scattered momenta, etc.). In addition, due to the large body of elastic scattering data, it can also be used to check the absolute cross section normalization. The nominal electron beam energy (E) was measured with the Hall C arc energy measurement, the scattered momentum (E') is obtained from the field to momentum conversion code for the HMS dipole, and the nominal scattering angles (θ) were read from the floor using a vernier scale attached to HMS. In order to reduce the uncertainties in the kinematic settings, possible offsets in the above mentioned

observables must be determined and should be corrected in the analysis.

During E03-103, several electron-proton elastic scattering runs were taken. In this case, the invariant mass W of the final hadronic state is equal to the proton mass (M). Thus,

$$W^2 = M^2 + 2M(E - E') - 4E E' \sin^2(\theta/2). \quad (5.5)$$

The difference between the proton mass and the calculated value of W (*i.e.* $\Delta W^2 = W^2 - M^2$) is due to offsets in E , θ or E' .

$$\Delta W^2 = \frac{\partial W^2}{\partial E} \delta E + \frac{\partial W^2}{\partial E'} \delta E' + \frac{\partial W^2}{\partial \theta} \delta \theta, \quad (5.6)$$

where δE , $\delta E'$ and $\delta \theta$ are the offsets in the beam energy, scattered momentum and scattering angle respectively. For each elastic scattering run, ΔW^2 has been calculated after correcting for the effects of ionization energy loss in the target. Additionally, small peak distortions due to radiative effects were also taken into account. Then the partial derivatives in Eqn. 5.6 were computed. Using a χ^2 minimization, these partial derivatives (note that, the calculations are done with fixed E) were fitted to determine the best kinematic offset which could reproduce the measured value of ΔW^2 . For E03-103, a combined fit of 2.01 GeV and 5.77 GeV data resulted in $\delta E' = -0.1\%$ and $\delta \theta = -0.4$ mrad [92]. These offsets are taken into account by correcting the relevant input parameter files in the ENGINE. Figure 5.6 shows the difference in proton mass and computed W values after applying the kinematic offsets. After applying the offsets, the difference between W and M is ≈ 1.5 MeV, which implies that the kinematics offsets are fairly well understood and accounted for in the analysis. The precision in determining the kinematic variables based on this analysis and previous Hall C data were estimated to be 0.5 mrad for the angle, 5×10^{-4} for the beam energy and 5×10^{-4} for the scattered energy.

As mentioned earlier, the elastic cross sections measurements can be used to verify the accuracy of the spectrometer acceptance and to check the agreement with the charge normalized yields. For E03-103, we used SIMC (for more details see [93, 82]), the standard HALL C Monte Carlo in the single arm mode, to study

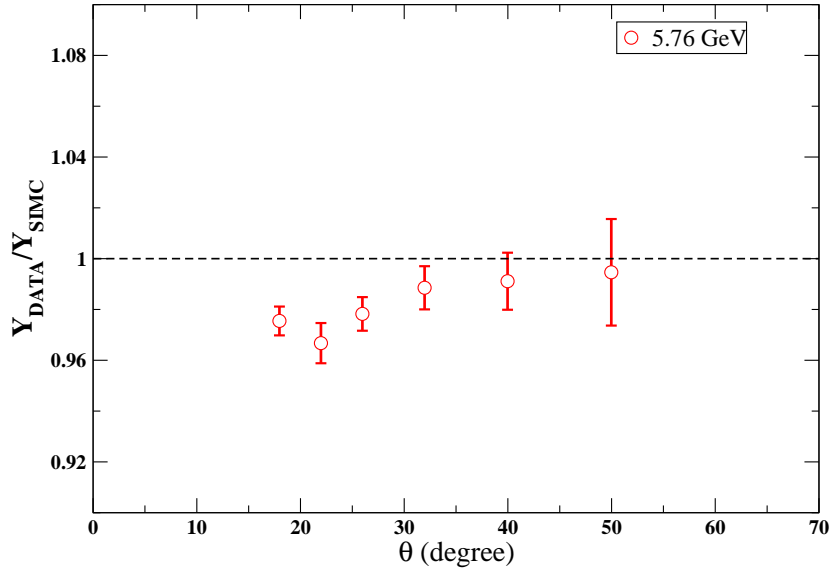


Figure 5.7 The ratio of experimental and Monte Carlo $H(e, e')$ normalized yields for the elastic data are shown in the figure. The error bars are statistical only.

the $H(e, e')$ elastic reaction. SIMC uses an elastic cross section parameterization [94] and also includes radiative corrections, multiple scattering and energy loss in the simulation. In order to compare data to the Monte Carlo, the data are corrected for all the dead times and efficiencies. The usual cuts on the reconstructed spectrometer variables and particle ID cuts are also applied. A loose cut on the invariant mass is used to make sure that the W spectrum contains true elastic events. For most of the elastic runs, dummy target data were also taken. The dummy yield is scaled to account for the thickness difference between the cellwall and the aluminum foil, and is subtracted from electron yield.

Figure 5.7 shows the ratio of the normalized experimental yield and the equivalent Monte Carlo normalized yield. The agreement between data yields and Monte Carlo yields suggests good knowledge of the acceptance and of the overall normalization.

Individual detector distributions in δ , $hsxptar$, $hsyptar$ and W with respect to the data are compared with corresponding Monte Carlo distributions. A representative plot of the comparison is shown in Figure 5.8. Agreement between the

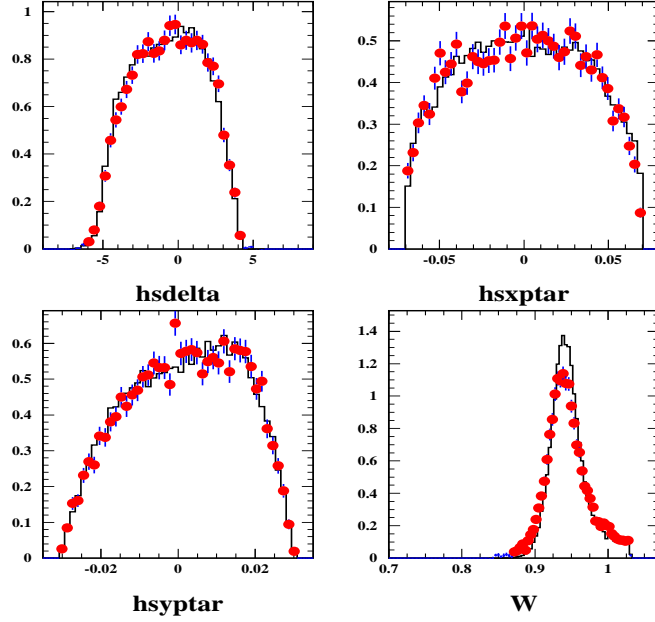


Figure 5.8 Experimental and Monte Carlo $H(e, e')$ distributions for one of the elastic settings (40 degree). Symbols represent data points while the solid curve represents the detector distribution. Error bars are statistical. Here, $hsdelta$ is the relative deviation from the central momentum, $hsxptar$ and $hsyptar$ are the out-of-plane and in-plane slopes of the reconstructed tracks, and W is the reconstructed invariant mass.

distributions indicates that the acceptances of the spectrometer components are well understood.

5.5 Methodology of Cross Section Extraction

The measured differential inclusive electron scattering cross section is given by:

$$\frac{d\sigma}{dE' d\Omega} = \left(\frac{1}{Q \rho t N_A/M} \right) \left(\frac{1}{\varepsilon} \right) \left(\frac{PS}{LT} \right) \left(\frac{(N^{e^-} - BG)}{\Delta E' \Delta \Omega} \frac{1}{A(\delta, \theta)} \right). \quad (5.7)$$

- In the equation above, the first factor normalizes the counts to the total number of electrons, Q , incident on the target and to the number of nuclei of the target

material. Here, ρ is the density, t is the thickness, M is the atomic mass of the target and N_A is Avogadro's number.

- The second factor corrects the number of counts for the inefficiencies in the trigger and software. Here, $\varepsilon = \varepsilon_{trig} \times \varepsilon_{track} \times \varepsilon_{cer} \times \varepsilon_{cal}$, where ε_{trig} corrects for the inefficiencies of various elements in the trigger logic, ε_{track} is the tracking efficiency. ε_{cer} and ε_{cal} represent the efficiency of the software cuts used to define the electron sample by the Čerenkov and calorimeter in the analysis.
- The third factor corrects the number of counts for the inefficiency in the DAQ system. Here, PS is the prescale factor, and $LT = LT_{comp} \times LT_{elec}$, where LT_{comp} and LT_{elec} are the computer and electronic dead times, respectively.
- The last factor represents the count density of electrons. N^{e^-} is the number of scattered electrons observed in the solid angle, $\Delta\Omega$, in the energy range, $\Delta E'$, and BG represents the background events to be subtracted from the observed electron spectra, and $A(\delta, \theta)$ is the acceptance correction.

Since we would like to measure the primary electrons which are coming from the interaction vertex, we have to first subtract the background electrons. This background is mainly comprised of secondary electrons that are created from charge symmetric processes (see section 5.8.3), and for cryotargets, events that originate from the cellwalls. The positron runs are taken with the **ELCLEAN** trigger, and we have to account for the relative inefficiency (since the electron runs are taken with **ELREAL** as main trigger) of this trigger. This is applied as a normalizing factor in the yield calculation.

In general, the efficiency-corrected charge normalized yield for a run is given by

$$Y_{\text{data}} = \frac{N}{\varepsilon Q_{\text{tot}}}, \quad (5.8)$$

where N is the total number of events, ε is the total combined efficiencies, and Q_{tot} is the total accumulated charge in mC. In order to form the charge normalized yield

for an electron run, we proceed as follows:

$$Y_e = Y_{(e^-, \text{elreal})} - \left[\frac{Y_{(e^-, \text{elreal})}}{Y_{(e^-, \text{elclean})}} \right] \times Y_{(e^+, \text{elclean})}. \quad (5.9)$$

In the equation above, the notation is as follows: $Y_{(e^-, \text{elreal})}$ is the yield of an electron run taken with **ELREAL** trigger, $Y_{(e^-, \text{elclean})}$ is the yield of an electron run taken with **ELCLEAN** trigger, and $Y_{(e^+, \text{elclean})}$ is the yield of a positron run with the **ELCLEAN** trigger. For a cryotarget, we need to subtract the cellwall contribution (we use dummy aluminum target for this, see section 5.8.1). The yield of an electron run with dummy aluminum target is

$$Y_{\text{ed}} = Y_{(\text{ed}^-, \text{elreal})} - \left[\frac{Y_{(\text{ed}^-, \text{elreal})}}{Y_{(\text{ed}^-, \text{elclean})}} \right] \times Y_{(\text{ed}^+, \text{elclean})}. \quad (5.10)$$

The final yield after charge symmetric background and cellwall subtraction is given by

$$Y = Y_e - f_{\text{dummy}} \times Y_{\text{ed}}, \quad (5.11)$$

where f_{dummy} is a correction factor to account for the geometric difference and thickness between the aluminum slab and the cellwall. The following sections will discuss how the corrections are estimated and accounted for in the data analysis.

5.6 Dead Times

For ideal data acquisition, after an event is read, the individual detector elements should be ready to detect another event instantaneously. However, the trigger electronics and the DAQ computers take a finite amount of time to process each event and one must correct for events that are lost or not recorded during this processing time. In general, dead times can be classified into two categories: extendable and non-extendable. A system is extendable if the hits occurring during the dead interval can extend that interval, but a non-extendable system will simply ignore the new inputs while processing an event. In Hall C, the dead times are divided into two groups: computer dead time arising from the trigger supervisor busy signal, and electronic dead time which is due to a missed trigger because an

event creates a hardware level trigger while the gate from the previous event is still active. The following sections briefly discuss how dead times are corrected in the E03-103 analysis, and a more thorough discussion about dead times and how these are applied to Hall C DAQ can be found in [93, 34, 80].

5.6.1 Electronic Dead Time

When a trigger is formed, the logic modules produce a logic busy level for a duration of time called a gate width (τ). If a module is active, and another event enters the spectrometer during this period, the module will simply ignore the latter event. Thus, during the period, τ , the module is effectively dead to any new input signal. This causes an electronic dead time.

In general, the actual number of events is not directly measured. If the true mean event rate is R (average number of events coming in per second), the probability of detecting n events in time interval t is given by Poisson statistics:

$$P(n) = \frac{(Rt)^n e^{-Rt}}{n!} \quad (5.12)$$

and the probability of the time between events is given by

$$P(t) = R e^{-Rt}. \quad (5.13)$$

For an electronic module of time width, τ , only those events arriving after a time interval τ are recorded. Thus, to get the fraction of time intervals greater than τ , the equation above should be integrated from the gate width τ to ∞ .

$$P(t > \tau) = R \int_{\tau}^{\infty} e^{-Rt} dt = e^{-R\tau}. \quad (5.14)$$

Thus, the measured event rate is given by

$$R_{measured} = R e^{-R\tau}. \quad (5.15)$$

In other words, the live time of the unit is given by

$$LT_{elec} = \frac{R_{measured}}{R} = e^{-R\tau} \approx 1 - R\tau, \quad (5.16)$$

where in the last step we assume $R\tau \ll 1$, and use a Taylor expansion. For E03-103, the rates are $\ll 1$ MHz, and $\tau = 60$ ns and, thus, $R\tau \ll 0.06$. (For most modules the typical time width is 40 ns. However, it was found that the effective hodoscope gate width was varying between 50 and 60 ns. To ensure a well defined gatewidth, the limiting gate width was defined by the **PRETRIG** gate, which was set at 60 ns).

To determine the electronic dead time of the trigger, copies of the trigger signals are generated with gate widths of 50, 100, 150 and 200 ns (also see the upper-right corner of Figure 4.11). These signals are fed to scalers, and can be used to extrapolate to zero gate width, thus determining the dead time correction. The “true” number of counts is

$$N_{true} = N_{measured} + (N_{PRE100} - N_{PRE150}) \frac{60 \text{ ns}}{50 \text{ ns}}, \quad (5.17)$$

and the electronic live time is

$$LT_{elec} = \frac{N_{measured}}{N_{true}} = 1 - \left(\frac{N_{PRE100} - N_{PRE150}}{N_{PRE100}} \right) \frac{6}{5}, \quad (5.18)$$

where it is assumed that $N_{PRE100} = N_{true}$, which is a reasonable approximation since the dead times are quite small. The electronic live time as calculated in the HMS is shown in Figure 5.9.

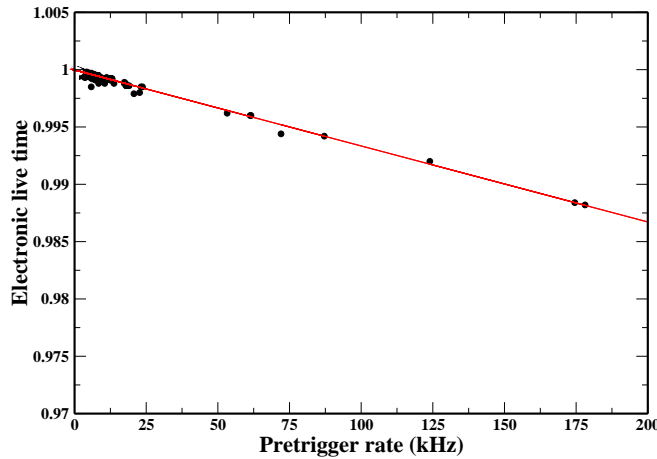


Figure 5.9 Electronic live time as a function of the pretrigger rate. The line shown is a fit of the form $1 - R\tau$ with $\tau = 66.2$ ns.

The experimental yields are corrected by multiplying the charge normalized yields with $\frac{1}{LT_{elec}}$ to account for the electronic live time. This was done on a run-by-run basis.

5.6.2 Computer Dead Time

The DAQ system requires a nonzero time interval to digitize and record the signals from detectors. Computer dead time occurs when the DAQ computers are busy processing events, and are not available for processing new events. This is an example of non-extendable dead time, since new events are ignored. The computer live time LT_{comp} is given by the ratio of number of triggers formed to the number of pretriggers¹

$$LT_{comp} = \frac{N_{trig}}{N_{pretrig}} = \frac{1}{1 + R\tau} \quad (5.19)$$

where R is the mean event rate, and τ is the “dead time” of the unit.

What follows is a brief discussion of the procedure for the dead time calculation for E03-103. Whenever a pre-trigger is formed, the signal is sent to the scalers and also to the Trigger Supervisor (TS) through the 8LM logic module. The TS provides all the control signals and acts as an interface between the DAQ and trigger hardware. The logic that went into processing the event by the TS is done externally using the 8LM and the input to 8LM includes **HMS PRETRIG**. Whenever the TS is busy, a **BUSY** signal is created and the output from the 8LM will not be processed until it is ready to accept a new event. Thus, the output of 8LM in the singles mode is **HMS TRIG** = **HMS PRETRIG** · AND · $\overline{\text{BUSY}}$. Then the computer live time is given by Eqn. 5.19 as the ratio of triggered to pre-triggered events. The trigger signal from the 8LM is processed by the TS where the event is either prescaled or read out to the ADC and TDC scalers.

During the E03-103 run period (especially for positron runs), it was found that the dynamical pion prescaling circuit **PIPRE** was behaving in an erratic manner

¹Triggers are number of events processed by the Trigger Supervisor while pretrigger is the total number of triggers reaching the 8LM module.

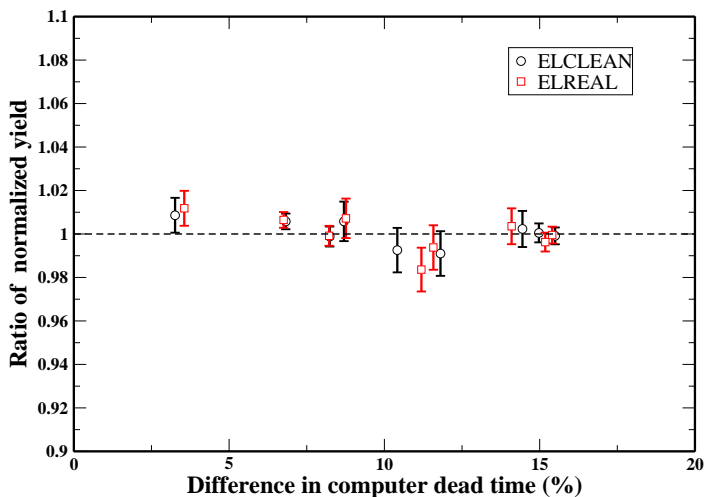


Figure 5.10 The ratio of luminosity normalized yields as a function of the difference in computer dead time. The plot shows the yield ratios for two different trigger types used in the E03-103 analysis. Error bars show statistical uncertainties.

resulting in huge, seemingly incorrect dead times. The calculation above (Eqn. 5.19) for the live time is valid for a single trigger type or multiple trigger types with more or less same rates. **PIPRE** was designed to give a maximum of 100 Hz at high **SCIN** rates and $\sim 2/3$ of the **SCIN** at low rates [34]. But it was found that one of the gate generators in **PIPRE** was malfunctioning and **PIPRE** was firing more often than expected. Recall that $\mathbf{PRETRIG} = \mathbf{ELREAL} \cdot \mathbf{OR} \cdot \mathbf{PIPRE}$ and this spurious triggering of **PIPRE** creates more **PRETRIG** signals. But at high rates the trigger supervisor is busy and it will inhibit the 8LM module due to this extra **PRETRIG** signals, thus increasing the apparent computer dead time. However, it should be noted that these “lost” events were predominantly **PIPRE** events.

During the data acquisition, the trigger signals are not only sent to scalers but also to the TDCs. These signals allow us to look at the TDC spectra in the defined range, and enables us to cut on individual (**ELCLEAN**, **ELREAL**, or **PIPRE**) spectra to calculate individual live times of different trigger legs. However, this calculation of live time is from the scaler read out just before forming **PRETRIG** but the pretrigger hardware gate width is little wider. Hence, it slightly overestimates the scaler number (for **ELCLEAN** trigger $\sim \frac{1}{10\text{ ns} \times \mathbf{ELCLEAN}_{\text{rate}}}$). This is negligibly

small under the experimental conditions. The TDCs are read out only every n^{th} time, where n is the prescale factor. For example, the computer live time for **ELREAL** trigger is

$$LT_{\text{comp}}^{\text{ELREAL}} = \frac{\text{TRIG}}{\text{PRETRIG}} \times \text{PS}, \quad (5.20)$$

where in this case TRIG is the trigger defined by **ELREAL** TDC, PRETRIG is the scaler value from the **ELREAL** scaler, and PS is the prescale factor.

In order to keep the dead time below a reasonable value the PS was adjusted by monitoring the rate in the DAQ system. If the PS is set to 1, the computer will attempt to process every trigger formed. If the PS is set to 10, the computer will process only every 10th trigger. A study of the computer dead time was done by taking data at the same spectrometer kinematic setting but with different prescale factors. This was repeated for several other kinematic settings. The data were corrected for all the dead times and efficiencies, and a luminosity normalized yield was formed. If the computer live time is measured properly then the luminosity normalized yields should be independent of computer live time. Figure 5.10 shows the ratio of luminosity normalized yields of these runs. Here the abscissa represents the percentage difference in computer dead time (caused by a change in prescale factor). From the figure it is clear that even if the computer dead time differs by $\sim 16\%$, the luminosity normalized yields are reproducible to better than 1%.

5.7 Efficiencies

For E03-103, we used Čerenkov counter and calorimeter detectors to distinguish electrons from other negatively charged particles by applying particle identification (PID) cuts. When we apply these cuts, there is a possibility that we may lose some valid events, and this must be included in the analysis. There can be additional loss of real events because of inefficiencies in the trigger circuit or due to the inefficiency of tracking algorithm to find a valid track. The following section gives a brief overview of the efficiencies of the detectors and PID cuts.

5.7.1 Trigger Efficiency

The trigger (see Figure 4.11) was designed to be efficient for electrons while suppressing other particle types. However, true electron events can be lost due to inefficiencies of the detectors used for the HMS spectrometer. The PID legs of the trigger require that either Čerenkov or the calorimeter register a hit. In the analysis we used stricter PID cuts than the PID trigger requirements, hence, no additional events were lost due to trigger inefficiencies from the Čerenkov counter or calorimeter. This means that the triggers lost because of the inefficiency of the PID leg are effectively included in the PID cut efficiency at the analysis level. However, we still need to account for the scintillator efficiency. The 3 out of 4 scintillator efficiency is given by

$$\begin{aligned} P_{3/4} &= P_1 P_2 P_3 P_4 + P_1 P_2 P_3 (1 - P_4) + P_1 P_2 (1 - P_3) P_4 \\ &+ P_1 (1 - P_2) P_3 P_4 + (1 - P_1) P_2 P_3 P_4, \end{aligned} \quad (5.21)$$

where P_n represents the efficiency of the n^{th} scintillator plane. The efficiency of a given plane can be calculated with an unbiased sample prepared by requiring hits in the other three planes. Then, P_n is defined as the fraction of events hit in the n^{th} plane divided by total number of events in the unbiased sample. Also, there can be position-dependent inefficient regions for a hodoscope, and this might cause an acceptance-dependent trigger inefficiency. This was investigated [83] and the effect was found to be small for E03-103 kinematics. The 3 out of 4 scintillator efficiency was found to vary from 0.993 to 0.991 depending on the setting. It was decided to use a single efficiency, 0.992, for all the analyzed runs.

5.7.2 Tracking Efficiency

The normalized yields must also be corrected for inefficiencies in the tracking. A track can be missed due to a failure in the tracking algorithm. There is also an intrinsic inefficiency associated with the drift chamber to produce a signal, and this is common to all types of particles. The failure of the tracking algorithm to produce

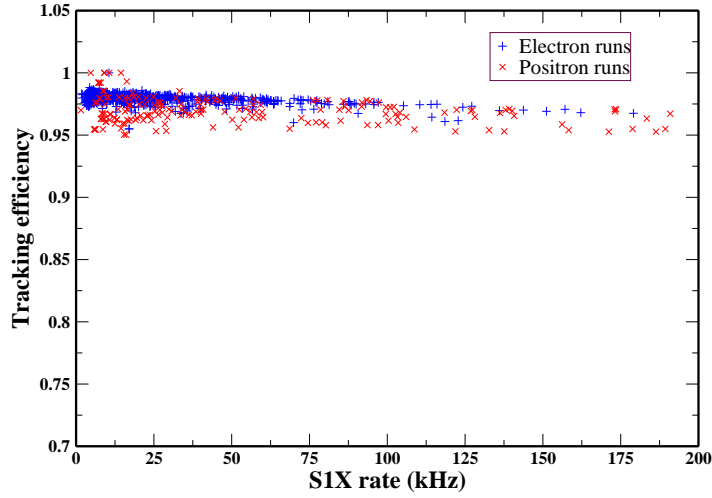


Figure 5.11 Tracking efficiency as a function of scintillator (S1X) rate.

a valid track is mainly because of insufficient or an excess of background information. If too many wires fire, then there is an increased probability that noise hits will be included in the calculation. On the other hand, if too few wires are fired then the left-right ambiguity cannot be resolved, thus preventing the reconstruction of an unambiguous track.

The tracking efficiency is calculated as follows. A “fiducial” area is defined using the scintillators (paddles 4 to 13 in X planes and 4 to 7 in Y planes). This guarantees that the particle passed through the central area of the acceptance (hence, the tracking efficiency is also known as the fiducial efficiency). Then the fiducial efficiency is calculated by taking the ratio of number of events for which a track is found and the expected number of tracks that should have been found:

$$\varepsilon_{track} = \frac{N_{did}}{N_{should}}, \quad (5.22)$$

where N_{should} is the number of events forming a valid trigger that satisfy the PID criteria used to select electrons. PID is incorporated (which includes a tight cut on Čerenkov detector and a cut on the total deposited energy in the calorimeter) in these calculations, because the scintillators are more sensitive to “noise” hits from low energy particles that are not associated with scattering at the target. N_{did} is satisfied whenever the tracking algorithm finds a track and N_{should} is valid.

The tracking efficiency calculated for each run as a function of the rate in the first scintillator layer (S1X) is shown in Figure 5.11. For E03-103, data are corrected for tracking inefficiency on a run-by-run basis.

5.7.3 Calorimeter Cut Efficiency

<i>hsshsum</i>	> 0.7
<i>hcer_npe</i>	> 1.5

Table 5.1 Particle identification cuts used in the analysis. Here, *hsshsum* is the ratio of total energy deposited in the calorimeter and the reconstructed energy of the particle, and *hcer_npe* is the number of photoelectrons produced by an event in the Čerenkov detector.

The calorimeter is used in conjunction with the Čerenkov counter in order to distinguish electrons from other charged particles. It is important to know how many otherwise valid events are lost when we place a cut on the calorimeter distribution. In order to find the number of electrons lost due to the calorimeter cut, it is crucial that we have a clean and unbiased sample of electrons (to avoid the π/e dependency on the efficiency calculation, since pions can be misidentified as electrons and bias the estimation). Since we want to study the efficiency of the calorimeter, we need to prepare the sample without using the calorimeter.

For E03-103, we used elastic scattering runs to determine the calorimeter cut efficiency. This is quite useful since we can isolate an extremely clean sample of electrons by requiring an additional condition on invariant mass, W . One drawback is that elastic scattering does not necessarily cover the full acceptance of the spectrometer. However, we were able to use δ scan² runs to verify that the cut efficiency is uniform across the acceptance. Then the calorimeter efficiency for a nominal cut

²Elastically scattered electrons tend to populate only a narrow region in the acceptance of the spectrometer. However, this narrow region can be moved across the acceptance by changing either the angle or E' , allowing one to map out the response of the spectrometer throughout the acceptance. This procedure is known as δ scan.

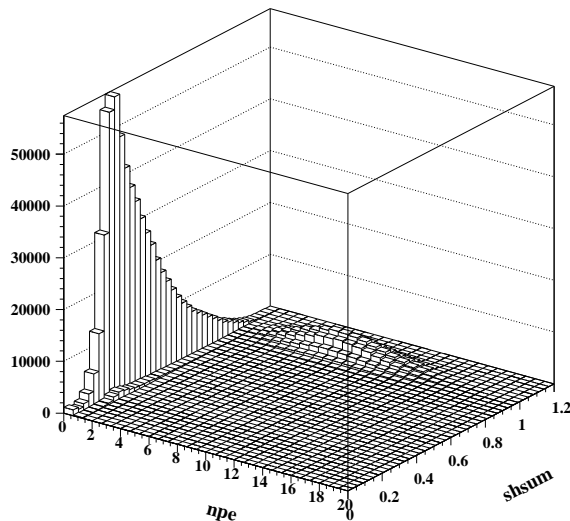


Figure 5.12 The figure shows the two-dimensional distribution of the Čerenkov signal vs the calorimeter response. Shown is the number of photoelectrons in the Čerenkov detector (npe) vs normalized shower counter spectrum ($shsum$). The peak that is visible near $npe \sim 0$ is due to pions while the electron distribution is visible around $shsum \sim 1$.

at $hsshsum > 0.7$ is defined as

$$\varepsilon_{calorimeter}^{cut} = \frac{N_{(all \& hsshsum > 0.7)}}{N_{(all)}}, \quad (5.23)$$

where $N_{(all)}$ is the total number of elastically scattered electrons passing cuts $abs(W - 0.93827)$, $hcer_npe > 10$ and $\mathbf{ELLO} > 100$. Note that, these cuts are applied in addition to the cuts defined in Table 5.3. These restrictions on the distributions make sure that we have a relatively clean sample of electrons. A cut on the \mathbf{ELLO} TDC ensures that the sample is derived using minimum information from calorimeter signal (as opposed to \mathbf{ELHI} leg of the trigger circuit, see section 4.6).

The efficiency is constant for E' above 1.7 GeV (99.89%), but below this momentum, the efficiency starts to decrease mainly due to decreasing resolution of the calorimeter. This efficiency is parameterized as a function of the scattered momentum (see Figure 5.13) and this parameterization is used in the analysis.

After the experiment it was discovered that there was a problem with the calorimeter ADCs. The ADCs exhibited a shifting gain which was present throughout

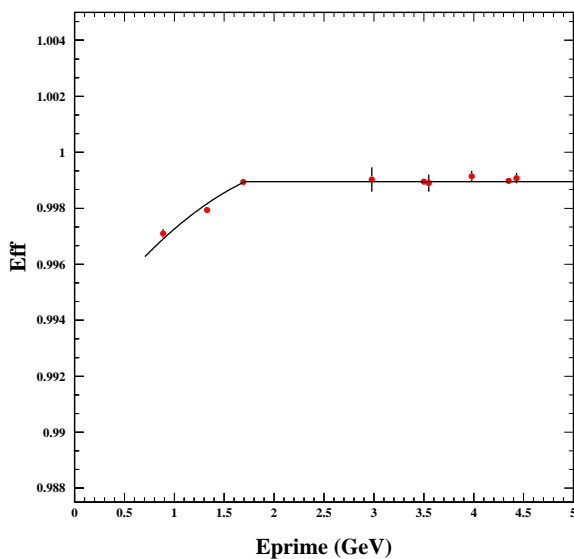


Figure 5.13 The calorimeter cut efficiency as a function of scattered momentum.

the course of the run. This causes a shift in the shower sum distribution (see Figure 5.14). A detailed account of this issue is given in the Appendix 3 of [91]. The shifting peak may cause electrons to be excluded, or pions to be included when we apply the nominal cut on the normalized shower spectrum. This shift widens the peak in the normalized shower spectrum, thus artificially increasing the calorimeter energy resolution (as given by the width of the peak). Due to the difficulty involved in correcting this shift on a run by run basis, it was decided to increase the systematic error associated with the PID cut on shower sum. Considering the global behavior of the shift, we estimate that this contributes 0.1% to the uncertainty in cut efficiency. Later it was found that the problem involved a switchable delay box, whose output was not stable (signal generating the ADC gate for the calorimeter) [95].

5.7.4 Čerenkov Cut Efficiency

In the analysis we used a cut ($hcer_npe > 1.5$) on the Čerenkov spectrum in order to distinguish electrons from pions. Figure 5.12 shows the response of the calorimeter and Čerenkov detector for a typical run. However, some fraction of the

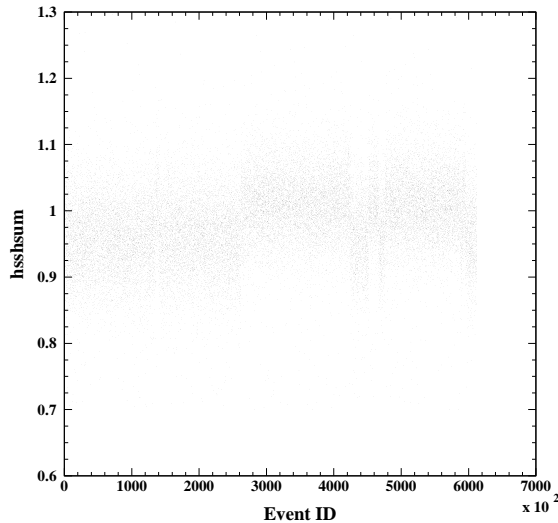


Figure 5.14 Figure shows the shift in the hsshsum peak vs event id (basically time progression) for one of the runs. This shift causes an artificial increase in the resolution of the spectrum and makes it difficult to apply a nominal PID cut on the spectrum.

electrons can be lost due to this cut and we need to account for that inefficiency. This is done with a pure sample of electrons, prepared without the use of the Čerenkov detector. For E03-103, we used elastic scattering runs to parameterize the Čerenkov efficiency by taking advantage of the constraint on invariant mass. In addition to the cuts in Table 5.3, we used the following cuts to define a pure sample of electrons. Then the Čerenkov cut efficiency for a nominal cut of 1.5 is defined as:

$$\varepsilon_{\check{C}erenkov}^{cut} = \frac{N_{(all \& hcer_{npe} > 1.5)}}{N_{(all)}}, \quad (5.24)$$

where $N_{(all)}$ is the total number of elastically scattered electrons passing cuts $abs(W - 0.938272) < 0.05$, $hsshsum > 0.8$ and $\mathbf{ELHI} > 100$. Putting a constraint on the \mathbf{ELHI} trigger assures that we are not biased towards the Čerenkov component (\mathbf{ELLO}) of the trigger.

As mentioned in section 5.3.2, the sum of signals from the photo-electrons from both tubes served as the Čerenkov signal. Figure 5.15 shows the efficiency of the Čerenkov detector for a high and low momentum elastic runs. From the figure

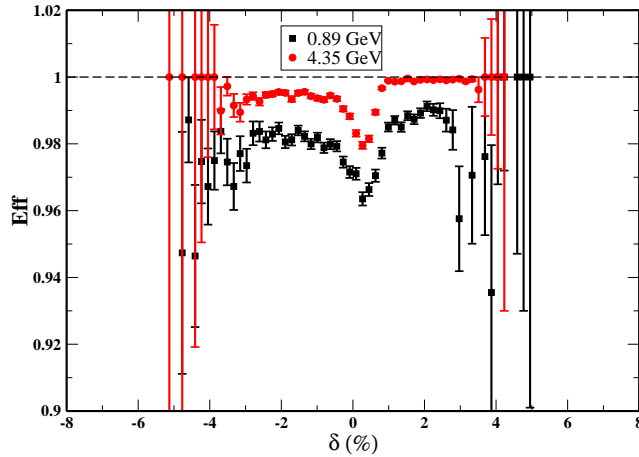


Figure 5.15 The plot shows the Čerenkov efficiency calculated for two elastic runs with different central momenta as shown in the legend. The efficiency is plotted as a function of δ . This plot shows that the response of the Čerenkov detector contains a momentum-dependent part and a δ -acceptance dependent part.

it is clear that the Čerenkov response has some position dependence. Mainly, the variation in the response near $\delta = 0$ is due to internal optical misalignments. This reduces the photo-electron yield near the central axis, which is evident from the dip in the small area in the $\delta = 0$ region in Figure 5.15. It is also clear that in addition to this δ -dependent inefficiency, the Čerenkov has a momentum-dependent inefficiency (also noted by previous experiments in the Hall C), related to variation of Čerenkov cone with particle momentum.

Extensive studies were done to parameterize the response of the Čerenkov detector. Basically, the δ acceptance was divided into three regions and a momentum dependent efficiency is parameterized for each of those regions. Since the elastic runs do not cover the full δ acceptance, we used runs with low a π/e ratio, to calculate the efficiency at the edge of acceptance. Figure 5.16 shows the calculated efficiency applied to one of the production runs with a central momentum of 2.17 GeV. It should be noted that it is extremely difficult to get a pure sample of electrons by using only the calorimeter, so the sample is pion contaminated and the parameterization slightly overestimates the data. However, the qualitative agreement with the production

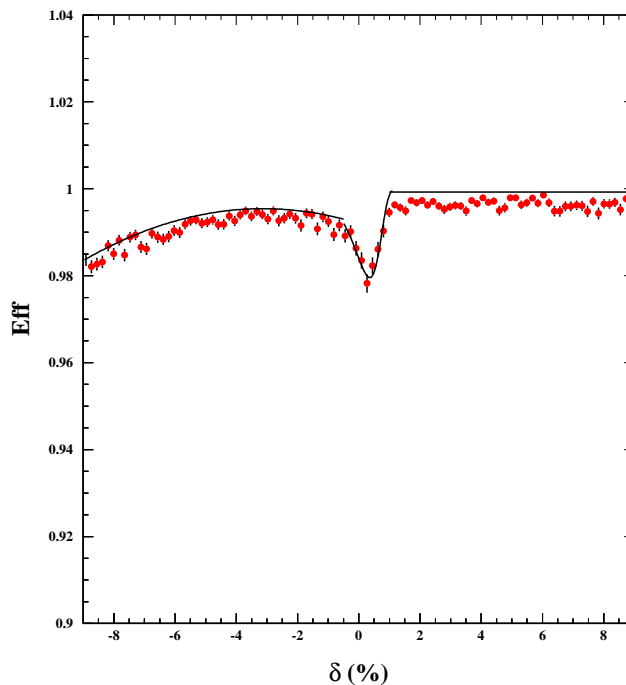


Figure 5.16 Parameterized Čerenkov efficiency (curve) applied to a production run with central momentum 2.17 GeV. This only shows the qualitative behavior (since this is a production run the data shown are pion contaminated, spoiling the quantitative agreement).

runs is fairly reasonable. During the data analysis the efficiency parameterization is applied on an event-by-event basis.

5.8 Background Processes and Estimation

In addition to the scattered electrons, there are secondary electrons that come into the acceptance of the detector due to other physical processes, and constitute a background for the measurement. This background mainly consists of scattered electrons from the cryotarget cellwall, pions that survive the nominal PID cuts and mimic scattered electrons and the secondary electrons that are produced from pair production in the target after the beam electron emits a bremsstrahlung photon, producing a π^0 . The following subsections discuss each of these processes, and how

we estimate and correct for them in the analysis.

5.8.1 Background from Target Cellwalls

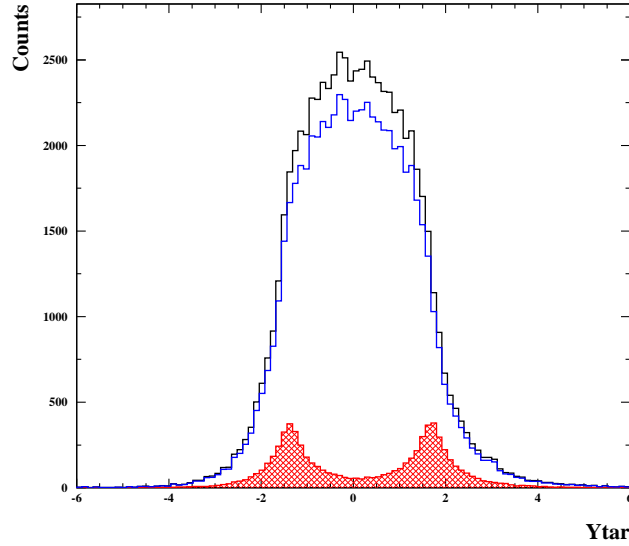


Figure 5.17 A representative y_{tar} distribution showing the dummy subtraction procedure. The count distribution shown is the events along the length perpendicular to the beam direction that pass all the nominal analysis cuts. The black (top) histogram shows the distribution in a ^4He run taken at 50 degrees. Shaded region represents the dummy contribution to the total integrated yield for this kinematics, and the dummy subtracted yield is shown by the blue histogram. Here, the cellwall contribution is $\sim 10\%$ of the total integrated yield.

Since the cryogenic targets were stored in an aluminum cell, electrons scattered from the cellwalls also contribute to the total number of detected events. This contribution has to be estimated and subtracted from the total detected events. Figure 5.17 illustrates the background subtraction procedure. The cryo-cells were made of Al 7075 which has a density of 2.7952 g/cm^3 and the thickness of the cellwalls was $\sim 0.12 \text{ mm}$ [96]. The electrons traverse two cellwalls, and since the cryo target thickness varies between 0.2 to 0.6 g/cm^2 , the typical size of the background contribution is between 10% to 20% .

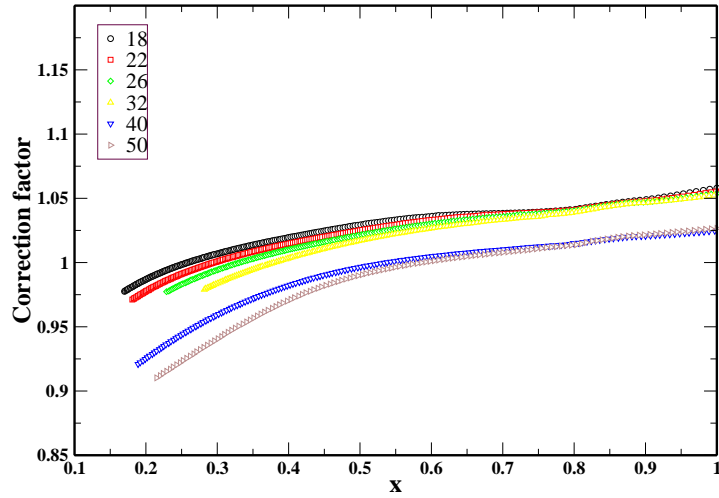


Figure 5.18 The correction due to external radiative effects for the dummy targets relative to the target cell. This arises because of the difference in geometry between the cellwall and the dummy targets. Different colors and symbols represent different angles (in degrees) as shown in the legend.

For E03-103, we used a dummy aluminum target to directly measure the cellwall contribution to the total yield. The dummy target consists of two Al foils (Al 6061- T6) separated by ~ 4 cm and with a total thickness of $(0.5259 \pm 0.0004 \text{ g/cm}^2)$. These dummy targets are ~ 8 times thicker than the cryo cellwalls (Table 5.2 gives the dummy to cellwall thickness ratios), thus allowing a higher luminosity and a smaller data acquisition time. During the experiment dummy data were taken at the same kinematics as the cryotarget data. Dummy data are treated in the same way as cryotarget data and the normalized dummy yield (after CSB subtraction, see section 5.8.3) is subtracted from the cryotarget yield (see also Eqn. 5.11) on a bin by bin basis.

$$Y = Y_e - \left[\frac{R_{\text{dummy}}^{\text{ext}}}{R_{\text{walls}}^{\text{ext}}} \frac{T_{\text{walls}}}{T_{\text{dummy}}} \right] \times Y_{\text{ed}}, \quad (5.25)$$

where T_{walls} and T_{dummy} is the thicknesses of the cellwalls and the dummy respectively, and the ratio of $R_{\text{dummy}}^{\text{ext}}$ and $R_{\text{walls}}^{\text{ext}}$ represents a correction factor which is applied to the external radiative corrections of the dummy yields. This correction factor is due to the difference in geometry between dummy and cellwalls. Since the electrons travel through different amounts of “extra” material (*i.e.* in the case of cryogenic

targets and dummy yields) the external radiative corrections will be different. This correction factor was calculated using the model cross section used for the radiative corrections and is shown in Figure 5.18.

Target	Loops	T_{dummy}/T_{walls}
^1H	2	7.757 ± 0.167
^2H	3	7.815 ± 0.231
^3He	2	7.757 ± 0.167
^4He	1	7.079 ± 0.228
^1H	1	7.079 ± 0.228
^2H	2	7.757 ± 0.167

Table 5.2 Shown are the loop numbers and the dummy to cellwall thickness ratios for the targets used in E03-103. The two rows in the bottom contain information about the summer running period. This ratio should be divided by 1.026 to account for the change in effective thickness due to the beam offset [92].

The dummy to cellwall ratio is calculated using reference [96]. The measured dummy and the cellwall thicknesses were calculated as an average of measurements at different points, thus allowing for the effects from the non-uniformity of cellwalls. It should be noted that the points closest to the beam intersection were counted twice in the averaging, to bias the average to the likely position closest to the beam-on target spot [92]. The final dummy to cellwall thickness ratio is shown in Table 5.2. For E03-103, the beam was offset ~ 4.6 mm from the cell center (see Appendix A). This means that the beam will traverse through a more curved cellwall than it should. This is estimated to change the effective cellwall thickness by 2.64%. This means that the T_{dummy}/T_{walls} ratios in Table 5.2 should be scaled by $1/1.0264$ when performing the dummy subtraction.

5.8.2 Pion Contamination

For E03-103, we used two PID cuts as mentioned in Table 5.1. However, even after this nominal cut, some pions can remain in the electron sample. Since this background cannot be removed by the nominal PID cuts, it is important to estimate the size of the background. Pion rejection rates of Čerenkov and calorimeter detectors

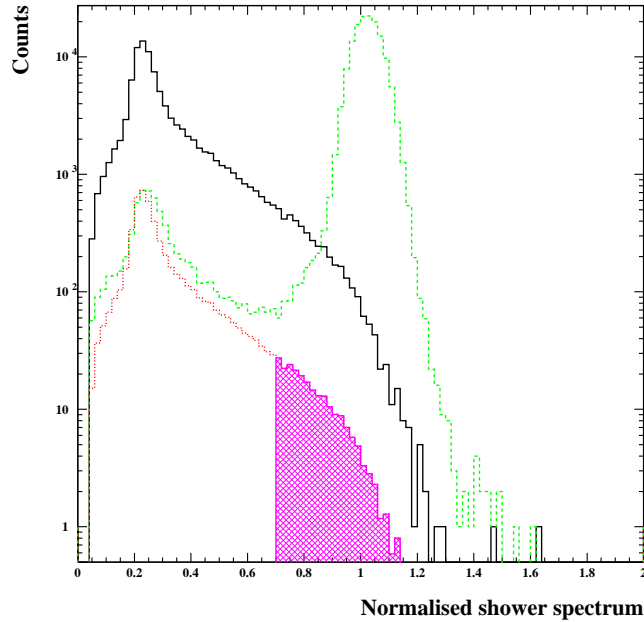


Figure 5.19 The calorimeter distribution showing the pion background estimation procedure. Here, the green dashed lines represents the electron sample and includes some pion background. The pion background is estimated by matching the background to spectrum of a pure pion sample (denoted by black solid curve). This pure pion sample is normalized to match the height of the electron+pion spectrum, and the resulting spectrum is denoted by the red dotted curve. Hatched area represents the total number of pions that pass the nominal PID cuts, and constitutes the pion contamination.

are always greater than 500:1 and 100:1 respectively. However, some pions can fire the Čerenkov detector by producing knock-on electrons in the aluminum entrance window. These knock-on electrons are of high enough energy to emit Čerenkov light and will pass the nominal Čerenkov cut. As mentioned earlier, pions in the calorimeter give a signal corresponding to their energy loss which is on average $0.3 \text{ GeV}/E'$. However, through a charge exchange reaction they can produce neutral pions, which decay into two photons. Thus, the full energy of a π^0 can be deposited in the calorimeter, and this will show up as a high energy tail in the calorimeter spectrum that extends well beyond the nominal cut at $\text{shsum} = 0.7$.

The following method was used to estimate the pion background. The idea

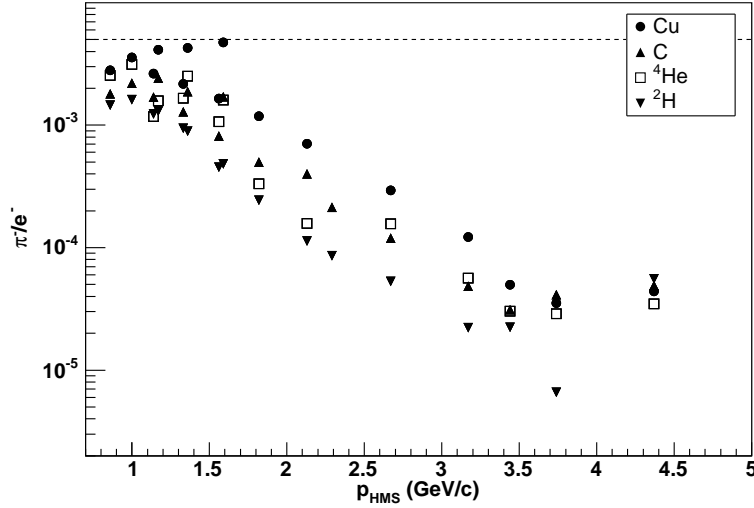


Figure 5.20 Ratio of pions to the sum of pions and electrons as a function of momentum. Only data for $x < 0.9$ are shown [91].

is to generate a clean pion sample. Then the shape of the calorimeter spectrum from this sample matches the residual pion background in the electron spectrum. First a calorimeter spectrum is created using the usual acceptance cuts, $hcer_npe > 1.5$ and using the standard trigger as in the data analysis. Then a clean sample of pions is prepared with the usual acceptance cuts, $hcer_npe < 0.5$ using an unbiased trigger sample. Then a normalization factor is calculated as the ratio of the number of events in the bin (containing highest count) around the pion peak in the calorimeter distribution for the above mentioned spectra. The next step is to scale the pion sample using the normalization factor so that it matches the pion background in the electron spectrum. Then the number of events passing the $shsum > 0.7$ in the normalized pion spectrum represents the pion contamination. For this study, events were selected from trigger types that did not require calorimeter information. The resulting spectrum is shown in Figure 5.19 and the shaded region represents the pions that pass the nominal PID cuts.

Figure 5.20 shows the pion contamination as a function of the HMS momentum. This figure shows the ratio of pions to the sum of pions and electrons. In the

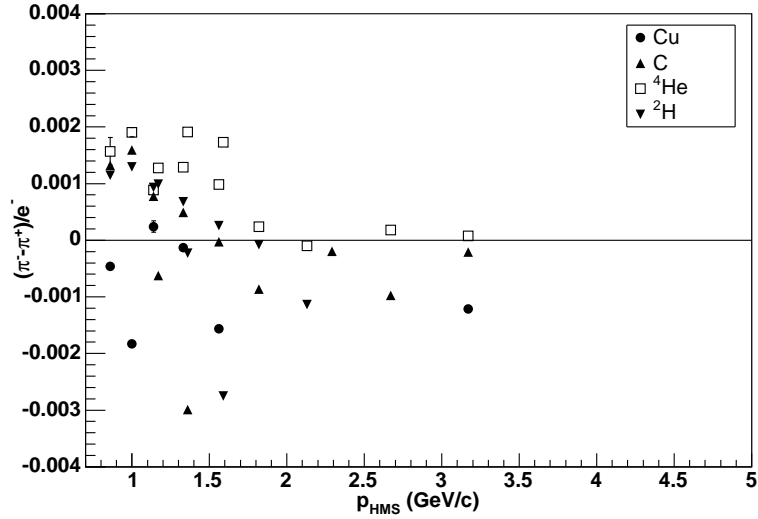


Figure 5.21 The relative difference in the normalized yields of π^+ and π^- as function of E' [91]. Since the difference is very small we make no explicit correction for pion contamination in the analysis.

worst possible case the pion contamination is 0.5%. However, it should be noted that there is also a pion background in the positive polarity data. If the cross sections for π^+ and π^- production are the same, then the number of pions in the negative polarity runs will cancel the number of pions in the positive polarity runs once we apply the charge symmetric background correction (see section 5.8.3). Figure 5.21 shows this relative difference in the yield of charged pions. The net pion contamination is at most 0.3% after the subtraction of the charge symmetric background. We assume a full pion subtraction for the cross section, and make no explicit correction for pion contamination. However, we assign a 0.2% point-to-point uncertainty to account for the relative difference in the number of negative and positive pions remaining in the sample even after charge symmetric background subtraction.

5.8.3 Charge Symmetric Background

In certain kinematic regions, there is a significant probability that the incident electron can interact with the target nuclei and produce neutral pions in the

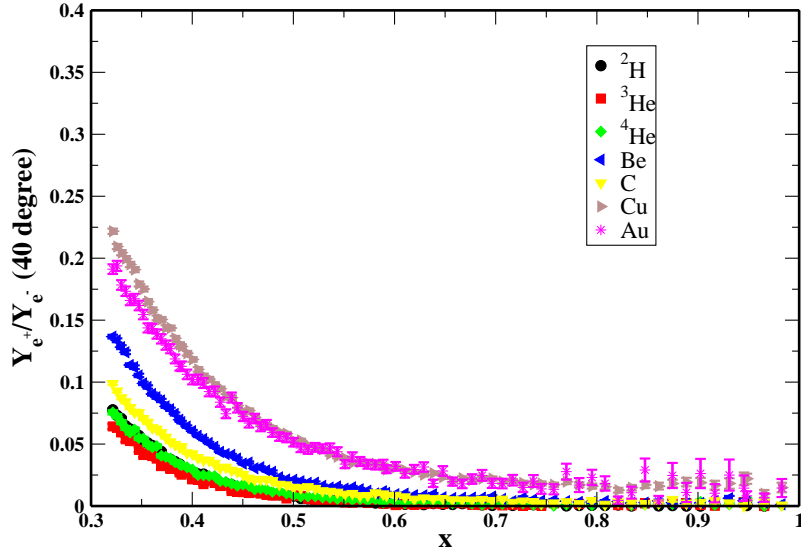


Figure 5.22 The charge symmetric background as a function of x for 40 degree data. Targets with relatively high radiation length have a significant background at low x values.

target. These pions can decay into high energy photons, which can produce an equal number of positrons and electrons. The Bethe-Heitler process (interaction of photon and virtual photon) can also contribute to the charge symmetric background (CSB), but the dominant contribution is from π^0 decay.

The total number of electrons detected in the spectrometer is $e_{detected}^- = e_{primary}^- + e_{background}^-$. Since an equal number of positrons and electrons are produced, the yield is charge symmetric. This allows us to estimate the number of secondary background electrons by running the spectrometer with positive polarity, and detecting the positrons.

During E03-103, we used the HMS to take positron data for each target, and at the kinematics setting where the CSB was large (larger scattering angles). This allowed a direct measurement of the CSB. Since the background is charge symmetric, we can set $e_{detected}^+ = e_{background}^-$. During the analysis, positron data are subjected to the same cuts as electron data. Due to the hadrons produced (especially π^+), the total rate in the detector is higher for positron runs than that for electron runs. So we

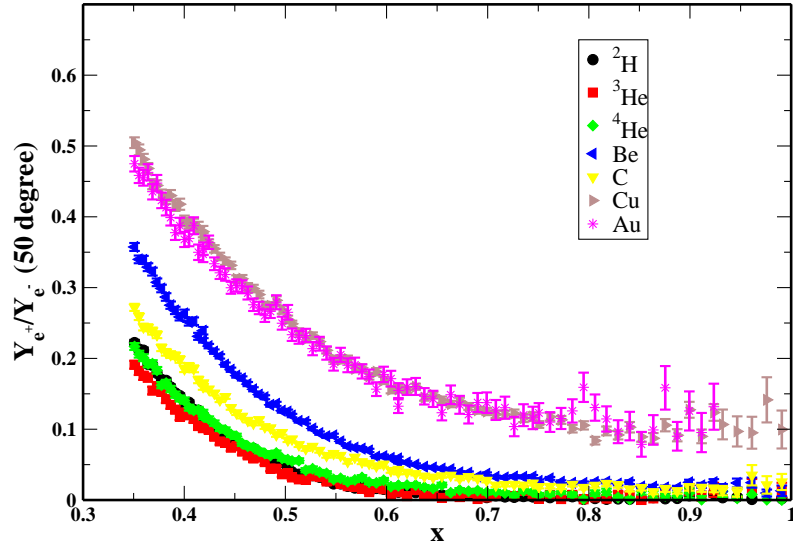


Figure 5.23 The charge symmetric background as a function of x for 50 degree data. Targets with relatively high radiation length have a significant background at low x values. For heavy nuclei and at low x , the magnitude of the background is the same as the magnitude of the signal.

used **ELCLEAN** (rather than the standard electron trigger, **ELREAL**, see section 5.6.2) for positron data acquisition. We formed a luminosity normalized yield of the positron data which was subtracted from the luminosity normalized electron yield as mentioned in section 5.5.

The yield ratio is

$$R_{\text{csb}} = \frac{Y_{(e^+, \text{elclean})}}{Y_{(e^-, \text{elclean})}}, \quad (5.26)$$

where $Y_{(e^-, \text{elclean})}$, contains the total yield from primary scattered electrons and the background. R_{csb} as a function of x for two different angles is shown in Figure 5.22 and Figure 5.23. The probability to produce neutral pions is large at larger scattering angles, and increases with decreasing scattered electron energy. At lower momentum settings, the energy transfer is high, and, thus, secondary electrons are energetic enough to bend into the spectrometer. Thus for heavy nuclei, and at 50 degrees $R_{\text{csb}} \sim 50\%$, implying that the primary electron and background electron signals are of the same magnitude at these kinematics. Thus, CSB is quite large at low x but

for the majority of the data and at high x , CSB is very small.

5.9 Target Boiling Corrections

When the electron beam passes through the target material, it deposits energy in the form of heat. This causes local boiling along the path of the beam, and temperature fluctuations affect the target density. For solid targets this is not a problem, but for cryotargets the density variation will affect the yield. The boiling effects depend on the beam current, beam rastering size and the thermal properties of targets. To understand the dependence of the yield on the current, dedicated runs (luminosity scans) were taken, in which data were taken at different beam currents for carbon and the four cryotargets used in the experiment. What follows is a brief description of the method. More information about the target boiling studies for E03-103 can be found in [91].

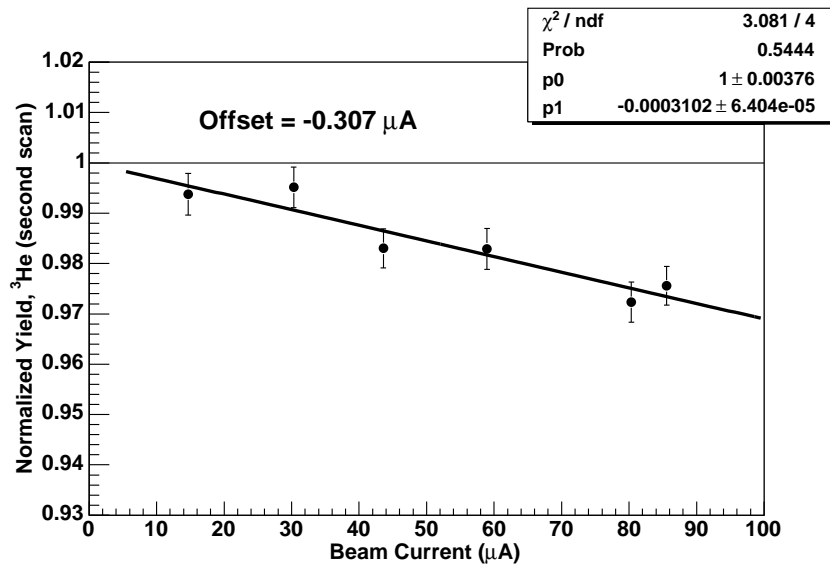


Figure 5.24 The charge normalized yield plotted against current for the ³He target. This yield is corrected for the offsets found from the carbon scan. The residual slope is due to target density fluctuations [91].

A luminosity scan consists of a set of runs taken by varying the beam current

and keeping everything else the same (target, kinematics ...). Then one forms the charge normalized yield for each run (see section 5.5). Possible variation of this charge normalized yield with the beam current is due to the local boiling of the cryogen. Solid targets should not be affected by the currents used in the experiment. However, a drop in yield was observed for the carbon target. It was found that a shift in the offset in the BCMs, consistent with the uncertainty in the BCM calibration procedure can cause such effects.

The particle yield is given by

$$Y_{measured} = \frac{N}{Q} = \frac{N}{I\Delta t}, \quad (5.27)$$

where I is the beam current from the BCM calibration. If there is an offset, ΔI , in the measured beam current then the correct yield will be

$$Y_{corrected} = \frac{Y_{measured}}{1 + \frac{\Delta I}{I}}. \quad (5.28)$$

The carbon data was fit to this functional form, and the offset was found to be $-0.307 \mu A$ which is comparable with the magnitude of the scatter seen in the BCM calibrations (see Figure 5.5). The data are corrected using the offsets calculated from the carbon scan to find the cryotarget slope versus current.

Luminosity scan results for the hydrogen and deuterium targets did not show any residual slope after correcting for the BCM offset. However, helium targets show a drop in the yield even after applying the BCM offset corrections. An example of the luminosity scan result for the ^3He target is shown in Figure 5.24. For ^3He , the measured slope was $(-3.10 \pm 0.64)\%$ at $100 \mu A$ and for ^4He $(-1.27 \pm 0.50)\%$ at $100 \mu A$. It should be noted that this slope is calculated based on the total yield (cryogen + cellwall). Estimating slope in this way is reasonable for our kinematics, since the ratio of yield from cellwall to the total yield is roughly constant as a function of x . The yield for each run is divided by a factor

$$\tau_{cor} = 1 - \text{slope} \times I_{beam-on}, \quad (5.29)$$

where $I_{beam-on}$ is the beam-on current, and τ_{cor} is the change in the areal density due to fluctuations in current.

5.10 Event Selection

$ x'_{tar} $	< 70 mrad
$ y'_{tar} $	< 20 mrad
$ \delta $	≤ 9 %

Table 5.3 Acceptance cuts used in the analysis. Here, δ is the relative deviation from the central momentum and x'_{tar} and y'_{tar} are the out-of-plane and in-plane slopes of the reconstructed tracks.

Imposing cuts on the spectrometer distributions allows us to limit the data to events where the acceptance is well known, and assures that the particle originated from the target region. Additional events come from particles that scatter into the acceptance when it hits an edge of a collimator. Since these events are not from an interaction vertex, they constitute a background. Thus, we need a geometrical cut on x'_{tar} , y'_{tar} (for a definition of these variables see section 5.2). These cuts are large enough so that effectively the collimator defines the angular acceptance. Similarly, a cut was applied to the reconstructed momentum mainly to restrain the momentum acceptance to spectrometer regions that have reliable matrix elements. Cuts used on reconstructed tracks for E03-103 analysis are shown in Table 5.3.

5.11 Acceptance Correction

An acceptance function is used to correct for the nonuniform sensitivity of the spectrometer. If the detector response is uniform, the acceptance function is naively the bin width in δ , times the geometric solid angle for a given $\Delta\theta$ bin. However, for a given setting, the spectrometer detects particles with a range of angles and momenta around the central value. As we move away from the central kinematics, some of the tracks can be lost if they hit collimators, apertures or vacuum beam pipes. Moreover, there can be effects due to finite resolution and non-perfect reconstruction of the spectrometer. These lost events must be counted when we calculate the cross section, otherwise the particle yield will be biased towards more efficient regions of the

acceptance. Thus, one needs a more reasonable function than the naive acceptance function mentioned above.

The acceptance of the spectrometer is defined to be the probability that the spectrometer will accept an event originating from a point in the target $(X_{\text{tar}}, Y_{\text{tar}}, Z_{\text{tar}})$ with kinematical properties described by three spectrometer coordinates (δ, X', Y') . In general, the acceptance is a function of the six variables $(\delta, X', Y', X_{\text{tar}}, Y_{\text{tar}}, Z_{\text{tar}})$ that fully define the event, and the measured yield for a given process is an integral of the acceptance function over this six-dimensional phase space, weighted by the differential cross section for that process. Due to the large amount of computer processing time required, it is not feasible to generate enough statistics in all six variables of a full simulation. In most cases, the target material is thin enough so that the energy loss and multiple scattering is negligible, allowing us to integrate over the target position variables. In addition, it has been shown that an acceptance function binned in two dimensions $(\delta, \Delta\theta)$ yields equivalent results as one binned explicitly in in-plane (Y') and out-of-plane (X') coordinates [92]. The acceptance function, $A(\delta, \Delta\theta)$, has been calculated using a Monte Carlo simulation of the spectrometer. A representative distribution is shown in Figure 5.25.

The Monte Carlo consists mainly of three parts: the event generator, transport of the particle through the magnets, and a list of different materials and apertures that stops the particle from being detected. Each event is randomly generated in the target coordinates, while the quantities $(\delta, \Delta Y', \Delta X')$ are randomly chosen within their allowed limits. Then the particles are projected forward and transported to the detector hut using the COSY INFINITY program [88], which models magnetic transport properties of the spectrometer. Events that pass through the walls of the magnets or fail to pass through the different apertures defined in the model are rejected. If the particle successfully traverses the spectrometer and passes all the criteria in the detector, then it is accepted. The acceptance in the $(ij)^{\text{th}}$ phase space bin is defined as,

$$A(\delta^i, \Delta\theta^j) = \frac{N_{\text{det}}(\delta^i, \Delta\theta^j)}{N_{\text{gen}}(\delta^i, \Delta\theta^j)} \Delta V_{\text{gen}}, \quad (5.30)$$

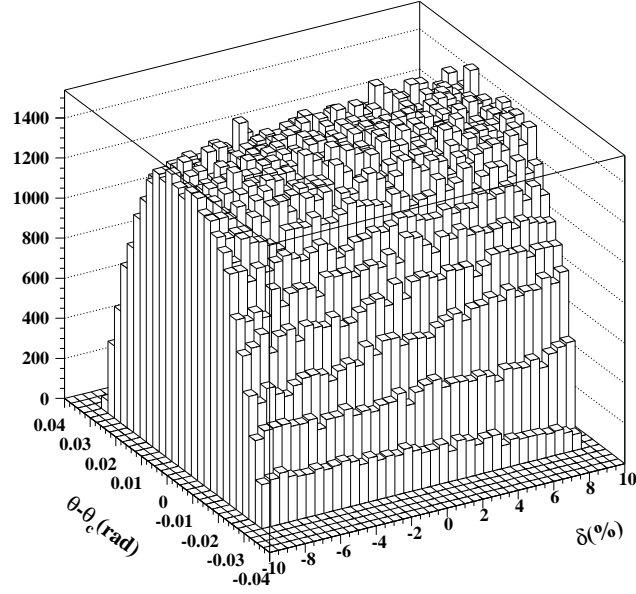


Figure 5.25 The acceptance distribution of the HMS for one of the settings calculated using a single arm Monte Carlo.

where N_{det} is the number of events detected and N_{gen} is the number of events generated in a volume of ΔV_{gen} in which the events are thrown. The spectrometer acceptance is calculated with the same cuts used for analysis, and is binned into small bins in δ and $\Delta\theta$.

For the data analysis, a relative acceptance was applied on an event-by-event basis. The relative acceptance with respect to central angle θ_c , for the k^{th} event is defined as,

$$A_{\text{rel}}^k = \frac{A(\delta^k, \theta_c)}{A(\delta^k, \Delta\theta^k)}. \quad (5.31)$$

Then the weight that an event is accepted in a given δ bin, normalized by the total solid angle for that δ bin, is given by

$$A_{\text{weight}}^k = \left[\frac{A_{\text{rel}}^k}{A(\delta^k, \theta_c)} \right] \frac{1}{N_{\text{tbin}}}. \quad (5.32)$$

Here, N_{tbin} is the total number of the $\Delta\theta$ bins in that one dimensional δ bin. Each event was multiplied with this acceptance weight, and then the event

was binned in a one dimensional δ bin. It should be noted that the θ bin-centering corrections are also applied on an event-by-event basis (see section 5.12.1).

It is known from previous experiments that there is a small imperfection in optics model, which can be corrected for using a δ -dependent correction to the acceptance function (for more information see [86]). It was found that this effect is independent of the kinematics (E, E', θ) and targets. This correction was parameterized as a function of δ , and this correction factor was divided out of the data on an event-by-event basis.

5.12 Cross Section Extraction

In order to get the Born cross section at fixed angle as a function of E' , the data needs to be corrected for radiative processes and bin-centering. The following sections briefly discuss how these corrections are applied for the E03-103 analysis.

5.12.1 Bin Centering Corrections

The main goal of the analysis is to obtain the inclusive differential electro-production cross section for a range of E' at a fixed scattering angle, and, hence, to obtain the target cross section ratios. The HMS accepts events in a range of theta ($\theta_c \pm 1.8$ degrees). A linear variation of the cross section over a symmetric θ acceptance does not result in bin centering corrections. However, for E03-103, the cross section can vary rapidly with θ (especially in the resonance region). In order to measure the cross section at fixed values of E' and θ , we must bin the data and make a correction to convert from binned counts to the value of the cross section at the center of the bin using the bin centering procedure. The bin centering correction depends on the model cross section used (the cross section model is discussed in section 5.13), and the model dependence in this correction can be a large systematic uncertainty in the analysis. We apply the correction by rescaling each event by the ratio of its cross section to the central cross section. The bin centering factor (BC)

for an event with scattered momentum E'_i and angle θ_i is:

$$\text{BC} = \frac{\sigma_{\text{rad}}^{\text{model}}(\mathbf{E}, \mathbf{E}'_c, \theta_c)}{\sigma_{\text{rad}}^{\text{model}}(\mathbf{E}, \mathbf{E}'_i, \theta_i)}, \quad (5.33)$$

where $\sigma_{\text{rad}}^{\text{model}}(\mathbf{E}, \mathbf{E}'_c, \theta_c)$ and $\sigma_{\text{rad}}^{\text{model}}(\mathbf{E}, \mathbf{E}'_i, \theta_i)$ are the radiated model cross sections calculated at $(\mathbf{E}'_c, \theta_c)$ and $(\mathbf{E}'_i, \theta_i)$ respectively. Here, \mathbf{E}'_c represents the center of the momentum bin and θ_c represents the central angle of the spectrometer. Then the bin centered radiated experimental cross section, $\sigma_{\text{rad}}^{\text{exp}}(\mathbf{E}, \mathbf{E}'_c, \theta_c)$ is given by:

$$\sigma_{\text{rad}}^{\text{exp}}(\mathbf{E}, \mathbf{E}'_c, \theta_c) = \sigma_{\text{rad}}^{\text{exp}}(\mathbf{E}, \mathbf{E}'_i, \theta_i) \times \text{BC}. \quad (5.34)$$

Bin centering corrections were applied on an event-by-event basis. Since we did a relative acceptance correction (with respect to θ_c), after this bin centering procedure the resulting cross section represents the radiated experimental cross section bin centered in momentum at fixed scattering angle.

5.12.2 Radiative Corrections

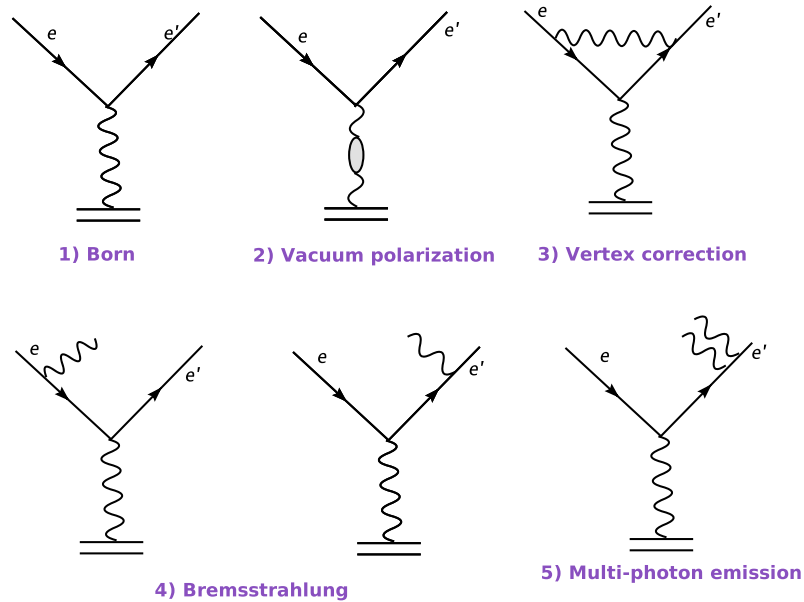


Figure 5.26 Lowest order Feynman diagrams for inclusive lepton-nucleon scattering.

Cross sections measured in deep inelastic scattering can have large contributions from processes other than the Born diagram (see Figure 5.26). The theoretical interpretation of cross sections often assumes that the interactions can be explained in the one photon exchange (Born) approximation. However, there are higher order Feynman diagrams in α that also contribute to the measured cross sections. In order to determine the differential cross section for the one photon exchange process, all the other contributions from the higher order processes in α have to be estimated and corrected in the measured cross section.

Radiative effects in electron scattering can be divided into two categories: internal and external. For the external corrections, the incoming or outgoing electron radiates a real photon due to interactions with the fields of nuclei other than the target. This process depends on the target thickness. Among the external processes are external bremsstrahlung and ionization energy losses. Internal effects occur at scattering vertex, and are calculable in QED. Internal effects include soft processes (or first order processes) like internal bremsstrahlung, but internal effects also include the hard processes like vacuum polarization, vertex correction and multiple photon exchange. All the processes described above will modify the energy of the particle from that at the scattering vertex. A thorough treatment of radiative corrections can be found in [97, 98].

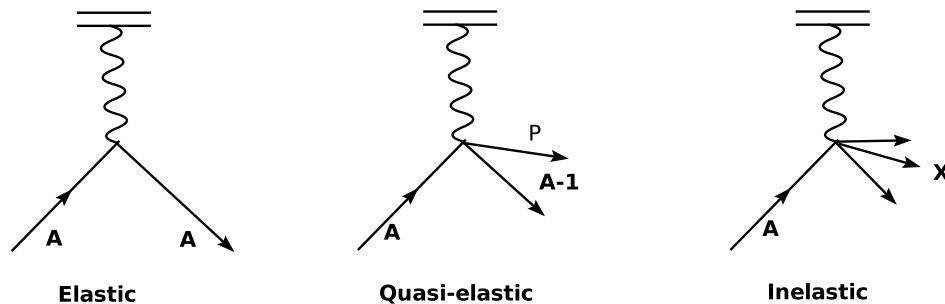


Figure 5.27 Different processes that can contribute to the measured cross sections.

The program used to compute the radiative corrections for this analysis was developed at SLAC and is described in detail in [99]. Processes that contribute to

the measured cross sections for a nuclear target are shown in Figure 5.27. The total radiated cross section can be expressed as,

$$\sigma_{\text{measured}} = \sigma_{\text{inelastic}}^{\text{radiated}} + \sigma_{\text{quasielastic}}^{\text{radiated}} + \sigma_{\text{elastic}}^{\text{radiated}}. \quad (5.35)$$

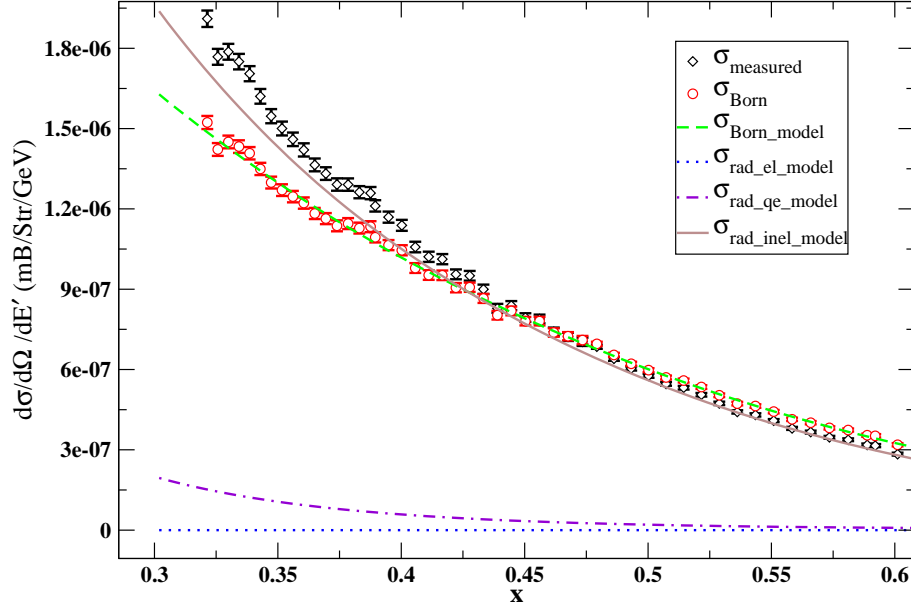


Figure 5.28 Measured (black diamonds) and extracted Born cross section (red circles) for Au at 40 degrees. Different contributions to the measured cross sections are also shown (dotted line represents the elastic tail, dash dotted line represents the quasi-elastic tail, solid line represents the inelastic contribution and the dashed line represents the total Born model). At low x , the quasi-elastic tail contributes significantly to the total radiated model. For heavy nuclei and at low x , the effect of this contribution is the dominant uncertainty in the radiative corrections.

Since the inelastic radiative cross section is largely proportional to the Born cross section for our kinematics ($> 80\%$), we used the multiplicative radiative correction method. For the kinematics of this analysis, the nuclear elastic tail contributes less than 0.1% to the total cross section for ^2H , and even less for heavy nuclei. Figure 5.28 shows the 40 degrees, Au cross sections before and after the application of radiative corrections. Contributions from various radiative processes to the measured cross sections are also shown in the same figure.

The radiative correction factor RC can be expressed as,

$$RC = \frac{\sigma_{Born}^{model}}{\sigma_{radiated}^{model}}, \quad (5.36)$$

where σ_{Born}^{model} is the model cross section due to the exchange of a single photon and

$$\sigma_{radiated}^{model} = external \otimes internal \otimes Born, \quad (5.37)$$

is the model cross section due to the sum of all higher-order diagrams. The convolution involves integrating over the “internal” and “external” bremsstrahlung photon momenta and angles, and the target dimensions.

For E03-103, the external corrections are computed using a complete calculation of Mo-Tsai [97] with a few approximations. This approach, “MTEQUI”, uses the equivalent radiator approximation [99]. In the equivalent radiator method, the effect of “internal” Bremsstrahlung is calculated using two hypothetical radiators of equal radiation length, one placed before and one after the scattering. Note that, in particular, the energy-peaking approximation is not used for the computation of external contributions. The internal contribution in “MTEQUI” method is evaluated by setting the radiation length of the material before and after the scattering point to zero, and ignoring the target length integral (see Eqn. C1 in [99]). Then the radiated model cross section is given by:

$$\sigma_{radiated}^{model} = \sigma_{MTEQUI}^{(i+e) radiated model}. \quad (5.38)$$

To obtain $\sigma_{radiated}^{model}$, one needs to know the cross sections over the entire kinematic range (from elastic threshold up to the kinematic point being calculated, see Figure C.1 in reference [99]). The Born model cross section used for this analysis is discussed in section 5.13. The radiative correction factor, RC, was multiplied with measured cross sections on an event-by-event basis to get the corrected cross sections. The effect of radiative correction varied from a few percent to 40%, depending on the kinematics and targets. Figure 5.29 shows the radiative correction factor (RC) for the 40 degree data for different targets used in this analysis.

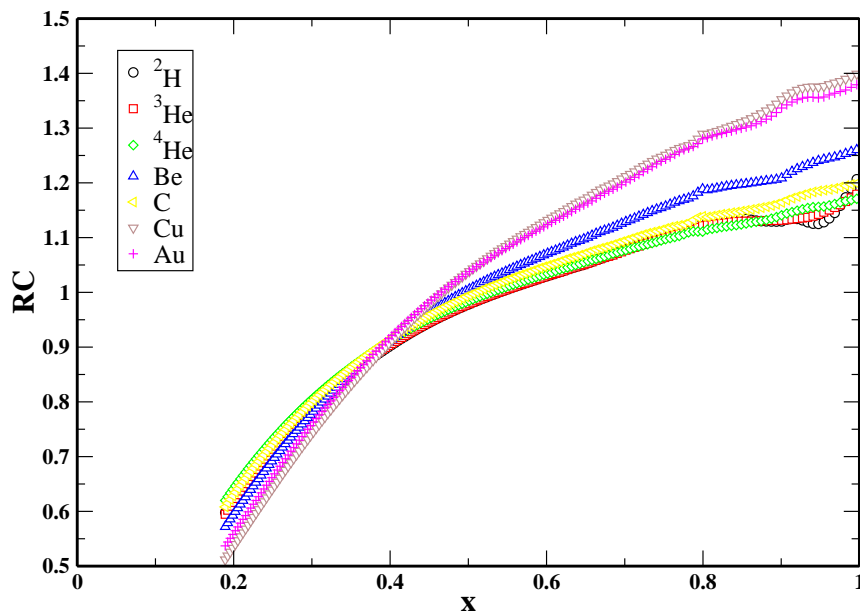


Figure 5.29 Radiative correction (RC) factor applied to 40 degree data for different targets used in this analysis.

5.12.3 Coulomb Corrections

This correction is due to the acceleration of the incoming electrons and deceleration of outgoing electrons in the Coulomb field of the target nucleus. This Coulomb distortion causes an increase in the momentum of incoming beam electron (E) and a decrease in the momentum of the scattered electron (E') relative to the vertex values. This change in the kinematics can have a significant effect on the measured cross sections. Thus, the plane wave Born approximation is no longer valid for the calculation of scattering cross sections in the strong and long-range electrostatic field of highly charged nuclei, and a correction should be applied to the measured asymptotic values of E and E' . For E03-103, we used an improved version of the Effective Momentum Approximation (EMA) as described in [100].

The charge of the nucleus has two effects on the electron wave function. The initial and final state electron momenta ($\vec{k}_{i,f}$) are modified in the vicinity of the nucleus due to the attractive electrostatic potential. Secondly, the attractive

Target	R_0 (fm)	ΔE (MeV)
^3He	1.80	0.85
^4He	1.68	1.0
Be	2.70	1.88
C	2.89	2.92
Cu	4.59	10.2
Au	6.55	19.9

Table 5.4 Table shows the average effective potential ΔE and the values of RMS charge radii for the different targets used in the analysis. Note that, the radii for helium are measured values, while the rest of the radii are calculated using Eqn. 5.41.

potential leads to focussing of the electron wave function in the interaction region. The distorted electron wave can be approximated by [101, 102],

$$\psi_{\vec{k}_{i,f}} = \frac{|(\vec{k}_{i,f})_{eff}|}{|\vec{k}_{i,f}|} \psi_{(0)} \exp\left(i \vec{k}_{i,f} \cdot \vec{r}\right), \quad (5.39)$$

where $\psi_{(0)}$ is the Dirac-spinor with $|(\vec{k}_{i,f})_{eff}| = |(\vec{k}_{i,f})| - \bar{V}$, and \bar{V} is the average electrostatic potential of the nucleus. The change in potential for a highly relativistic electron approaching from infinity along the z axis towards the nuclear center (with charge Ze , radius R_0 , and for $z < R_0$) of a spherical charge distribution is given by:

$$\Delta V_{(z)} = V_{(\infty)} - V_{(z)} = -\frac{Z\alpha}{2R_0} \left(3 - \frac{z^2}{R_0^2}\right) \quad (5.40)$$

with $V_{(\infty)}$ defined as zero, and z is measured from the center of the sphere. The RMS charge radii of a nucleus with mass number A are calculated using the relation given in [102],

$$R_0(A) = 1.1 A^{1/3} + 0.86 A^{-1/3}. \quad (5.41)$$

If the scattering happens at the center of the nucleus, then the change in the potential becomes

$$\Delta V_{(0)} = \frac{3Z\alpha}{2R_0}. \quad (5.42)$$

Note that, since one does not typically correct for Coulomb acceleration in $Z = 1$ targets, and we are comparing nuclei with $Z > 1$ to deuterium, we replace the factor Z with $Z - 1$ in Eqn. 5.42. Since most of the nucleons in a heavy nuclei are located

on the surface of the nucleus, taking the electrostatic potential at the center of the nucleus will be an overestimate of the Coulomb correction. This effect is incorporated in the EMA approach by an average potential $0.75 - 0.80$ times $V_{(0)}$. For E03-103, an average potential of $\Delta E = \bar{V} = 0.775 V_{(0)}$ is used.

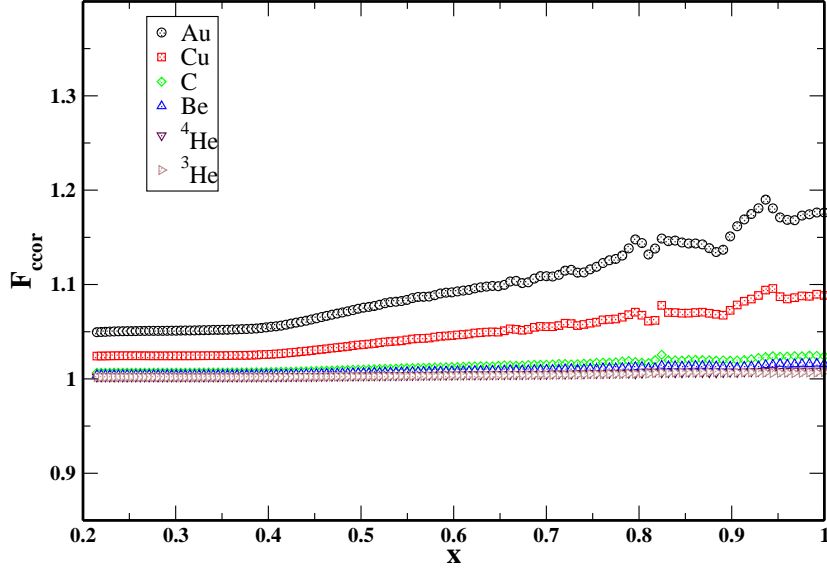


Figure 5.30 The Coulomb correction factor as a function of x , for 50 degree data and for different targets. For heavy nuclei, the Coulomb correction factor is significant, reaching a maximum of $\sim 18\%$ at very high x , near the quasi-elastic peak. For all other angles, the Coulomb correction factor is smaller than the values shown here.

In the EMA approach, the focussing factor of the incoming wave, $F_i = |(\vec{k}_i)_{eff}|/|\vec{k}_i|$, enters quadratically in the cross section calculation and produces an enhancement in cross section strength. However, the focussing factor of the outgoing wave cancels with the enhanced phase space factor in the effective cross section. The Coulomb correction factor in the EMA approach is given by the ratio of the model cross sections with nominal and shifted kinematics, scaled by the square of the focussing factor:

$$F_{cor} = \frac{\sigma_{(E,E')}}{\sigma_{(E+\Delta E, E'+\Delta E)}} \left[\frac{E}{E + \Delta E} \right]^2, \quad (5.43)$$

where σ 's are the Born model cross sections used in the radiative correction program. The measured cross sections are then multiplied by F_{cor} , to get the Coulomb-corrected cross sections.

Table 5.4 shows the values for the RMS charge radii, and the magnitude of the energy boost for the targets used in E03-103. The Coulomb correction factors as applied to the 50 degree data, are shown in Figure 5.30. These corrections are relatively small for light nuclei, but for the heavy nuclei and near the quasi-elastic peak, these corrections are significant. For Be and C, these correction are always less than 3%, and for heavy nuclei they are estimated to be $\sim 5\%$ at very small x . Though the validity of EMA calculations are verified for the inclusive quasi-elastic experiments [103], it is not clear that the same prescription can be applied for deep inelastic scattering.

5.13 Cross Section Model

A cross section model is required for the bin centering corrections, the radiative corrections and the Coulomb corrections. The Born cross section model was made up from 2 contributions: a quasi-elastic model and an inelastic model. For the quasi-elastic contribution we use a y -scaling model. The scaling variable y can be interpreted as the minimum momentum of the struck quark in the direction of the virtual photon. The scaling function, $F(y)$, is defined as the ratio of the measured nuclear cross section to the off-shell cross section for a nucleon, multiplied by a kinematic factor [104, 34, 83]:

$$F(y) = \frac{d\sigma}{d\Omega d\nu} \frac{1}{Z\sigma_p + N\sigma_N} \frac{q}{\sqrt{M^2 + (y + q)^2}}, \quad (5.44)$$

where Z is the number of protons in the nucleus, N is the number of neutrons, q is the three-momentum transfer, and M is the proton mass. The scaling function used for ${}^2\text{H}$ is from [105] and has the form:

$$F(y) = (f_0 - B) \frac{\alpha^2 e^{-(\alpha y)^2}}{\alpha^2 + y^2} + B e^{-b|y|}. \quad (5.45)$$

For heavier targets this was modified to be:

$$F(y) = (f_0 - B) \frac{\alpha^2 e^{-(ay)^2}}{\alpha^2 + y^2} + B e^{-(by)^2}, \quad (5.46)$$

where the parameters a, b, f_0, B and α are fit to the $F(y)$, extracted from the data for each target. The QE peak was fit to the data after subtracting the inelastic contribution (calculated using the inelastic part of the model) [83]. After the fit, the iterated model was used as the input for the cross section extraction, and the process was repeated until good agreement between data and the model was achieved for all settings. In addition, an angle independent global polynomial correction was used for each target to improve the agreement between data and model.

For the ${}^2\text{H}$, for the full x range, parameterizations of the proton and neutron structure functions (developed by P. Bosted and E. Christy [106]) are used. They are smeared using the momentum distribution $n(k)$, which is computed from $F(y)$.

The inelastic cross sections are computed differently for different x regions. For $x < 0.8$, the structure function is built from the ${}^2\text{H}$ model using an inelastic ‘‘EMC type’’ ratio obtained from our data. These inelastic cross sections are obtained by subtracting the quasi-elastic model from the total data cross section. Then the inelastic model was multiplied with the above ‘‘EMC type’’ ratio to get the nuclear inelastic model. The inelastic EMC ratio is iterated until good agreement between data and model is achieved. For $x > 0.9$, the smearing prescription is used with the corresponding $n(k)$ for each target. For $0.8 < x < 0.9$, an x -weighted average of the two formalisms is used.

The inelastic part of the model used for radiative correction is slightly different from the model above. The inelastic model used for bin centering has the disadvantage that, at low Q^2 , the resonances do not get smeared out enough, leaving some residual structure in the data to model ratios. It was decided to use the full smearing prescription for the full x range. For $x < 0.8$, the model is the sum of the proton and neutron structure functions smeared by the momentum distribution (determined from the derivative of $F(y)$ used in the quasi-elastic model cross section).

For $x < 0.8$, this inelastic model is then multiplied by a target-dependent polynomial function to improve the agreement between data and model. This is smoothly joined to the full smearing prescription for $x > 0.9$, using an x -weighted average for $0.8 < x < 0.9$. For the bin centering, we need the Born cross section on a two dimensional grid in θ and x (or E'), and the smearing prescription for the inelastic model cannot be used because of the significant increase in CPU time. However, once the bin centering corrections are applied, the data are centered to the central angle. Hence, the radiative correction table can be one dimensional, since the data are centered on the central angle of the setting.

The quasi-elastic peak accounts for a large portion of the total cross section, especially at the low Q^2 settings. The quasi-elastic tail has significant contribution at low x values in the radiated model, especially for heavy nuclei (see Figure 5.28). Hence, it is important to have a good quasi-elastic model. For heavy nuclei, our model cross section was compared with low Q^2 ($\geq 0.5 \text{ GeV}^2$) quasi-elastic world data, and the agreement between data and model was found to be at the 10% level near the quasi-elastic peak [83].

5.13.1 Isoscalar Corrections

EMC ratios, $R_{F_2}^A$, are expressed as the cross section ratio (per nucleon) of a target nucleus with an equal number of protons and neutrons (isoscalar nuclei) to that of deuterium. Thus, the EMC ratio for an isoscalar nuclei is just σ^A/σ^D . Since the protons and neutrons have different cross sections, the cross sections for nuclei with $Z \neq A/2$ will significantly differ from that of nuclei with $Z = A/2$. Thus, one needs a correction function to the measured F_2^A to get a symmetric nucleus:

$$\frac{1}{2}(F_2^p + F_2^n) = f_{iso}^A \frac{1}{A}(Z F_2^p + (A - Z)F_2^n). \quad (5.47)$$

This correction function only depends on F_2^n/F_2^p , the neutron to proton structure function ratios. The isoscalar function is defined as:

$$f_{iso}^A = \frac{\frac{1}{2}(1 + F_2^n/F_2^p)}{\frac{1}{A}(Z + (A - Z)F_2^n/F_2^p)}. \quad (5.48)$$

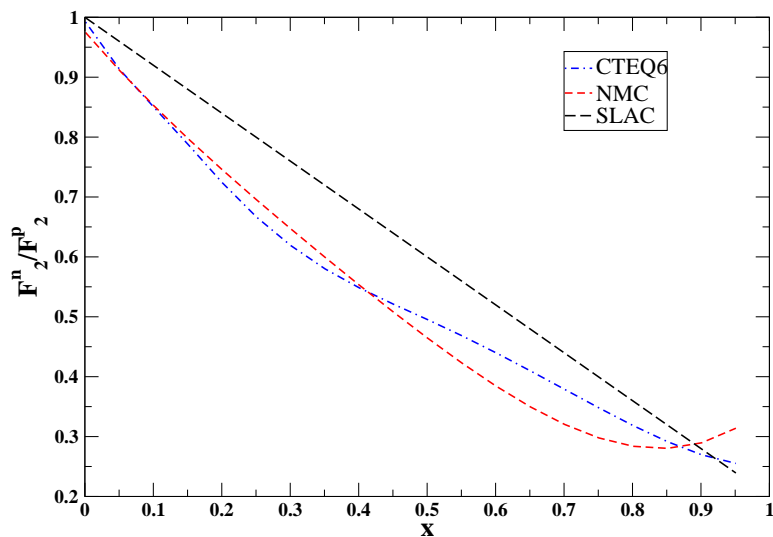


Figure 5.31 Different parameterizations for F_2^n/F_2^p .

The measured cross section ratios are multiplied by f_{iso}^A to get the isoscalar-corrected cross section ratios.

F_2^n/F_2^p has been extracted from proton and deuteron DIS measurements by SLAC [107] and NMC [108, 109]. Since there is no free neutron target, the extraction of F_2^n is always model-dependent. SLAC applied explicit Fermi motion corrections to the deuterium cross sections and extracted an unsmearred F_2^n . However, the NMC F_2^n/F_2^p ratios were extracted from the ratio of deuterium to proton cross sections, making no corrections for nuclear effects. It should be noted that both parameterizations neglect possible binding effects in deuterium. At large x , neglecting nuclear binding effects in deuterium can introduce a significant uncertainty in the F_2^n/F_2^p ratios [110].

Figure 5.31 shows different parameterizations for F_2^n/F_2^p along with F_2^n/F_2^p constructed from parton distributions from CTEQ [111] computed at $Q^2 = 10 \text{ GeV}^2$. The CTEQ fit also neglects the Fermi motion of nucleons. The results presented in this analysis are calculated using SLAC parameterization, since it more closely represents the free nucleon value. The correction factors for various parameterizations for ^3He and Au are shown in Figure 5.32.

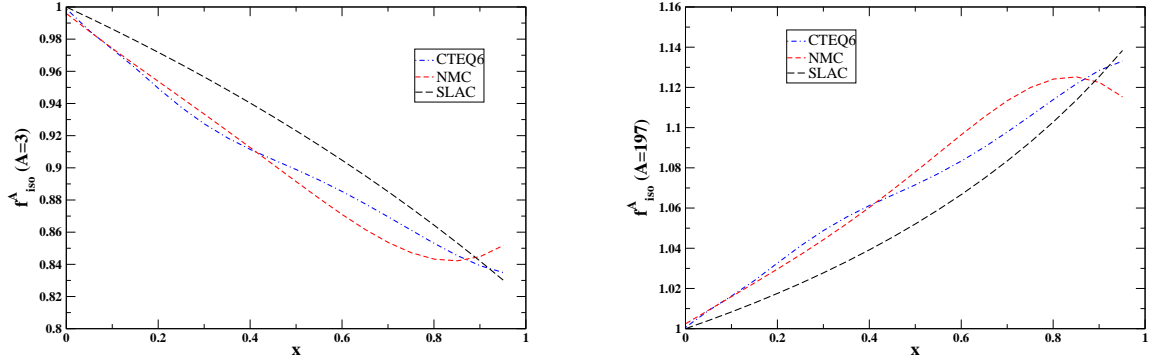


Figure 5.32 Magnitude of isoscalar corrections for ^3He and Au for the different parameterizations of F_2^n/F_2^p as discussed in the text.

5.14 Systematic Uncertainties

Statistical uncertainties come from the random variation in the various yields used to compute the cross sections. The total systematic uncertainty in the cross section extraction is taken as the sum in quadrature of all systematic uncertainties of the quantities that contribute to the cross section. The components of the systematic uncertainty can be broadly divided into two groups: point-to-point uncertainties and normalization uncertainties. Point-to-point uncertainties are due to changes in experimental conditions over the course of data acquisition, and so their effect is uncorrelated between different data points. These include uncertainties arising from a variation in the efficiencies between runs, a change in the spectrometer from one setting to another, etc. Normalization (scale) uncertainties affect the measurement globally (e.g., target thickness). Sometimes the uncertainty in a given quantity can be a mixture of point-to-point and normalization uncertainties (e.g., radiative corrections). There is an overall 2% uncertainty in the radiative corrections for the cross section calculation, and part of this comes from the methodology, while the rest comes from the model dependence). The resulting overall uncertainty in the cross section ratios is less than the total uncertainty in the cross section itself, because several scale and point-to-point type errors cancel in the ratios. Some of these uncertainties have been discussed in the relevant sections. Table 5.5 summarizes the systematic uncertainties.

Source	Absolute Uncertainty	Relative Uncertainty	$\delta\sigma/\sigma$ (%)	$\delta R/R$ (%) pt-to-pt Helium	$\delta R/R$ (%) scale Helium	$\delta R/R$ (%) pt-to-pt Solid	$\delta R/R$ (%) scale Solid
HMS Momentum	0.05%	0.01%	0.1-0.6	0.0-0.1	-	0.0-0.1	-
Beam Energy	0.05%	0.02%	0.2	0.1	-	0.1	-
θ	0.5 mr	0.2 mr	0.5	0.5	-	0.5	-
τ_D	1.4%	-	1.4	-	0.8	-	1.4
$\tau_{^3\text{He}}$	2.4%	-	2.4	0.1	2.1	-	-
$\tau_{^4\text{He}}$	1.9%	-	1.9	0.1	1.5	-	-
$\tau_{\text{C,Be}}$	0.5%	0.1%	0.5	-	-	-	0.5
τ_{Cu}	1.0%	0.1%	1.0	-	-	-	1.0
τ_{Au}	2.0%	0.2%	2.0	-	-	-	2.0
Charge	0.5%	0.25%	0.5	0.3	-	0.3	-
Target Boiling	0.6	-	0.5	0.3	0.6	-	0.5
Endcap Subtraction	<0.6%	-	0.3-0.6	-	0.1-0.3	-	0.3
Acceptance	1.0	1.0	1.4	0.3	0.2	0.3	0.5
Tracking Efficiency	0.7%	0.3%	0.7	0.3	-	0.3	-
Trigger Efficiency	-	0.05%	0.05	-	-	-	-
Electronic Dead Time	-	0.06%	0.06	-	-	-	-
Computer Dead Time	-	0.3%	0.3	0.3	-	0.3	-
Charge Symmetric BG	-	<2.5%	<2.5	<1.0	-	<2.5	-
Pion Contamination	-	0.2%	0.2	-	-	-	-
Detector Efficiency	-	0.2%	0.2	-	-	-	-
Radiative Corrections	1.0%	0.5-1.0%	1.4	0.5	0.1	0.5-1	0.5-1
Bin-centering	-	0.2%	0.2	0.1	-	0.1	-
Total	-	-	3.4-4	1.5-1.8	1.7-2.3	1.0-2.5	1.5-2.4

Table 5.5 Systematic uncertainties. The various uncertainties are shown for the different targets. For the total uncertainty, the uncertainties for each target are added in quadrature.

Kinematic uncertainties come from uncertainties in knowledge of the beam energy, spectrometer momentum, and spectrometer angle. The uncertainty associated with these quantities are determined by calculating the cross section at nominal kinematics, and comparing this to the cross section when each of the kinematic variables are shifted by the uncertainty of that variable. We use our model cross section for these studies. The resulting point-to-point systematic uncertainties are listed in Table 5.5. However, the kinematic uncertainties almost completely cancel in the cross section ratios.

The beam charge measurement is discussed in section 5.3.5. The point-to-point uncertainty was estimated to be 0.5%. This was obtained by studying the residuals of the measured currents during the calibration procedure. An additional scale uncertainty of 0.2% was assumed for the charge measured, due to the UNSER calibration. The thicknesses and the associated uncertainties of the cryogenic targets are discussed in detail in section 4.3.

The correction for cryotarget boiling was significant for the helium targets. The uncertainty associated with this correction comes from the uncertainties in the fits to the carbon and cryogenic target luminosity scan data as discussed in section 5.9. The total uncertainty in the cross section due to the boiling correction is determined to be 0.6%. Though no boiling correction is made in the case of the deuterium target, the uncertainty arising due to boiling of this target still needs to be addressed. We assign a scale uncertainty of 0.5% for the solid to deuterium target ratios.

The scale uncertainty of the acceptance correction in the HMS was estimated to be 1% from the elastic cross section studies. This is a combination of the uncertainties from the effect of position uncertainties in the target, collimator, magnets, and detector package on the acceptance correction. This also partly accounts for the uncertainty in the δ -dependent Čerenkov efficiency. The point-to-point uncertainty comes from comparison of model in the inelastic region (where the cross sections does not vary significantly) to data, and is estimated to be 1%. For the target ratios, the point-to-point uncertainty was estimated to be 0.3%. For the cryo target ratios, the scale uncertainty was estimated to be 0.2% and for solid target ratios this is estimated

to be 0.5%. This difference occurs because part of the uncertainty cancels in the cryo target ratios.

The normalization uncertainty of the tracking efficiency (see section 5.7.2) is determined to be 0.7%, mainly due to the limitations of the algorithm used for tracking. Also a point-to-point uncertainty of 0.3% is assigned to the tracking efficiency, mainly based on the spread of the points in tracking efficiency vs scintillator rate plot. Though the trigger efficiency was better than 0.992, a scale uncertainty of 0.05% is assigned to account for the possible limitation of the **STOF** trigger.

Electronic and computer dead times are discussed in section 5.6. We assign a scale uncertainty of 0.06% to the electronic dead time, mainly from the deviation of the measured value of τ from the expected value of 60 ns. The point-to-point uncertainty in computer dead time depends on the trigger set up, π/e ratio, etc. and is estimated to be 0.3%.

Since the pion contamination is so small after the charge symmetric background subtracted yield, we made no explicit correction for the pion contamination (see section 5.8.2). However, we assign a 0.2% point-to-point uncertainty to account for the relative difference in the number of negative and positive pions remaining in the sample after charge symmetric background subtraction.

The charge symmetric background is discussed in section 5.8.3. At very low x values, the structure functions should scale, and any deviation is possibly due to the charge symmetric background (since this is the dominant uncertainty for heavy nuclei at small x and large scattering angles). A comparison of 40 and 50 degree data suggests that scaling is satisfied if the CSB varies by no more than 5%. A polynomial fit was made to the charge symmetric background as a function of x , and 5% of the magnitude of the charge symmetric background is applied as the point-to-point uncertainty in the charge symmetric background subtraction.

The normalization uncertainty in the cross section, due to the theoretical uncertainty in the radiative correction calculation was estimated to be 2% [99] (Note that, this is larger than the value quoted in the reference, because we do not use

the BARDIN prescription for the internal corrections). The uncertainty due to the model dependence in the radiative correction was studied by varying the DIS and QE models independently. The change in cross section was most pronounced in the low x region ($x < 0.4$). The relative uncertainty in the cross section from the model dependence is estimated to be 1%. For the helium target ratios, the point-to-point uncertainty is estimated to be 0.5% and we assign a scale uncertainty of 0.1% due to the difference in radiation length of the helium and deuterium targets. For heavy nuclei ($A > 5$), the point-to-point uncertainty in the cross section ratios for $x < 0.4$ is estimated to be 1%, mainly due to the uncertainty from the radiated quasi-elastic tail. For $x > 0.4$, we assign a point-to-point uncertainty of 0.5% for the $A > 5$ target ratios. Also a scale uncertainty of 1% is assigned to the cross section ratios of nuclei with large radiation length (6% for Au and Cu) and an estimated uncertainty of 0.5% for the rest of $A > 5$ targets.

The effect of the model on the bin centering corrections was studied by varying the shape of the model. This is done by supplying artificial x and Q^2 dependence as input to the individual DIS and QE pieces. The variation was found to be most pronounced for the $x > 0.8$ region, and we estimate a point-to-point uncertainty of 0.2% for the cross sections, and 0.1% for the cross section ratios.

Uncertainties in the Coulomb corrections (see section 5.12.3) come from the uncertainty in the average potential, $V_{(0)}$, used in the EMA calculation. We estimate this to be known at the 10% level. The Coulomb correction factors were calculated using the shifted potential and the shape of the x -dependence of the cross section ratios (shifted to nominal) was fitted by a polynomial. This fit is used to compute the systematic uncertainty over the full x range. At 40 degrees for the Au target, this uncertainty ranged from 0.5% at low x to 1.5% at high x .

Uncertainty in the isoscalar correction (see section 5.13.1) is mainly due to the uncertainty in the F_2^n/F_2^p parameterizations. We estimate a point-to-point systematic uncertainty of 1% in the magnitude of the correction at $x = 0.3$ and then linearly increase this uncertainty for a maximum of 2% at $x = 0.9$.

5.15 Differential Cross Section Results

The experimental cross sections are the final product of the data reduction. Figures 5.33 and 5.34 shows the differential cross section for all the targets plotted against energy transfer, ν . Also shown are the cross section model (solid curve denoted as XEM model in the plots) used for the radiative corrections.

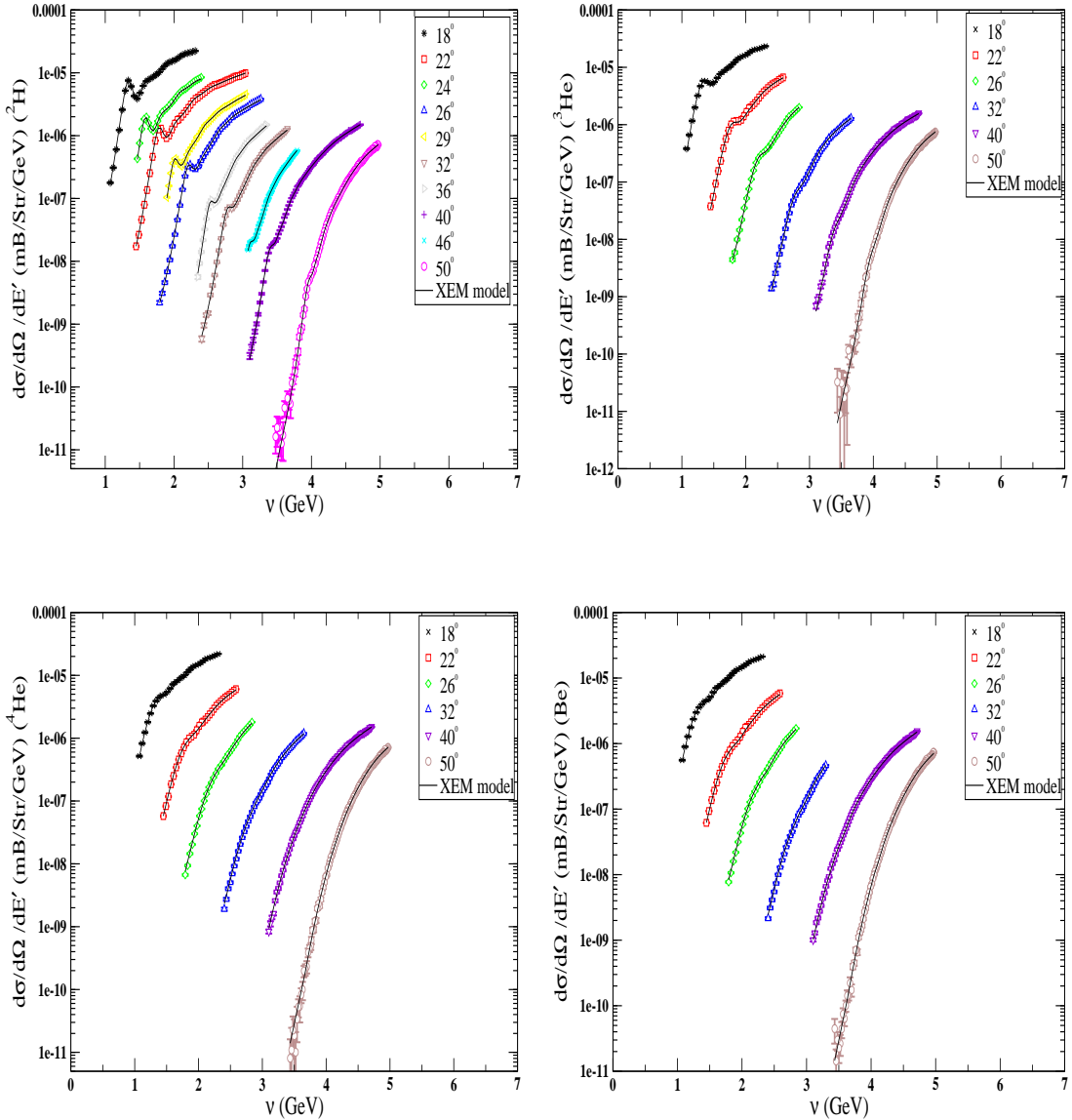


Figure 5.33 Differential Born cross sections on ^2H , ^3He , ^4He , and Be along with the XEM model.

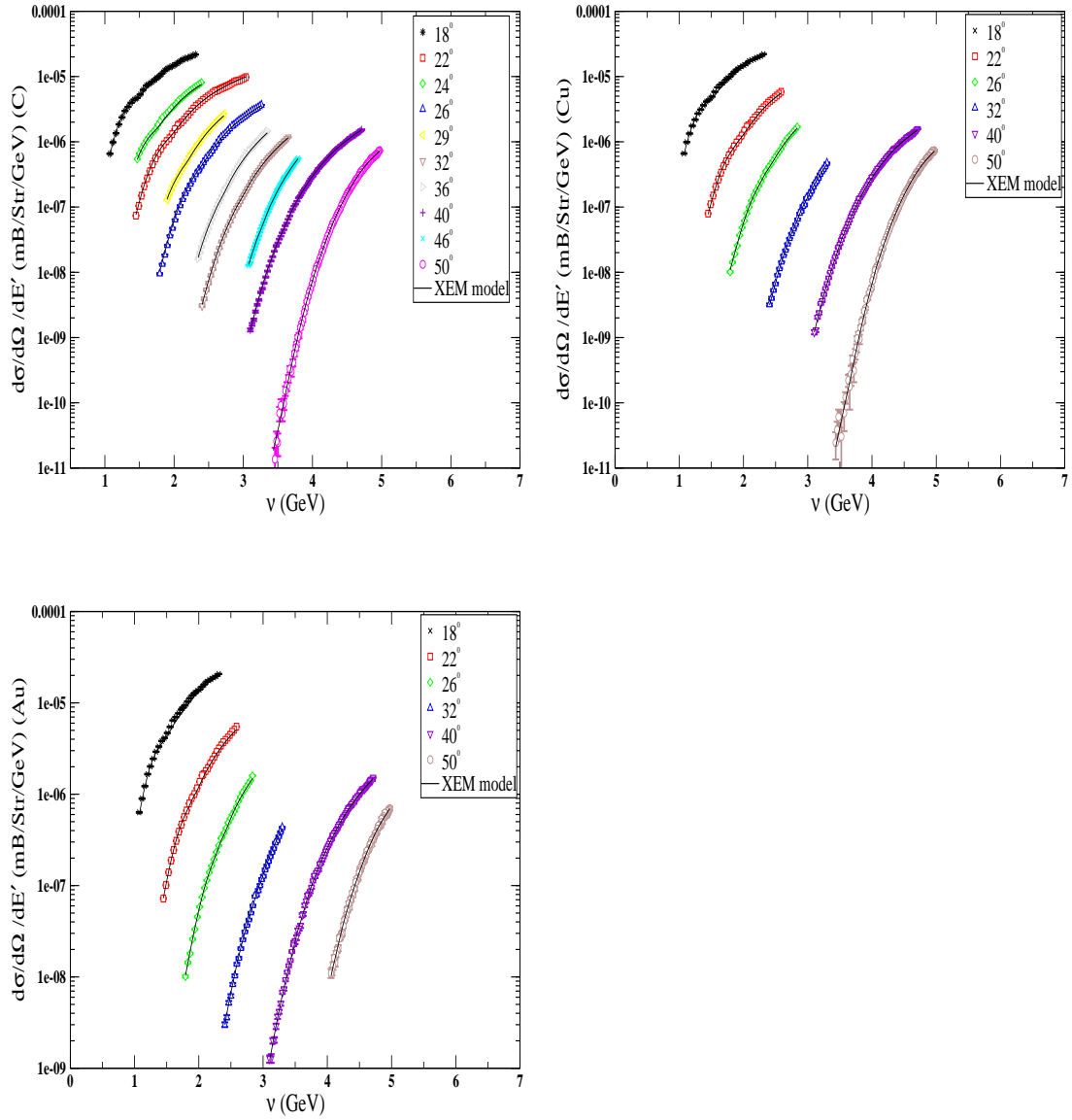


Figure 5.34 Differential Born cross sections on C, Cu, and Au along with the XEM model.

CHAPTER 6

RESULTS

In this chapter, the results of data analysis of the E03-103 experiment are presented. The chapter starts with a discussion of the the extraction of the F_2 structure function from the cross section data. Then the F_2 structure function is presented. Following the discussion of the structure functions, the result of the cross section ratios is presented.

6.1 Structure Functions

The DIS structure functions give information about the momentum distribution of quarks in the nucleus. As discussed in section 2.5.1, scaling of the structure functions for nucleons is expected to hold only in the standard DIS region ($Q^2 > 1 \text{ GeV}^2$ and $W^2 > 4 \text{ GeV}^2$), where the non-perturbative, resonance structure is no longer apparent. In the DIS region, we see scaling not only in the Björken variable x , but also in the Nachtmann variable ξ . For very large Q^2 , $\xi \rightarrow x$, and in the DIS limit ξ is related to the quark momentum distribution, as is the case for x . At finite Q^2 and at large x , additional scaling violations can originate from resonance contributions. In the case of nuclei, quasi-elastic scattering from a nucleon in the nucleus will cause additional scaling violations. However, scaling violations at finite Q^2 are smaller when we examine the data in terms of ξ rather than x , because using this variable partially accounts for target mass effects.

The F_2 structure function is given by

$$F_2^A = \frac{\nu}{1 + \beta} \frac{\sigma_{measured}}{\sigma_{Mott}}, \quad (6.1)$$

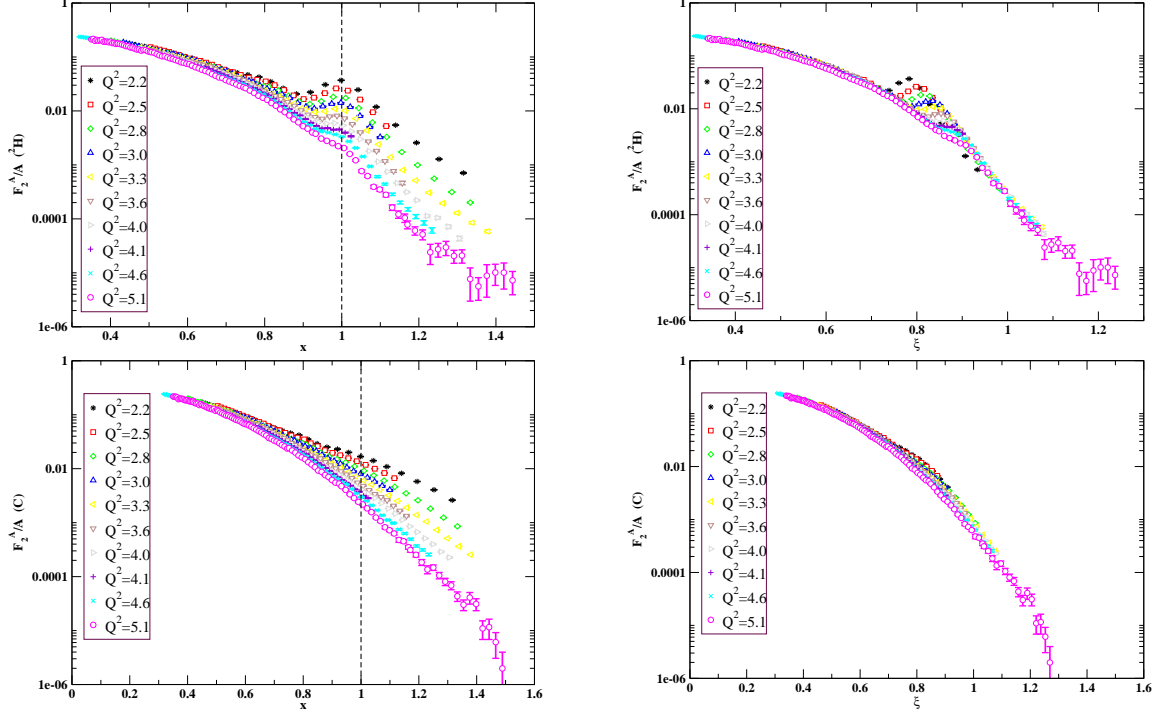


Figure 6.1 The left panels shows F_2^A/A for deuterium and carbon as a function of x , while the right panels show the same data plotted against ξ . The Q^2 values (in GeV^2) indicated in the legend are evaluated at $x = 1$.

where $\sigma_{measured}$ is the measured cross section, $\sigma_{Mott} = 4\alpha E'^2 \cos^2(\theta/2)/Q^4$, and β is given by

$$\beta = 2 \tan^2 \frac{\theta}{2} \left(\frac{1 + \frac{\nu^2}{Q^2}}{R - 1} \right). \quad (6.2)$$

If the ratio of longitudinal to transverse cross section for two different nuclei is same (*i.e.* $R_{A_1} = R_{A_2}$) then:

$$\frac{\sigma_{A_1}}{\sigma_{A_2}} = \frac{F_2^{A_1}}{F_2^{A_2}}. \quad (6.3)$$

Thus, the nuclear dependence of the structure function is directly given by this ratio of cross sections. All existing measurements are consistent with little nuclear dependence in R (see Figure 2.4). The present analysis is carried out under the assumption that R is the same for all A . Since ΔR is known to be zero at the 10% level, a change of R by 10% will change the structure function ratio by $\sim 2.5\%$. However, it should

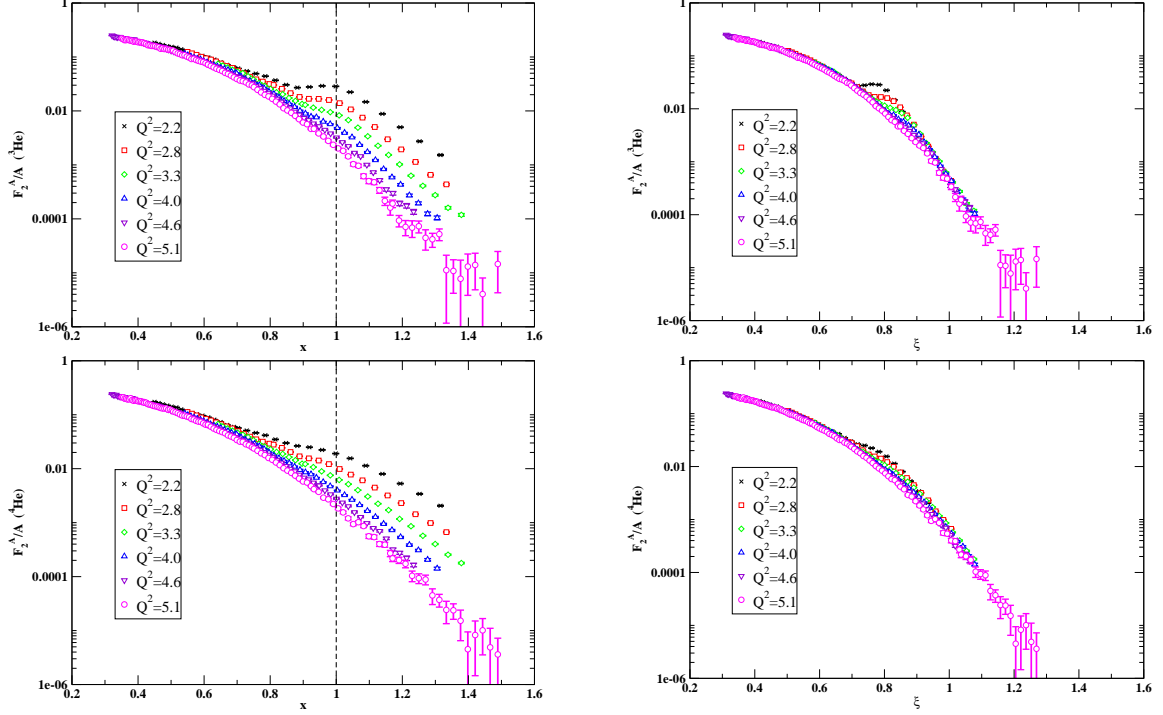


Figure 6.2 The left panels shows F_2^A/A for ^3He and ^4He as a function of x , while the right panels show the same data plotted against ξ . The Q^2 values (in GeV^2) indicated in the legend are evaluated at $x = 1$.

be noted that, since the cross section is extracted for each target, there is no uncertainty in R from the cross section ratio, other than the uncertainty in the choice of model and radiative corrections. This is found to be negligible. The results presented here are computed using R_{1990} from reference [112]. We directly measure the cross section ratios. However, if one wants to find the cross section ratios in terms of the structure function ratios (using Eqn. 6.3), one should assign an additional uncertainty to account for the possible nuclear dependence of R .

Figures 6.1 to 6.4 show the F_2^A/A structure function for all the targets measured in E03-103. The solid line at $x = 1$ indicates the position of the quasi-elastic peak. The measured structure functions are similar for all heavy nuclear targets that were measured. The data, as shown, demonstrate that the structure function does not scale in the Björken x except for lowest x values. At low x values, DIS dominates and the resonance and the QE contributions are negligible. However, the QE

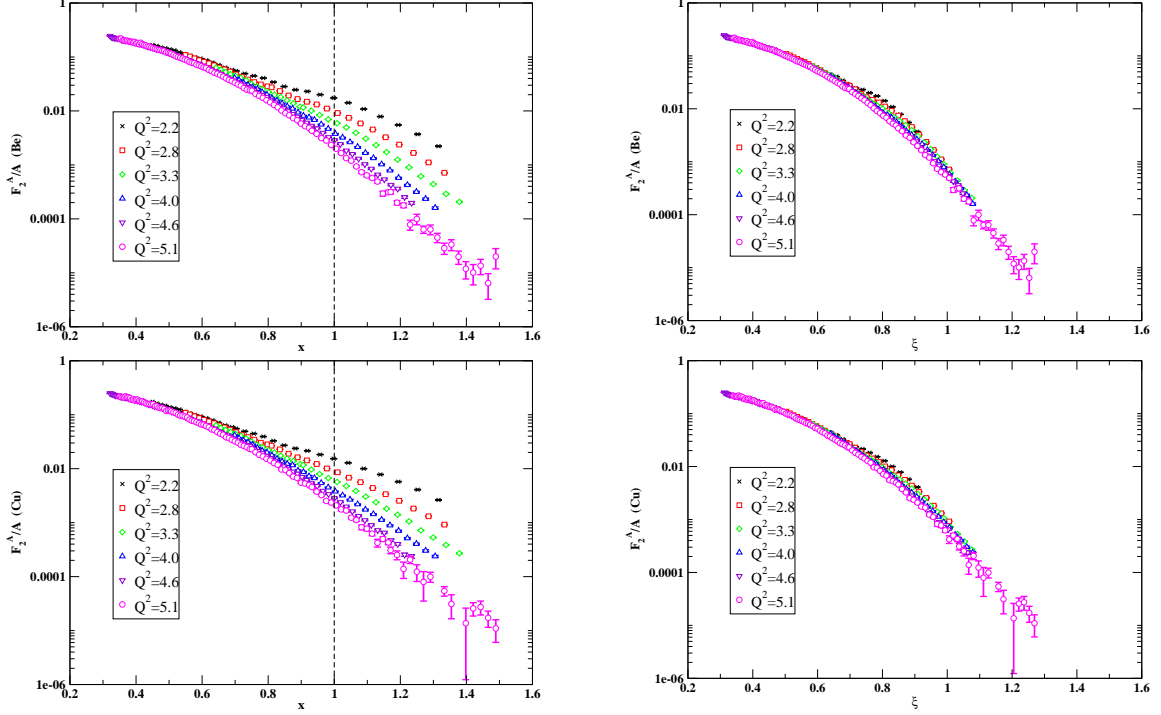


Figure 6.3 The left panels shows F_2^A/A for Be and Cu as a function of x , while the right panels show the same data plotted against ξ . The Q^2 values (in GeV^2) indicated in the legend are evaluated at $x = 1$.

contribution dominates for $x > 1$ region and produces a strong Q^2 dependence in the structure functions. For nuclear targets, Björken scaling is still violated in the resonance region and near the QE peak, but the peaks themselves are widened due to Fermi motion of the nucleons in the nucleus.

However, when plotted as function of the Nachtmann variable, ξ , the structure function shows scaling for nearly all values of ξ . The Nachtmann variable absorbs a far greater amount of the Q^2 dependence in the structure functions. At low ξ , DIS dominates, and scaling behavior is expected as predicted by the parton model. The position of the QE peak depends on Q^2 , and the peak moves to lower ξ for lower Q^2 . Furthermore, the structure functions, measured at different Q^2 values, scale above QE peak (unlike the case of x scaling). As previously mentioned in section 2.5.1, at finite Q^2 , mass effects become important as Q^2 is reduced, and x becomes a less suitable parameter as the energy is reduced. This indicates that ξ is the appropriate

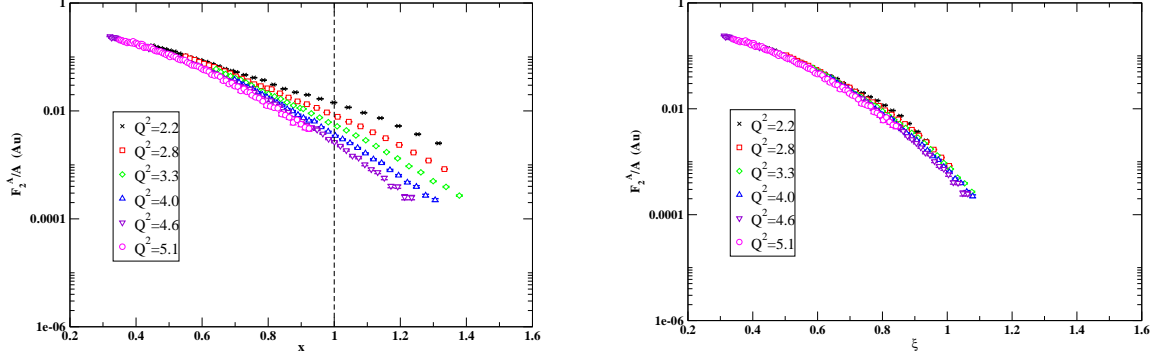


Figure 6.4 The left panel shows F_2^A/A for Au as a function of x . The right panel shows the same data plotted against ξ . The Q^2 values (in GeV^2) indicated in the legend are evaluated at $x = 1$.

variable to study parton model predictions at finite Q^2 .

6.2 Q^2 Dependence of F_2 Structure Function

We can study the quality of scaling by examining the Q^2 dependence of the structure function at fixed x and ξ . Figure 6.5 shows the Q^2 dependence of the deuterium structure function at fixed x . The curves in the figure are fits to the high Q^2 ($W^2 > 4 \text{ GeV}^2$) data from SLAC [12] using a function of the form

$$F_2^A = \exp(a + b \cdot \ln(Q^2)). \quad (6.4)$$

Here, $d \ln(F_2)/d \ln(Q^2) = \text{constant}$, as predicted by QCD. The F_2/A values at fixed $\xi(x)$ for E03-103 were obtained by fitting the structure function data near the desired value of $\xi(x)$.

Deviations of the data from the curves give a measure of the scaling violations as a function of Q^2 . From the figures we see that at high Q^2 , the structure functions for deuterium exhibit logarithmic scaling behavior as expected from QCD. From Figure 6.6 we see that, at lower W^2 (where the data are in the resonance region), scaling violations are small when the data are examined in terms of ξ . Above $Q^2 = 3 \text{ GeV}^2$, the data deviate from the logarithmic Q^2 dependence at the few percent level. When we move to higher ξ values, this extended scaling in Nachtmann variable

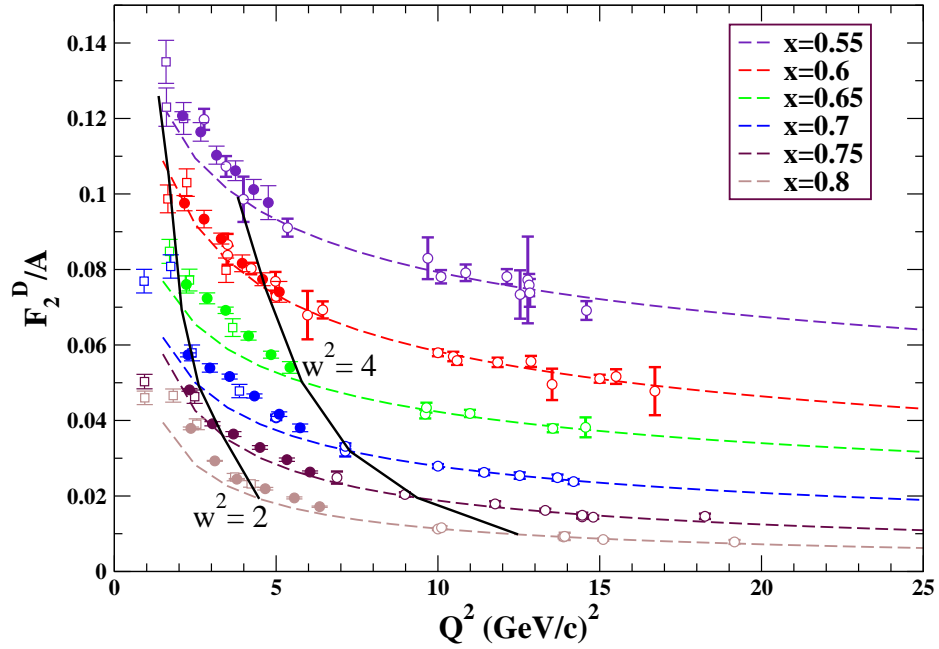


Figure 6.5 F_2^A/A vs Q^2 for deuterium at fixed values of x . The dashed lines show a logarithmic Q^2 dependence (see text for more details). Solid lines denote $W^2 = 2$ and 4 GeV^2 . The hollow circles are data from SLAC [12], the hollow squares are from JLab [33], and the filled circles are E03-103 data.

is violated (low Q^2 points) due to possible contributions from the QE peak. However, from the figure it is clear that at $\xi = 0.75$, the largest two angles are consistent with scaling. These plots quantitatively indicate that ξ is a better variable to study the parton model predictions at finite Q^2 .

6.3 Cross Section Ratios

An additional test of scaling can be performed by examining the cross section ratios themselves. One advantage of using ratios is that many of the systematic uncertainties cancel. The ratios were constructed by binning the data in $1\% \delta$ bins for each momentum setting, and computing the ratios for the final cross sections. These data were then re-binned into bins of constant ξ or x .

Figure 6.7 shows the Q^2 dependence of cross section ratios for carbon at the

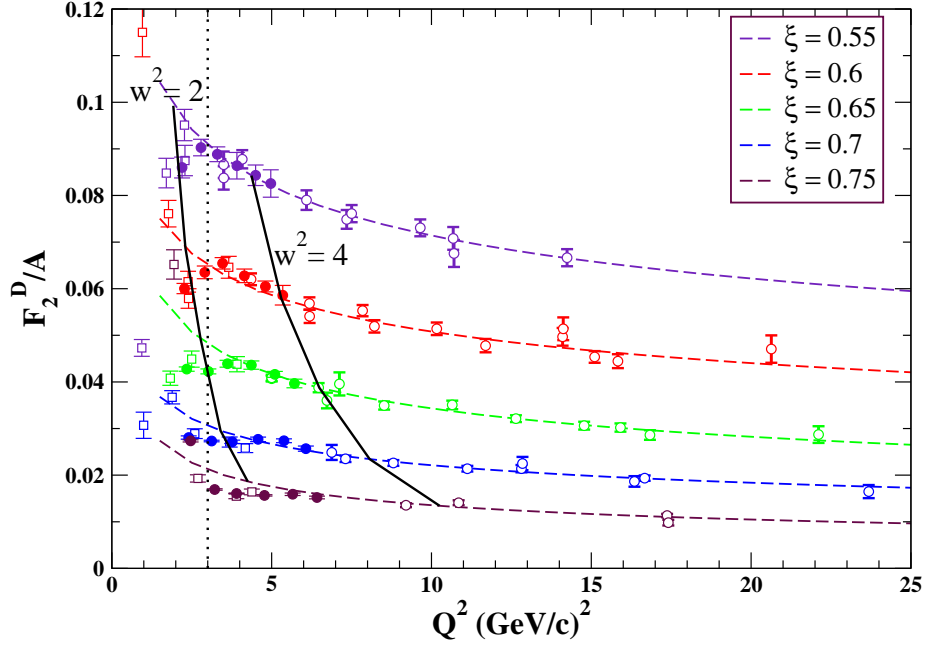


Figure 6.6 F_2^D/A vs Q^2 for deuterium at fixed values of ξ . The dashed lines show a logarithmic Q^2 dependence (see text for more details). The solid lines denote $W^2 = 2$ and 4 GeV^2 . The hollow circles are data from SLAC [12], the hollow squares are from JLab [33], and the filled circles are E03-103 data.

five largest Q^2 values taken during the experiment (at $x = 0.7$, Q^2 ranges from 4-6 GeV^2). The data at 36° and 46° were collected with a beam energy of 5.01 GeV while the rest of the Q^2 settings are at 5.76 GeV . The results are presented along with the data from SLAC [36] and JLab E89-008 [26]. The E03-103 cross section ratios are more precise, and are independent of Q^2 over the entire range of x shown. However, when plotted vs ξ , the ratios show deviation from scaling at large ξ (see Figure 6.8). The reason for this is not clear since the cross sections themselves scale better when using the Nachtmann variable, ξ . However, to ensure the greatest chance that we are in the scaling regime, we use only the two largest angles for extraction of the EMC effect. In addition, we used only $W^2 > 1.2 \text{ GeV}^2$ data, in order to exclude the region very close to the quasi-elastic peak. The cross section ratios presented here are taken as the average of the 2 highest Q^2 settings (40 and 50 degrees data at 5.76 GeV). It should be noted that the Q^2 dependence of structure functions is quite different when taken at fixed x as opposed to fixed ξ . However, this has a small effect on

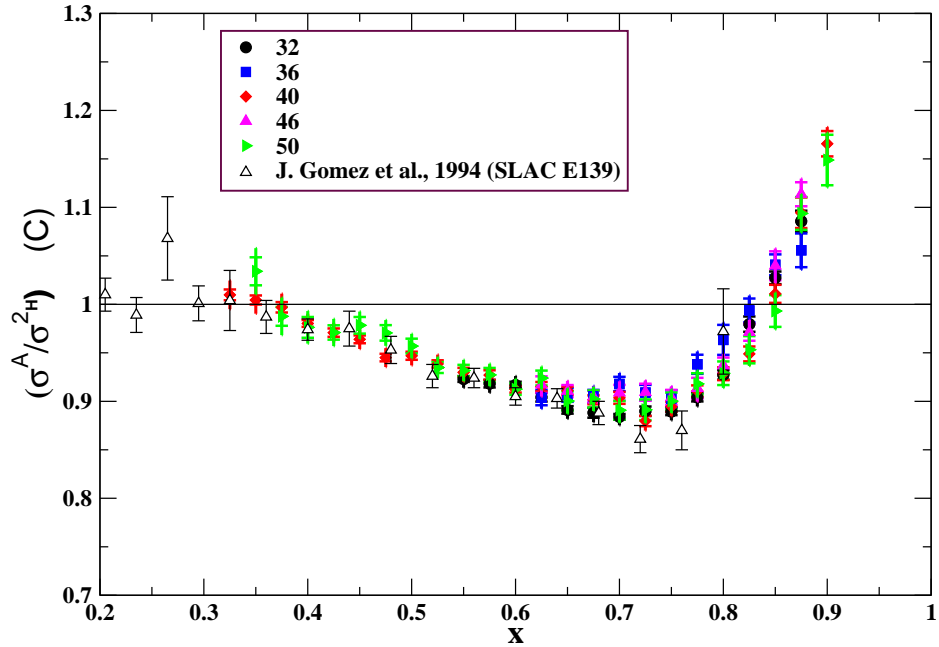


Figure 6.7 Ratio of C and ${}^2\text{H}$ cross sections for the five largest Q^2 settings (represented by different symbols and colors) as a function of x . The data at 36° and 46° were collected with a beam energy of 5.01 GeV. The inner error bars are statistical, while the outer bars are the combined statistical and estimated point-to-point systematic uncertainties added in quadrature.

the cross section ratios, and the high Q^2 EMC ratios are independent of Q^2 whether taken as a function of x or ξ . Any A -independent scaling violation cancels in the ratios as opposed to the case of structure function itself. Also, since most of the data and calculations are available in x , we will mainly present the cross section ratios as a function of x .

For high Z targets (Au and Cu), and for very low x , the contribution from charge symmetric background is quite large and substantially affects the systematic uncertainties. On the other hand, at high x , the data at large scattering angle has sizeable corrections due to Coulomb distortions and has a large contribution in the final uncertainty. Because the statistics are poor and the corrections are large for the 50° degree data, the ratios presented for Au and Cu are extracted from the 40° degree data alone. However, the 40° and 50° data are consistent within the uncertainties.

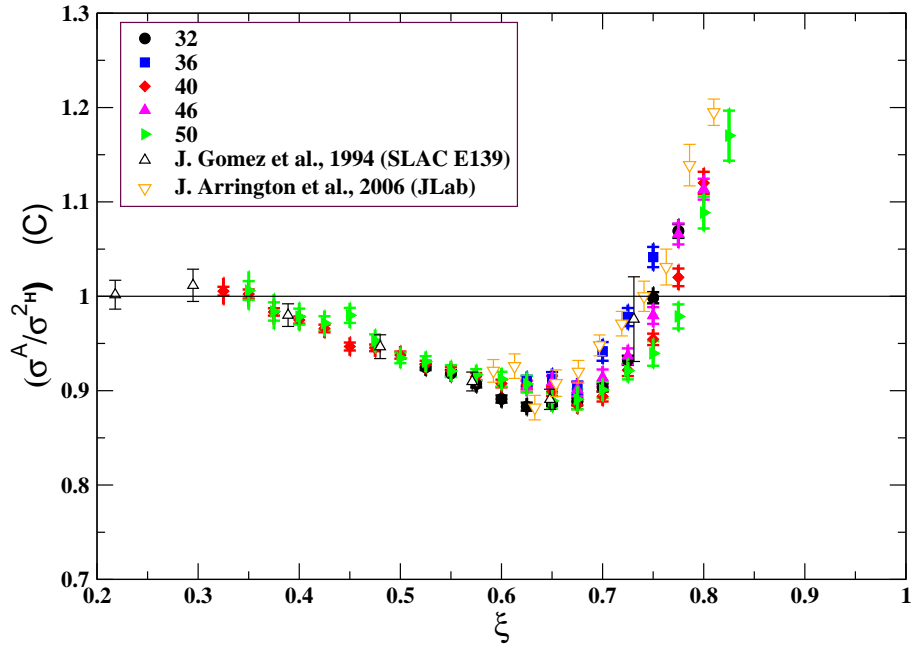


Figure 6.8 Ratio of C and ^2H cross sections for the five largest Q^2 settings (represented by different symbols and colors) as a function of ξ . The data at 36° and 46° were collected with a beam energy of 5.01 GeV. The inner error bars are statistical, while the outer bars are the combined statistical and estimated point-to-point systematic uncertainties added in quadrature. The open triangles are data from an earlier JLab experiment taken in the resonance region [26].

On the other hand, the 50° data sample has large systematic uncertainty.

We first discuss the cross section ratios for C and ^4He , since the ratios have no complications coming from isoscalar corrections, and the Coulomb distortion effects are much smaller for ($A < 12$) nuclei. Figure 6.9 shows the cross section ratios for carbon. The carbon ratio is consistent with previous data, but of much higher precision at large x values. Previous measurements were statistics limited, mainly due to the large Q^2 values required to reach the DIS region. The positions of the minima for the data sets are also consistent within error bars. The Coulomb corrections were less than a percent for C for the E03-103 data. Also, shown are a SLAC fit [36] (which is a $\ln(A)$ parameterization) and a calculation from Cloet *et al.*, [113]. There is a good agreement with the calculation at high x . This calculation is done in the quark meson coupling framework [66], where the nucleus is described using a relativistic

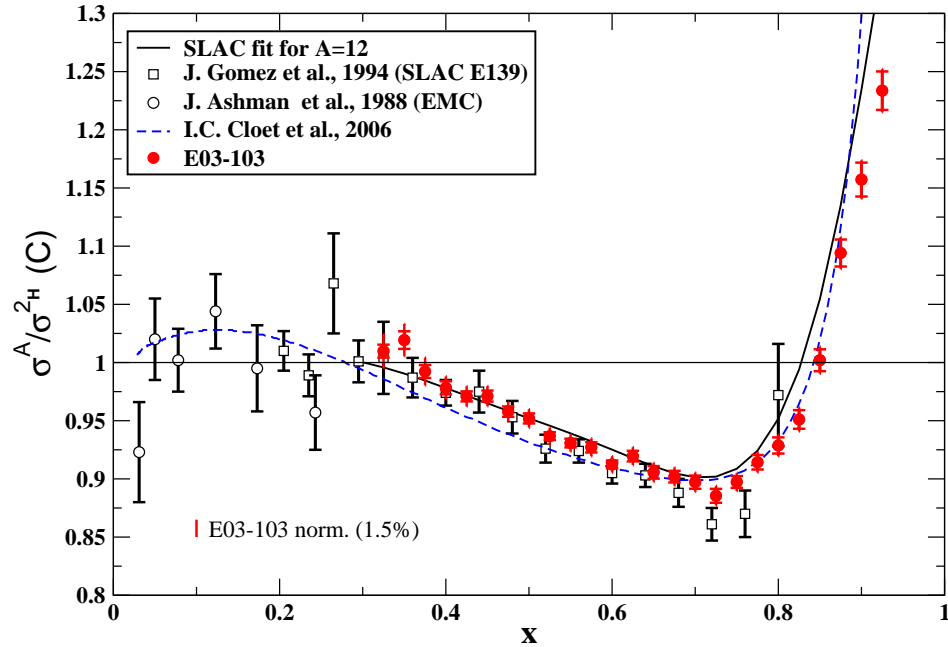


Figure 6.9 Ratio of C and ^2H cross sections. The E03-103 result (solid circles) are shown with data from SLAC [36] as open squares, and data from EMC [43] as open circles. The inner error bars are statistical, while the outer bars are the combined statistical and estimated point-to-point systematic uncertainties added in quadrature. The SLAC fits are the $\ln(A)$ parameterizations from [36]. The scale uncertainties (1σ) are also shown in the figure.

shell model, including mean scalar and vector fields that couple to the quarks in the nucleon. The nuclear structure functions are then obtained as convolutions of the structure function of the bound nucleon with the light-cone nucleon distributions.

Figure 6.10 shows the cross section ratios for ^4He along with the SLAC data [36]. Calculations of Smirnov [114], Benhar *et al.*, [115] and Cloet *et al.*, [113] are also presented. There is good agreement between the datasets, but the E03-103 result is of high precision at large x . Figure 6.11 shows the cross section ratios for carbon and ^4He . While the earlier SLAC data suggested that the EMC effect in ^4He was slightly smaller than in carbon, our results indicate that the EMC effect is nearly identical for these two nuclei. Since ^4He and carbon have about the same nuclear density (0.089 nucleons/ fm^3) [36], these results suggest that EMC effect scales with nuclear density.

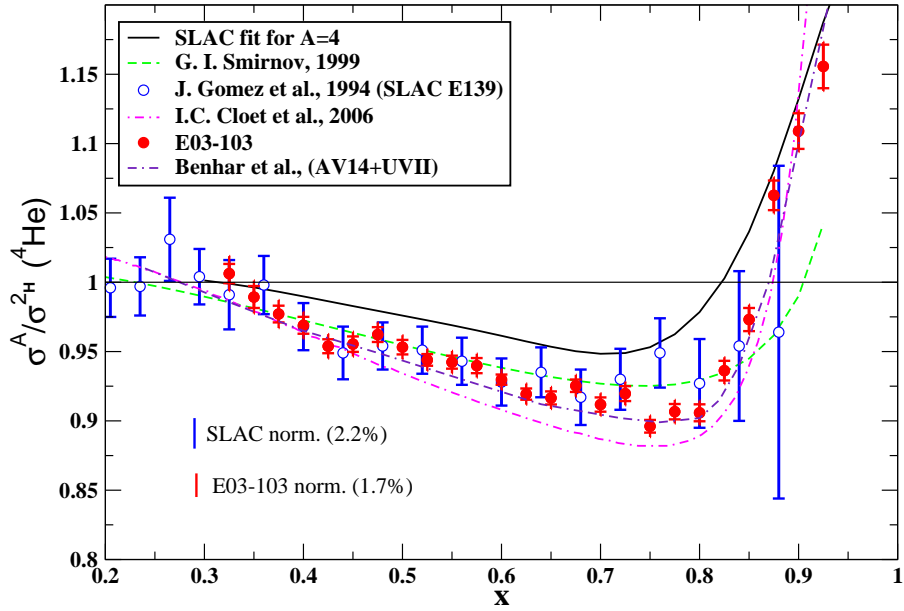


Figure 6.10 Ratio of ${}^4\text{He}$ and ${}^2\text{H}$ cross sections. The E03-103 result (solid circles) are shown with data from SLAC [36] (open circles), and a few calculations from [114, 115, 113]. The inner error bars are statistical, while the outer bars are the combined statistical and estimated point-to-point systematic uncertainties added in quadrature. The SLAC fits are the $\ln(A)$ parameterizations from [36]. The scale uncertainties (1σ) are also shown in the figure.

Figure 6.12 shows the cross section ratios for ${}^3\text{He}$. Because ${}^3\text{He}$ has two protons and a neutron, we must apply a proton excess correction to obtain the isoscalar EMC ratios (see section 5.13.1). The size of this correction is significant for ${}^3\text{He}$, ranging from 3% to 15% for our kinematics. As mentioned earlier, there is a significant uncertainty in the neutron cross section in this region, hence, the extracted EMC ratios are very sensitive to these isoscalar corrections. Figure 6.12 shows the isoscalar corrected and the uncorrected cross section ratios along with the existing HERMES results [57]. Also, shown is a fit by Smirnov [114] and a model prediction from Afnan *et al.*, [70]. It should be noted that HERMES applied a proton excess correction that used the NMC parameterization for F_2^n/F_2^p , while our results are presented with the SLAC parameterization (see section 5.13.1). All the calculations use a convolution formalism. The EMC effect in ${}^3\text{He}$, for $x > 0.7$ is larger than expected from most calculations.

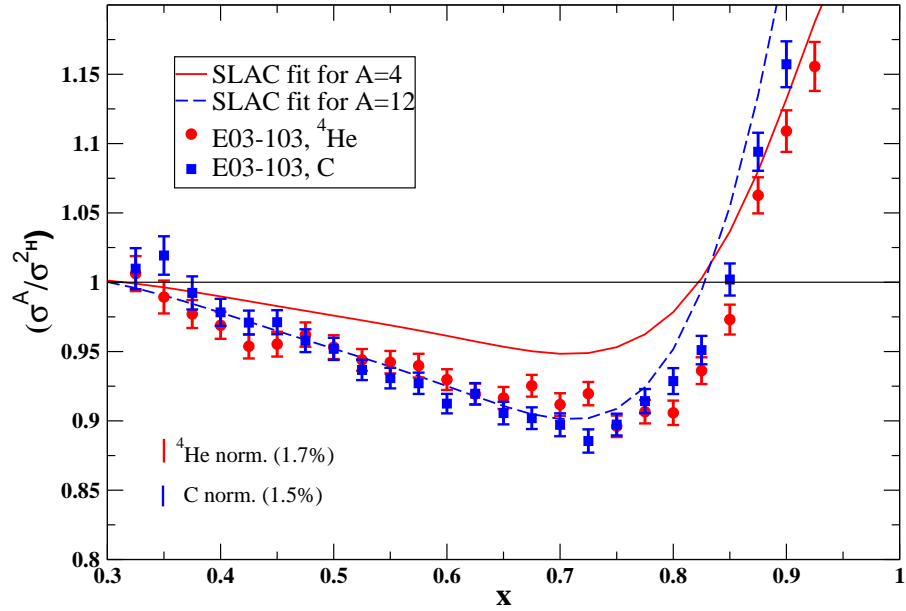


Figure 6.11 ^4He and carbon EMC ratios as a function of x . The SLAC fits are the $\ln(A)$ parameterizations from [36]. The scale uncertainties (1σ) are also shown in the figure.

6.3.1 Cross Section Ratios for Heavy Nuclei

Now we turn to the discussion of the cross section ratios for heavy nuclei. Several corrections to the data on heavy nuclei are significantly larger or more uncertain, than for light nuclei. At low x , the corrections from the charge symmetric background (see section 5.8.3) are quite large. Also, the model dependence of the radiative corrections is significant at small x (see section 5.12.2). On the other hand, at high x , Coulomb distortion effects are significant for high- Z targets.

Figure 6.13 shows the cross section ratios for Be. Our results are consistent with the SLAC [36] results and are very precise at high x values. It should be noted that the SLAC data are not corrected for Coulomb distortion (the correction factor is less than 0.5%).

Figures 6.14 and 6.15 show the cross section ratios for Cu and Au, respectively. Because of the lack of data to constrain the effects of binding (which is

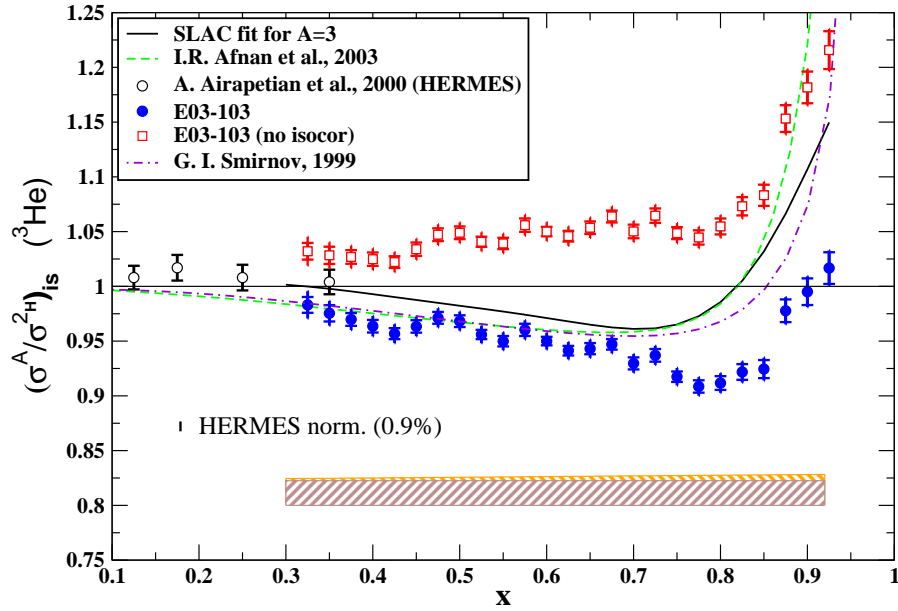


Figure 6.12 Ratio of ${}^3\text{He}$ and ${}^2\text{H}$ cross sections as a function of x . The raw cross section ratios from E03-103 are shown with hollow squares and the isoscalar-corrected ratios are shown with solid circles. Also, shown are the data from HERMES [57] (open circles) and a few calculations from [114, 70]. The inner error bars are statistical, while the outer error bars are the combined statistical and estimated point-to-point systematic uncertainties added in quadrature. The SLAC fits are the $\ln(A)$ parameterizations from [36]. The error band on the bottom includes the normalization uncertainty (brown hatched region in the bottom of the plot), while the brown and orange hatched areas represent the quadrature sum of normalization uncertainty and uncertainty from isoscalar correction.

dominant at high x), many calculations of the EMC effect are performed for nuclear matter, and extrapolated to lower density. The EMC ratio plot for Cu shows such a binding calculation from Benhar *et al.*, [71]. This calculation takes into account the binding energy of the nucleons in a realistic way, and the calculation is in fair agreement with our results for Cu, at large x . The calculation shown in the plot also include the contribution from “nuclear pions”. Our data shows that the contribution from nuclear pions, traditional binding and Fermi motion might not be enough to explain the observed effect in heavy nuclei. While our precise data provides the necessary baseline for binding calculations, it should be noted that the QE contribution to the radiative tail at very low x ($x < 0.5$) is still under investigation.

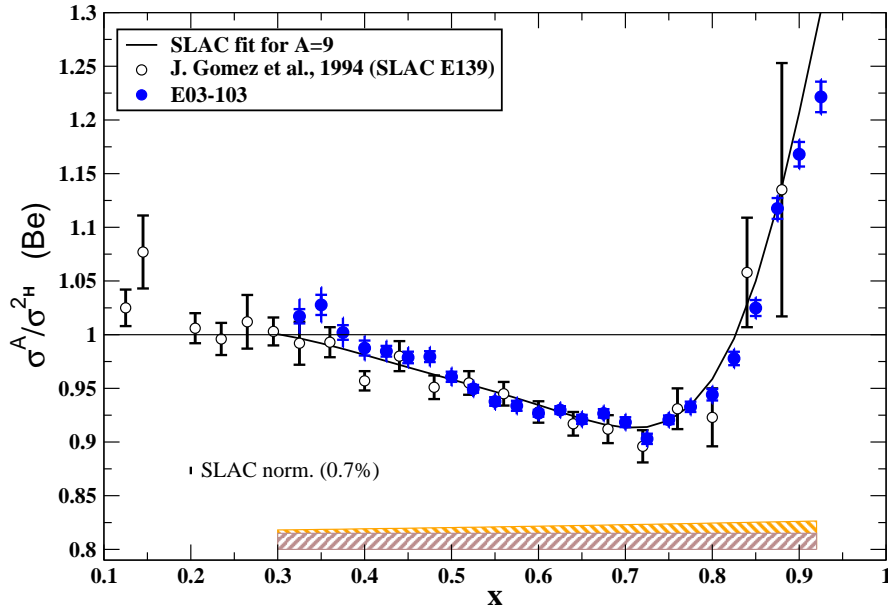


Figure 6.13 Ratio of Be and ^2H cross sections as a function of x . The E03-103 result are shown with solid circles while the data from SLAC [36] is shown in hollow circles. The SLAC fits are the $\ln(A)$ parameterizations from [36]. The error band on the bottom includes the normalization uncertainty (brown hatched region in the bottom of the plot), while the brown and orange hatched areas represent the quadrature sum of normalization uncertainty and uncertainty from isoscalar correction. It should be noted that the uncertainty from isoscalar correction is common for SLAC and E03-103, as the same correction is applied for both data sets.

The effects of binding and Fermi motion exist over the entire x region, and not at just at the largest x values. However, data at large x , and the nuclear dependence of the high x cross-over allows for tests of the models chosen to describe binding and Fermi motion. Figure 6.16 shows the cross section ratios for heavy nuclei as a function of x . The large x coverage of the SLAC measurements was insufficient to make a clear statement about the cross-over (value of x where $\sigma^A/\sigma^{^2\text{H}} = 1$) point at high x . A calculation by Gross and Liuti [58] using a manifestly covariant form of the convolution formalism predicted an A -dependent cross-over at large x (some hints of which were observed by earlier JLab data in the resonance region [26]). In this calculation, as one goes to heavier nuclei, the cross-over shifts to higher x . Another calculation including A -dependent nuclear spectral functions [72] also

gives an A -dependent cross-over at large x , but in this case the cross-over point moves to lower x values as one goes to heavier nuclei. However, there are convolution calculations (e.g., [118]) which predict no significant x dependence of the cross-over point for targets with $A > 10$. In this calculation, the high x cross-over comes about due to counter-acting contributions at large x of the average nucleon binding energy and average kinetic energy. In this framework, there is no significant A -dependence expected for $A > 10$. Qualitatively, our data agrees with an A -independent high x cross-over.

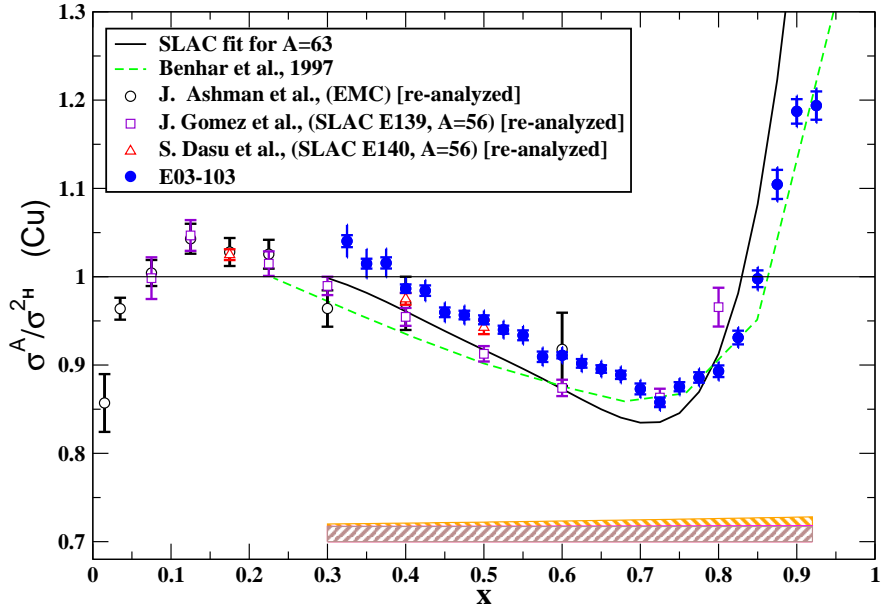


Figure 6.14 Ratio of Cu and ^2H cross sections as a function of x . The E03-103 results are shown with solid circles while the re-analyzed (including Coulomb corrections) iron data from SLAC E139 and E140 [36, 116, 117] are shown in hollow squares and hollow triangles. The re-analyzed (including Coulomb corrections) EMC data [43, 117] are represented by hollow circles. Also, shown is a calculation from [71]. The error band on the bottom shows the normalization uncertainty (from the bottom, first shaded region (in brown)), quadrature sum of normalization uncertainty and uncertainty from Coulomb correction (from the bottom of the plot (brown and magenta region)), while the full error band represents the total quadrature sum of normalization uncertainty, uncertainty from isoscalar correction and Coulomb correction. The SLAC fits are the $\ln(A)$ parameterizations from [36]. Note that data from SLAC and E03-103 used the SLAC parameterization [107] for the isoscalar corrections.

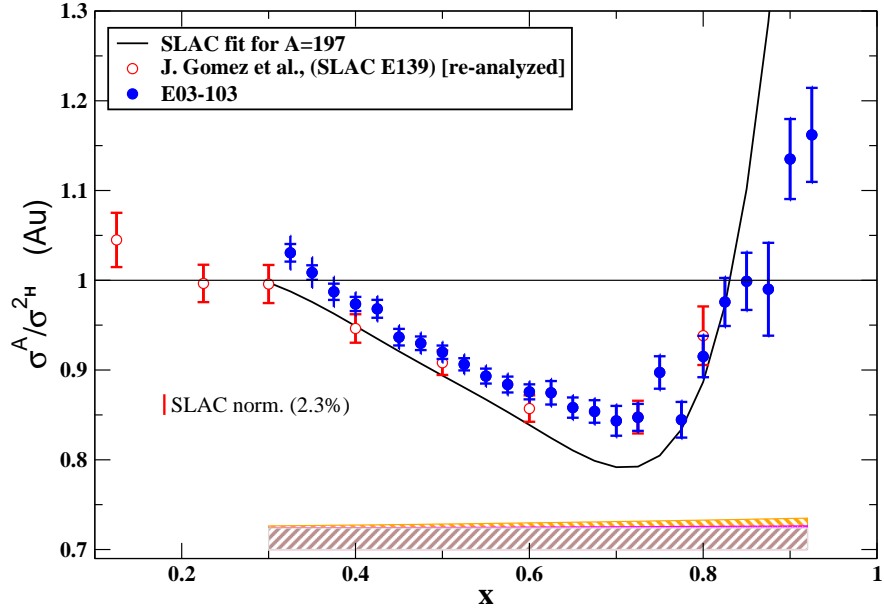


Figure 6.15 Ratio of Au and ^2H cross sections as a function of x . The E03-103 results are shown with solid circles while the re-analyzed data (including Coulomb corrections) from SLAC [36, 117] are shown in open circles. The error band on the bottom shows the normalization uncertainty alone (from the bottom, first shaded region (in brown)), quadrature sum of normalization uncertainty and uncertainty from Coulomb correction (from the bottom of the plot (brown and magenta region)), while the full error band represents the total quadrature sum of normalization uncertainty, uncertainty from isoscalar correction and Coulomb correction. The SLAC fits are the $\ln(A)$ parameterizations from [36]. It should be noted that the uncertainty from isoscalar correction is common for SLAC and E03-103, as the same correction is applied for both data sets.

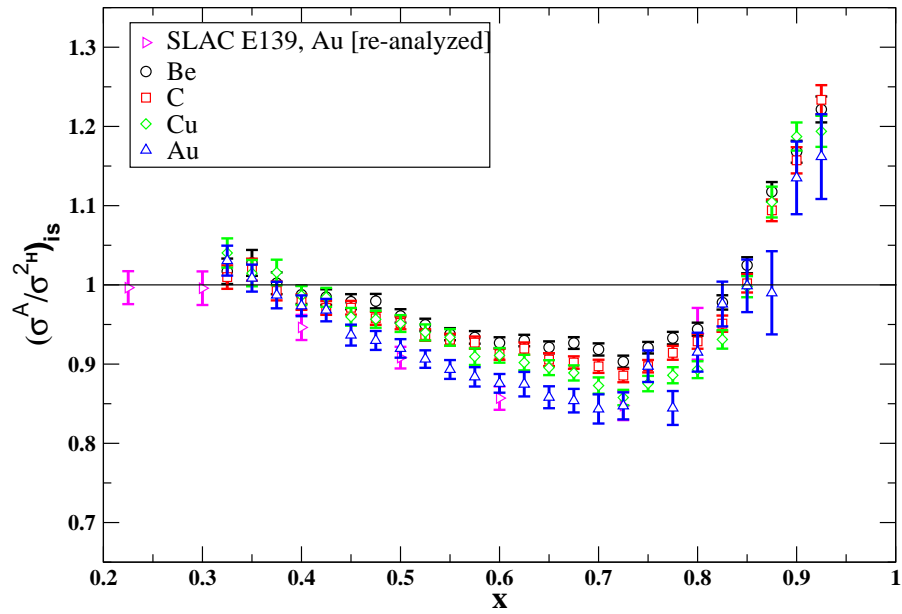


Figure 6.16 Cross section ratios for heavy nuclei as a function of x . Also, shown are the re-analyzed (including Coulomb corrections) Au data from SLAC [36, 117]. Data suggests A -independent cross-over at high and low x .

CHAPTER 7

CONCLUSIONS AND OUTLOOK

Deep inelastic scattering from unpolarized ${}^2\text{H}$, ${}^3\text{He}$, ${}^4\text{He}$ cryogenic targets and Be, C, Cu, and Au solid targets was measured by the E03-103 experiment at the Jefferson Lab. The ratios of inclusive nuclear cross sections with respect to the deuterium cross section have been determined in the x range of $0.3 < x < 1.0$ with an average Q^2 varying between 3 and 8 GeV^2 , and for beam energies of 5.77 and 5.01 GeV. These data will allow a comparison to *ab initio* calculations for few-body nuclei, where the uncertainty in the nuclear structure is minimum. Our data for heavy nuclei at large x , where binding and Fermi motion effects dominate, provide much better constraints on the effects of binding. Our high x results for heavier nuclei have better precision than the existing data, and can serve as a base-line for traditional nuclear physics calculations. Though a considerable body of data has been accumulated on nuclear parton distributions, our precise data set provides stringent constraints on the extraction of nuclear parton distribution functions.

The data show that, at high Q^2 , the structure functions for deuterium exhibit logarithmic scaling behavior, as expected from QCD. However, at lower W^2 (where the data are in the resonance region), scaling violations are small when the data are examined in terms of ξ . Above $Q^2 = 3 \text{ GeV}^2$, our results deviate from the logarithmic Q^2 dependence at the few percent level.

A variety of models for the nuclear dependence of the cross section ratios were also considered. It was found that the ratio of cross sections exhibits scaling to a better precision than the structure functions. The cross section ratios for C at different Q^2 values do not show any systematic Q^2 dependence, and the scatter at the largest x values is both consistent with the uncertainties in the individual

measurements. Our data agrees with the SLAC data over the kinematic regions where data are available, but our results have improved precision.

We considerably improved the precision of ^4He EMC ratios, especially in the high x region. There is also good agreement with SLAC data. Also, it was found that the EMC effect for ^4He is nearly identical to that of carbon, suggesting that the modification of the quark distribution scales with average nuclear density. Our ^3He data agree reasonably well with the HERMES data. These data exhibit the general shape observed for the cross section ratios for heavy nuclei. However, the ^3He results suggest that the EMC effect is larger in this $A=3$ systems than one would expect if one simply scales the EMC effect by nuclear mass or average nuclear density. Our results for C and Be are consistent with SLAC data, and are very precise at high x values. We have measured the cross section ratios for Au and Cu, and our data improve the precision of the EMC ratios in the high x region, and give a fine mapping of the EMC effect in the region above $x=0.7$. We improved the large x coverage of the EMC effect, and our results suggest that the high and low x cross-over of the cross section ratios are target independent. This result is significant, since the nuclear dependence of the high x cross-over allows for tests of models chosen to describe binding and Fermi motion.

Since the experimental effects (magnitude of deviation from unity) are at the few percent level, our results are both sensitive to experimental uncertainties and model dependence in their interpretation. For non isoscalar nuclei, the extraction of the EMC effect critically depends on the parameterization of F_2^n/F_2^p . Thus, precise data on F_2^n/F_2^p ratios would greatly reduce the uncertainty in isoscalar corrections. A recent measurement of inclusive electron scattering on an almost free neutron using CLAS, and a novel recoil detector is attempting to address this issue [119].

Another novel technique to address isoscalar corrections is to use the lightest mirror nuclei ^3He and ^3H to extract the F_2^n/F_2^p ratio [120]. In the absence of the Coulomb interaction and in an isospin-symmetric world, the properties of the proton bound in the ^3H nucleus is identical to that of a neutron bound in a ^3He nucleus. By measuring the ratio of the structure functions of these mirror nuclei, one can directly

extract the neutron to proton ratio with less sensitivity to nuclear effects. There is a proposal [121] to measure this ratio at the Jefferson lab as part of the 11 GeV upgrade program.

Compared to the unpolarized sector, the polarized counterpart of the EMC effect is poorly explored. The spin-dependent EMC effect emphasizes the quark polarization degrees of freedom within a nucleus, due to the spin-dependence of the coupling between the quarks and the strong gluon fields inside the nucleus. There are calculations which predict that the EMC effect of the spin dependent structure functions is significantly larger than that for the usual F_2 structure function [122]. Also, there is now a considerable body of high-quality DIS data, but more investigation is required to exploit other hard probes with differing sensitivities to quark-flavor and gluon degrees of freedom.

Additional information will be available once the analysis of mass number and density dependence of the cross section ratios is complete. Extrapolation of the ratio of nuclear and deuteron cross sections per nucleon to $A = \infty$ yields the nuclear matter cross section ratio [123, 124]. Understanding the EMC effect of nuclear matter is important, and our data will improve the knowledge of the EMC effect of nuclear matter. In addition, one can explicitly subtract (in a model-dependant way) the quasi-elastic contribution and look at the behavior of the cross section ratios at large x . Further, one can explicitly correct for target mass effects using the prescriptions available in literature (e.g., see [25, 125]), and investigate the “target mass corrected” cross section ratios.

Finally, we hope the data presented in this work will bridge the gap between measurement of the EMC effect in light nuclei and heavy nuclei, thus providing a comprehensive, precise basis to test state of the art models that attempt to explain the observed nuclear dependence.

APPENDIX A

Calculation of effective cryotarget thicknesses

As mentioned in section 4.3 there were several factors that had to be taken into account when computing the effective target length. The cryogen was contained in cells with cylindrical geometry (tuna can). These cans are made of Al 7075 (an alloy of aluminum), and are roughly 4 cm in diameter [96].

Dimensions of the target cells were measured at room temperature. Since the cryogenic liquid was kept at a very low temperature, this caused a thermal contraction to the Al containers. All cryotargets were operated below 25 K, and the contraction factor for aluminum was determined to be 0.996 for this temperature range [91, 82].

During the experiment it was found that the beam was offset by 1.1 mm left (facing downstream) of the ideal beam axis. Also, the target ladder was shifted 2.5 mm to the right of ideal beam axis due to target cooldown. It is known that the target ladder typically moves during the evacuation of the scattering chamber. This vacuum motion is estimated to be 1 mm [92] (in the same direction as the cooldown motion). So this amounts to a horizontal deviation of 4.6 mm between the center of the can and the real beam axis. In addition, the target cells were surveyed with respect to the ideal beam axis, and it was found these cells were also offset from their nominal positions. This introduces another offset which is target cell dependant.

The effective target length as seen by the beam is given by the length of the chord that the beam traverses in the target material:

$$t = 2\sqrt{r^2 - a^2}, \quad (\text{A.1})$$

where r is the radius of the can and a is the horizontal distance (corrected for all offsets) between center of the can and the real beam axis. Furthermore, one needs

to account for the finite width of the raster. The raster averaged target thickness is given by

$$\langle t \rangle = \frac{2 \int_{a_0-w}^{a_0+w} da \sqrt{r^2 - a^2}}{\int_{a_0-w}^{a_0+w} da}, \quad (\text{A.2})$$

with $w = 1$ mm is the half width of the raster and a_0 represents the point of intersection of beam from center of the can.

Target	Loop	Inner diameter of cell (cold) (cm)	Cell offset (mm)	t (cm)	$\langle t \rangle$ (cm)	Areal thickness (g/cm ²)
¹ H	2	3.977	-0.03	3.868	3.865	0.2794
² H	3	3.975	-0.10	3.862	3.860	0.6446
³ He	2	3.977	-0.03	3.868	3.865	0.2736
⁴ He	1	3.969	+0.31	3.875	3.873	0.5229
¹ H	1	3.969	+0.73	3.893	3.890	0.2812
² H	2	3.977	+0.63	3.897	3.894	0.6503

Table A.1 A detailed calculation of cryotarget thicknesses. Beam left (facing downstream) is positive. The inner diameter of the cell is obtained from reference [91]. Here, t represents the offset corrected cryogen in the path of the beam and $\langle t \rangle$ includes the correction due to the width of the raster. In the analysis, $\langle t \rangle$ is used to find the areal thickness. The two rows in the bottom list the cryotarget information in the summer run period, while the top rows contain information about the fall run period. Uncertainties associated with cryotarget thicknesses are given in Table 4.3.

The areal thickness of the cryotarget is the product of density and effective target length of the cryogen. Fluctuations in the target density can affect the areal thickness, and, hence, the cross sections. The density of the target is computed from the knowledge of pressure and temperature. For E03-103, we constantly monitored the temperature and pressure fluctuations which were recorded in EPICS file.

Pressure was measured with pressure transducers with a precision of ~ 1.5 PSIA, and the temperature was monitored by two Lakeshore Cernox resistors measured with a precision of ~ 0.1 K. The densities of the cryo targets are sensitive to fluctuation in temperature rather than fluctuations in pressure, so the uncertainty in the density measurement via the equation of state is dominated by the temperature dependence. The temperature and pressure of ²H and ¹H targets were maintained

at 22 K, 24 PSIA and 19 K, 21 PSIA, respectively. The temperature and pressure of ^3He and ^4He were maintained at a nominal value of 5.8 K, 117 PSIA and 6.2 K, 182 PSIA, respectively.

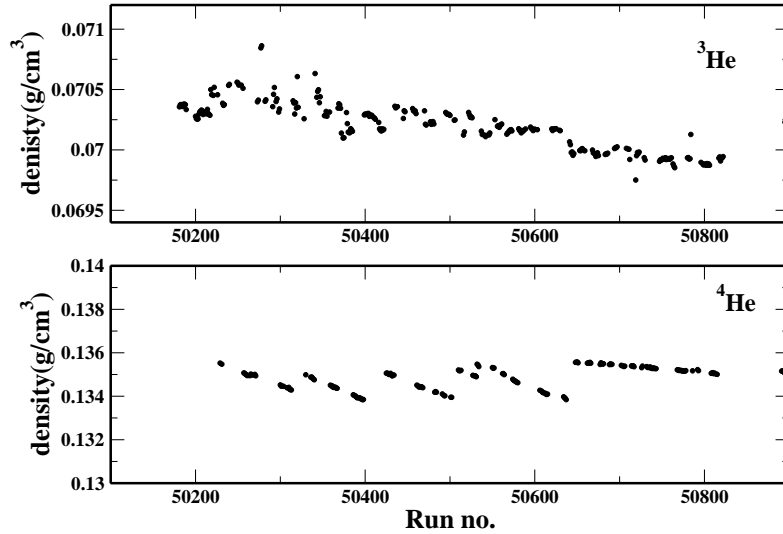


Figure A.1 The figure shows the absolute density of the helium targets computed using the tables, as described in the text. Fluctuations seen in the ^4He density are due to frequent refill and subsequent leak of target material.

During the experiment it was found that there was a leak in the helium target cells. Because of the leak, the pressure of the material in the target changed over time. Since the change was not significant enough over the course of a single run, it was decided to compute the target densities on a run by run basis. For a given run, the temperature and pressure is averaged over all the EPICS events and then this run-averaged temperature and pressure is used to compute the density of the target for that run. The pressure and temperature dependence is interpolated from data tables to get the absolute density. This is shown in Figure A.1. For ^4He , densities were calculated using the data tables provided by National Institute of Standards and Technology [126], while for ^3He , we used reference tables from [127]. These tables provide the absolute density to a precision of 1%.

In addition to the offsets mentioned above, fluctuations in the horizontal beam positions about the nominal position will also influence the effective target

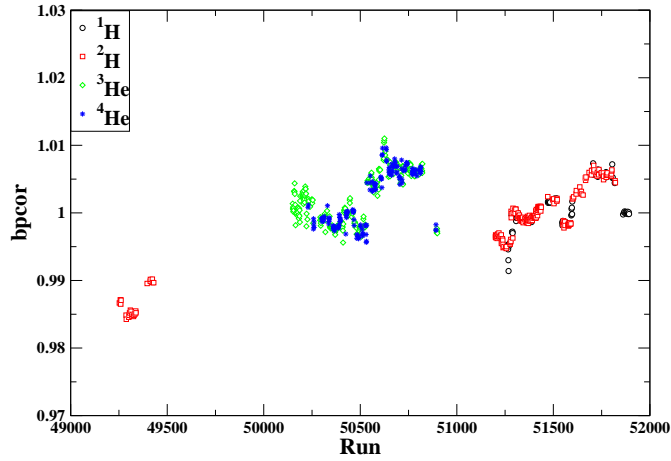


Figure A.2 The run-by-run beam position correction factor (bpcor) for the cryotargets plotted against run number.

length. This effect can be calculated with the help of BPM information recorded in the EPICS files. During E03-103, the BPM H00A was located at $z_{bpm1} = 327.15$ cm and H00B at $z_{bpm2} = 231.46$ cm from the target ($z = 0$). Thus, for a given run, the horizontal coordinate of the point of intersection of the beam and the can is given by,

$$x_{run} = \left[x_{bpm2} + \frac{\Delta x}{\Delta z} z_{bpm2} \right] + \delta x, \quad (\text{A.3})$$

where

$$\frac{\Delta x}{\Delta z} = \frac{x_{bpm2} - x_{bpm1}}{z_{bpm1} - z_{bpm2}}. \quad (\text{A.4})$$

Here, δx includes the nominal beam offset and BPM offset (-1.1 mm + 0.18 mm), and x_{bpm} is the current weighted average of BPM position information from EPICS file. Then the horizontal displacement of the beam from the nominal position for a given run is $dx = x_{run} - x_{nominal}$ with $x_{nominal} = -1.1$ mm, the beam offset from ideal beam axis. Thus, the beam position correction factor for a given run is:

$$\text{bpcor} = \frac{\sqrt{R^2 - x_{off}^2}}{\sqrt{R^2 - (x_{off} - dx)^2}}, \quad (\text{A.5})$$

where $R = \langle t \rangle / 2$ (see also Table A.1) and $x_{off} = 4.6$ mm. Here, the numerator represents the nominal thickness assuming the beam is stable, and the denominator

accounts for the thickness variation due to fluctuation in beam position. Figure A.2 shows this beam position correction factor against run number for different cryo targets used in E03-103. For ^3He , the sensor that was read out in EPICS was rescaled to better agree with the average of the three transducers. This is accounted for by scaling the ^3He areal densities by $\frac{1}{1.0051}$.

REFERENCES

- [1] J. J. Aubert *et al.*, Phys. Lett. B **123**, 123 (1983).
- [2] J. Arrington and D. Gaskell, spokespersons, Jefferson Lab experiment E03-103.
- [3] R. Hofstadter *et al.*, Rev. Mod. Phys. **28**, 214 (1956).
- [4] F. Halzen and A. D. Martin, *Quarks and leptons: an introductory course in modern particle physics* (John Wiley and Sons, 1984).
- [5] M. N. Rosenbluth, Phys. Rev. **79**, 615 (1950).
- [6] R. L. Jaffe, hep-ph/9602236.
- [7] W. Greiner and A. Schafer, *Quantum Chromodynamics* (Springer Verlag, 1994).
- [8] J. D. Bjorken, Phys. Rev. **179**, 1547 (1969).
- [9] M. Breidenbach, Phys. Rev. Lett **23**, 935 (1969).
- [10] W. M. Yao *et al.*, Journal of Physics G **23**, 187 (2006).
- [11] F. E. Close, *An introduction to Quarks and Partons* (Academic Press, 1979).
- [12] S. Dasu *et al.*, Phys. Rev. D **49**, 5641 (1994).
- [13] L. Whitlow, Ph. D. Dissertation, Stanford University, 1990.
- [14] M. E. Peskin and D. V. Schroeder, *An introduction to quantum field theory* (Addison-wesley, 1995).
- [15] C. Callan and D. Gross, Phys. Rev. Lett. **22**, 156 (1969).
- [16] G. Altarelli and G. Parisi, Nucl. Phys. B **126**, 298 (1977).

- [17] J. L. Miramontes and J. S. Guillen, *Z. Phys.* **C41**, 247 (1988).
- [18] D. F. Geesaman, K. Saito, and A. W. Thomas, *Annu. Rev. Nucl. Part. Sci.* **45**, 337 (1995).
- [19] W. Melnitchouk, R. Ent, and C. E. Keppel, *Physics Reports* **406**, 127 (2005).
- [20] R. L. Jaffe, Lectures presented at the Los Alamos School on Quark Nuclear Physics, Los Alamos (1985).
- [21] K. Wilson, *Phys. Rev.* **179**, 1499 (1969).
- [22] J. M. Cornwall and R. E. Norton, *Phys. Rev.* **177**, 2584 (1969).
- [23] R. G. Roberts, *The Structure of the Proton* (Cambridge University Press, 1990).
- [24] O. Nachtmann, *Nucl. Phys.* **B63**, 237 (1973).
- [25] H. Georgi and H. D. Politzer, *Phys. Rev. D* **14**, 1829 (1976).
- [26] J. Arrington *et al.*, *Phys. Rev. C* **73**, 035205 (2006).
- [27] M. A. Dewitt and S. Jeschonnek, *Quarks, hadrons and Nuclei; Proceedings of the 16th and 17th Annual HUGS* (World Scientific, 2004).
- [28] E. D. Bloom and F. Gilman, *Phys. Rev. Lett.* **25**, 1140 (1970).
- [29] E. D. Bloom and F. Gilman, *Phys. Rev. D.* **4**, 2901 (1971).
- [30] I. Niculescu *et al.*, *Phys. Rev. Lett* **85**, 1186 (2000).
- [31] S. Malace, Ph. D. Dissertation, Hampton University, 2006.
- [32] M. Arneodo *et al.*, *Phys. Rev. B* **364**, 107 (1995).
- [33] J. Arrington *et al.*, *Phys. Rev. C* **64**, 014602 (2001).
- [34] J. Arrington, Ph. D. Dissertation, California Institute of Technology, 1998.
- [35] A. Martin *et al.*, *Eur. Phys. J. C* **28**, 455 (2003).

- [36] J. Gomez *et al.*, Phys. Rev. D **49**, 4348 (1994).
- [37] J. J. Aubert *et al.*, Nucl. Phys. B **293**, 740 (1987).
- [38] A. C. Benvenuti *et al.*, Phys. Lett. B **189**, 483 (1987).
- [39] N. Armesto, J. Phys. G: Nucl. Part. Phys. **32**, 367 (2006).
- [40] P. R. Norton, Rep. Prog. Phys. **66**, 1253 (2003).
- [41] R. P. Bickerstaff and A. W. Thomas, J. Phys. G: Nucl. Part. Phys. **15**, 1523 (1989).
- [42] G. Piller and W. Weise, Phys. Rep. **330**, 1 (2000).
- [43] J. Ashman *et al.*, Phys. Lett. B **202**, 603 (1988).
- [44] J. Ashman *et al.*, Z. Phys. C **57**, 211 (1993).
- [45] G. Bari *et al.*, Phys. Lett. B **163**, 282 (1985).
- [46] P. Amaudruz *et al.*, Z. Phys. C **51**, 387 (1991).
- [47] P. Amaudruz *et al.*, Z. Phys. C **53**, 73 (1992).
- [48] P. Amaudruz *et al.*, Nucl. Phys. B **441**, 3 (1995).
- [49] M. Arneodo *et al.*, Nucl. Phys. B **481**, 3 (1996).
- [50] M. Arneodo *et al.*, Nucl. Phys. B **481**, 23 (1996).
- [51] M. Arneodo *et al.*, Nucl. Phys. B **487**, 3 (1997).
- [52] A. Bodek *et al.*, Phys. Rev. Lett **51**, 534 (1983).
- [53] S. Stein *et al.*, Phys. Rev. D **12**, 1884 (1975).
- [54] A. Bodek *et al.*, Phys. Rev. Lett **50**, 1431 (1983).
- [55] R. G. Arnold *et al.*, Phys. Rev. Lett **52**, 727 (1984).
- [56] K. Ackerstaff *et al.*, Phys. Lett. B **475**, 386 (2000).

- [57] A. Airapetian *et al.*, Phys. Lett. B **567**, 339 (2003).
- [58] F. Gross and S. Luiti, Phys. Rev. C **45**, 1374 (1992).
- [59] S. V. Akulinichev *et al.*, JETP Lett. **42**, 127 (1985).
- [60] D. M. Alde *et al.*, Phys. Rev. Lett. **64**, 2479 (1990).
- [61] E. Berger and F. Coester, Phys. Rev. D. **32**, 1071 (1985).
- [62] R. L. Jaffe, Phys. Rev. Lett. **50**, 228 (1983).
- [63] F. E. Close *et al.*, Phys. Lett. B. **129**, 346 (1983).
- [64] O. Nachtmann and H. J. Pirner, Z. Phys. C **21**, 277 (1984).
- [65] K. Saito and A. W. Thomas, Nuc. Phys. A **574**, 659 (1994).
- [66] I. C. Cloet, W. Bentz, and A. W. Thomas, Phys. Lett. B **642**, 210 (2006).
- [67] J. R. Smith and G. A. Miller, Phys. Rev. Lett. **91**, 212301 (2003).
- [68] J. R. Smith and G. A. Miller, Phys. Rev. Lett. **98**, 099902E (2007).
- [69] G. I. Smirnov, Eur. Phys. J. C **10**, 239 (1999).
- [70] I. R. Afnan *et al.*, Phys. Rev. C **68**, 035201 (2003).
- [71] O. Benhar, V. R. Pandharipande, and I. Sick, Phys. Lett. B. **410**, 79 (1997).
- [72] E. Marco *et al.*, Nuc. Phys. A **611**, 484 (1996).
- [73] C. W. Leeman, D. R. Douglas, and G. A. Krafft, Annu. Rev. Part. Sci. **51**, 413 (2001).
- [74] C. Yan *et al.*, Nucl. Instrum. Methods **A365**, 261 (1995).
- [75] W. Barry, Nucl. Instrum. Methods **A301**, 407 (1991).
- [76] P. Gueye, M. Tiefenback, and C. Yan, Hall C Beam Energy Measurement (2001).

- [77] C. Armstrong, Ph. D. Dissertation, College of William and Mary, 1998.
- [78] D. Meekins, Ph. D. Dissertation, College of William and Mary, 1999.
- [79] J. Dunne, Cryo and Dummy Target Information (1997).
- [80] W. Leo, *Techniques for Nuclear and Particle Physics Experiments* (Springer Verlag, 1994).
- [81] O. K. Baker *et al.*, Nucl. Instrum. Methods **A367**, 92 (1995).
- [82] T. Horn, Ph. D. Dissertation, University of Maryland, 2006.
- [83] N. Fomin, Ph. D. Dissertation, University of Virginia, 2007.
- [84] S. A. Lewis, Overview of the experimental physics and industrial control system: EPICS (2000), Lawrence Berkeley National Laboratory.
- [85] D. Geesaman and S. Wood, Hall C analysis software vade mecum (1995), Hall C internal report.
- [86] V. Tvaskis, Ph. D. Dissertation, University of Vrije, 2004.
- [87] L. Tang *et al.*, Nucl. Instrum. Methods **A366**, 259 (1995).
- [88] M. Berz, COSY Infinity Version and Reference Manual (1995), NSCL Technical report MSUCL-977.
- [89] C. Armstrong, Hall C Time of Flight Fitting Code (1999), Hall C internal report.
- [90] V. Tadevosyan and H. Mkrtchyan, How to Calibrate HMS Calorimeter with Electrons (1999), Hall C internal report.
- [91] J. Seely, Ph. D. Dissertation, Massachusetts Institute of Technology, 2006.
- [92] D. Gaskell, Private Communication.
- [93] D. Gaskell, Ph. D. Dissertation, Oregon State University, 2001.

- [94] P. E. Bosted, Phys. Rev. C **51**, 409 (1995).
- [95] J. Arrington, Private Communication.
- [96] D. Meekins, Hall C Target Configuration (2004).
- [97] L. W. Mo and Y. S. Tsai, Rev. Mod. Phys. **41**, 205 (1969).
- [98] Y. S. Tsai, Hall C Time of Flight Fitting Code (1971), SLAC-PUB-848.
- [99] S. Dasu, Ph. D. Dissertation, University of Rochester, 1988.
- [100] A. Aste, C. von Arx, and D. Trautmann, Eur. Phys. J. **A 26**, 167 (2005).
- [101] R. Rosenfelder, Annals Phys. **128**, 188 (1980).
- [102] A. Aste and J. Jourdan, nucl-th/0403075.
- [103] P. Gueye *et al.*, Phys. Rev. C **60**, 044308 (1999).
- [104] D. Day and I. Sick, Phys. Rev. C **69**, 028501 (2004).
- [105] R. D. McKeown *et al.*, Phys. Rev. Lett **56**, 1452 (1986).
- [106] P. Bosted, Private Communication.
- [107] A. Bodek *et al.*, Phys. Rev. D **20**, 1471 (1979).
- [108] M. Arneodo, Nuc. Phys. B **364**, 107 (1995).
- [109] M. Arneodo, Nuc. Phys. B **487**, 3 (1997).
- [110] W. Melnitchouk and A. W. Thomas, Phys. Lett. **B377**, 11 (1996).
- [111] H. L. Lai *et al.*, JHEP **04**, 089 (2007), hep-ph/0702268.
- [112] L. Whitlow *et al.*, Phys. Lett. B **250**, 193 (1990).
- [113] I. Cloet, Private Communication.
- [114] V. Burov, A. Molochkov, and G. Smirnov, Phys. Lett. B **466**, 1 (1999).

- [115] O. Benhar, Private Communication.
- [116] S. Dasu *et al.*, Phys. Rev. Lett **60**, 2591 (1988).
- [117] P. Solvignon, Private Communication.
- [118] S. A. Kulagin, G. Piller, and W. Weise, Phys. Rev. C. **50**, 1154 (1994).
- [119] H. Fenker, C. Keppel, S. Kuhn, and W. Melnitchouk, spokespersons, Jefferson lab experiment E03-012.
- [120] I. R. Afnan *et al.*, Phys. Lett. B. **493**, 36 (2000).
- [121] G. G. Petratos *et al.*, Jefferson lab proposal PR-12-06-118.
- [122] I. C. Cloet, W. Bentz, and A. W. Thomas, Phys. Rev. Lett. **95**, 052302 (2005).
- [123] I. Sick and D. Day, Phys. Lett. B **274**, 16 (1992).
- [124] O. Benhar, V. R. Pandharipande, and I. Sick, Phys. Lett. B. **469**, 19 (1999).
- [125] I. Schienbein *et al.*, arXiv:0709.1775v1.
- [126] National Institute of Standards and Technology, <http://webbook.nist.gov>.
- [127] R. M. Gibbons and D. I. Nathan, Wright-Patterson AFB Report No. AFML-TR-67-175 (1967), (unpublished).